

2013

Micro/nano scale surface roughness tailoring and its effect on microfluidic flow

Jing Ren
Iowa State University

Follow this and additional works at: <https://lib.dr.iastate.edu/etd>

 Part of the [Engineering Commons](#)

Recommended Citation

Ren, Jing, "Micro/nano scale surface roughness tailoring and its effect on microfluidic flow" (2013). *Graduate Theses and Dissertations*. 13562.

<https://lib.dr.iastate.edu/etd/13562>

This Dissertation is brought to you for free and open access by the Iowa State University Capstones, Theses and Dissertations at Iowa State University Digital Repository. It has been accepted for inclusion in Graduate Theses and Dissertations by an authorized administrator of Iowa State University Digital Repository. For more information, please contact digirep@iastate.edu.

Micro/nano scale surface roughness tailoring and its effect on microfluidic flow

by

Jing Ren

A dissertation submitted to the graduate faculty
in partial fulfillment of the requirements for the degree of
DOCTOR OF PHILOSOPHY

Major: Mechanical Engineering

Program of Study Committee:
Sriram Sundararajan, Major Professor
Baskar Ganapathysubramanian
Michael Olsen
Gary Tuttle
Sumit Chaudhary

Iowa State University
Ames, Iowa

2013

Copyright © Jing Ren, 2013. All rights reserved.

TABLE OF CONTENTS

ABSTRACT	v
CHAPTER 1. INTRODUCTION.....	1
1.1 Research background	1
1.2 Surface roughness	3
1.2.1 Surface typology and characterization	3
1.2.2 Roughness characterization techniques	8
1.3 Surface modification techniques	9
1.4 Objectives, research plan, challenges and thesis organization	11
1.5 References.....	14
CHAPTER 2. Methodology.....	17
2.1 Micro/nano scale surface roughness generation and tailoring	17
2.1.1 Chemical wet etching.....	17
2.1.2 Hybrid tailoring process on quartz substrate.....	17
2.2 Micro/nano scale surface roughness characterization	18
2.2.1 Surface roughness characterization using Atomic Force Microscopy (AFM) .	18
2.2.2 Surface roughness characterization using ZYGO 3D optical profilometer	20
2.3 Microfluidic device fabrication	21
2.4 Micro Particle Image Velocimetry	24
2.5 References.....	29
CHAPTER 3. EXPERIMENTAL ANALYSIS OF THE SURFACE ROUGHNESS EVOLUTION OF ETCHED GLASS FOR MICRO/NANO FLUIDIC DEVICES.....	31
3.1 Abstract	31
3.2 Introduction	32
3.3 Experimental procedure	34
3.4 Results and discussion	37
3.4.1 Surface roughness parameters.....	37
Center-line average	38
Autocorrelation length.....	40
3.4.2 Surface height distribution	42
3.5 Conclusions	45
3.6 Acknowledgement.....	46
3.7 Appendix	46
3.8 References.....	47
CHAPTER 4. A HYBRID SURFACE TAILORING PROCESS TO GENERATE NANOSCALE RANDOM ROUGHNESS ON MATERIALS FOR MICROFLUIDIC APPLICATIONS	51
4.1 Abstract.....	51

4.2 Introduction	52
4.3 Experimental Procedure.....	54
4.4 Result and Discussion.....	57
4.4.1 Spatial distribution randomness test.....	57
4.4.2 Roughness analysis.....	60
4.5 Conclusions	70
4.6 Acknowledgments	71
4.7 References.....	72
CHAPTER 5. INCORPORATING NANOSCALE RANDOM SURFACE ROUGHNESS BY DESIGN INTO MICROFLUIDIC DEVICE FABRICATION	76
5.1 Abstract.....	76
5.2 INTRODUCTION.....	77
5.3 Microchannel fabrication	78
5.3.1 SU-8 mold fabrication	80
5.3.2 PDMS casting and liquid inlet/outlet shaping.....	81
5.3.3 Preparation of glass substrate with nanoscale random surface roughness ...	82
5.3.4 Microfluidic channel bonding, inspection and testing.....	84
5.4. Effect of the nanoscale surface roughness on Non-Newtonian blood analog fluidic flow	86
5.4.1 Blood analog fluid	86
5.4.2 Micro-PIV measurement	88
5.5 Conclusions	94
5.6 References.....	95
CHAPTER 6. NANOSCALE SURFACE ROUGHNESS AFFECTS LOW REYNOLDS NUMBER FLOW: EXPERIMENTS AND MODELING	100
6.1 Abstract.....	100
6.2 Introduction	101
6.3 Experimental procedure	102
6.4 Modeling	104
6.5 Result and discussion	107
6.6 Conclusions	112
6.7 References.....	112
CHAPTER 7. INVESTIGATION OF NANOSCALE SURFACE ROUGHNESS ON NON-NEWTONIAN MICROFLUIDIC FLOW-EXPERIMENT.....	115
7.1 Abstract.....	115
7.2 Introduction	116
7.3 Experimental methods	119
7.3.1 Roughness generation and measurement.....	119
7.3.2 Microfluidic device fabrication	122
7.3.3 Blood analog fluid	123
7.4 PIV measurement of the velocity field	126

7.5 Result and discussion	128
7.6. Conclusion	139
7.7 Reference	142
CHAPTER 8. CONCLUSIONS AND FUTURE WORK.....	146
8.1 Random roughness generation on glass substrate	146
8.2 Hybrid random roughness tailoring process on quartz substrate	147
8.3 Effect of nanoscale surface roughness on microfluidic flow	148
8.3.1 Experiments and modeling study on Newtonian fluid	148
8.3.2 Investigation of nanoscale surface roughness effect on non-Newtonian fluid.....	148
8.4 Future work	151
ACKNOWLEDGEMENTS	152
APPENDIX A. DETAILED PROCESS METHODOLOGY.....	153
I. Process flow of glass surface treatment using chemical wet etching.....	153
II. Process flow of tailoring surface roughness on quartz	154
III. Process flow for SU-8 mold fabrication	155
IV. Operating procedure of preparing PDMS	156
V. PDMS replica fabrication	157
VI. Bonding of the PDMS replica and glass substrate	158
APPENDIX B. MATLAB CODES.....	159

ABSTRACT

The rapid growth of applications of lab-on-chip and bio-MEMES (Micro-electro-mechanical systems), arranging from cell culture and drug delivery to the microscale energy harvesting, microelectronics cooling, requires an understanding of microfluidic flow. Surface roughness, even at micro and nano scale, both deterministic and random, is considered an important parameter to affect fluid flow at the microscale. Over the past several decades, a variety of studies have been carried out on the impact of surface roughness on microfluidic flow behavior, including pressure drop, friction factor, heat transfer, laminar-turbulent transition, etc. However, most of the current studies focus on the large, deterministic roughness with patterned shapes formed by micromachining or microfabrication techniques. The effect of micro/nano scale random roughness on micro fluid flow remains relatively unexplored. As the size of microfluidic chip shrinks, the effect of realistic surface roughness on the microchannel walls cannot be simply ignored. In this work, the effect of realistic random surface roughness on fluid flow at the microscale was investigated through experiment and numerical simulation.

Methods for roughness generation were explored. Chemical wet etching was used to vary the surface roughness on glass substrate. The evolution of roughness with etching parameters and the surface distribution was studied to provide a better understanding of random roughness characterization. In addition to this study, a hybrid surface tailoring process combining particle masking and reactive ion etching was developed to generate and control roughness on quartz substrate. A mathematical model was built to predict the roughness parameters, which was validated by the Atomic force microscopy (AFM) measurement. It was proved mathematically that the process is able to produce a random surface with controllable amplitude and spatial parameters.

Based on the surface tailoring techniques, microfluidic devices were fabricated with desired surface roughness inside. This was made possible through incorporating the chemical wet etching treatment to the microfluidic device fabrication. The device is made from PDMS and glass substrate using soft lithography. Different levels of roughness were generated on the glass substrates for the study.

Micro particle image velocimetry (microPIV) was utilized as an analysis tool for the microfluidic flow characterization inside rough channels. Measurement was carried out on both Newtonian fluid (deionized water) and non-Newtonian fluid (dilute xanthan gum solution) at low flow rate condition. The roughness data obtained from optical profilometry was integrated with Direct Numerical Simulation (DNS) to resolve the effect of the realistic nanoscale roughness. This work demonstrated that realistic random surface roughness, even at the nanoscale, has a measurable effect on microfluidic flow. This effect can be characterized through microPIV measurement and full-scale coupled experimental-computational analysis. Particularly, this study provides promising potential of surface roughness harness for respective lab-on-chip applications, such as chemical mixing, cell manipulation and drug delivery, etc.

CHAPTER 1. INTRODUCTION

1.1 Research background

The historical understanding of surface roughness effect on fluidic flow performance can be even traced back to nineteenth century [1]. Experimental studies were carried out to investigate mainly the pressure drop and friction factor in fluidic tubes with different relative roughness. The Colebrook equation was developed to describe the correlation between surface roughness and the resulting pressure drop [2]. The well-known Moody diagram [3] provides the Darcy friction factor as a function of Reynolds number over a small range of relative roughness (roughness height/tube root diameter) between 0-5%.

Over the past several decades, advances in microfabrication techniques facilitate the development of MEMS and lab-on-chip, bringing out exciting revival of classical fluidic theories. The size of modern microfluidic devices keep shrinking from millimeter to the level of 1-100 μm . Size effect and device downscaling leads to many interdisciplinary researches, including microscale fluid mechanics, computational fluid dynamics, micro/nano scale surface processing and measurement, etc. Beyond the academic perspective, the benefits of downscaling reach to medical and biological areas. The ability of processing large amount of fluid mixing and chemical reaction at small volumes simultaneously opens possibility of diverse application in biology and biotechnology. Modern applications of using microfluidic chip includes pathogen detection [4, 5], DNA culture and analysis [6, 7], electrophoretic separations [8], etc.

Novel products have been developed based on complex microfluidic systems to provide faster speed, better and more reliable performance at more affordable prices. For example, small

size skin-contact-actuated dispenser/pump has been produced to help patients with convenient transdermal drug injection and delivery [9]. Disposable smart lab-on-chip device has been developed for clinical point-of-care testing and diagnostics [10].

Keep in mind that due to the small scale size effect and size shrinking, especially some flow applications are at extremely small scale like several micrometers, even several nanometers, a more complete understanding of the flow behavior inside the microfluidic devices is required in order to further improve the design of current bioMEMS and lab-on-chip products.

Of particular interest, results of extensive studies indicate that surface roughness affects fluid flow behavior under low Reynolds numbers in microfluidic channels. Numerical simulations of micro flow in rough channels [11] showed that bulk flow velocity and the volumetric flow rate decrease in different rates as the roughness increases. Studies on the effect of surface roughness on friction force [12], pressure drop [13, 14], heat transfer in single-phase flow [15] and laminar-turbulent transition [16] indicate the necessity of precise control of the surface morphology inside the fluidic device for the purpose of enhancing the reliability and performance of the fluidic system [17]. Experimental results of blood flow in rough microchannels [18] emphatically showed that surface roughness affects blood viscosity due to boundary effects. Application of surface roughness for gradient generation in microfluidic system has also been widely studied [19-21].

In most of these studies, researchers relied on micro-machining or micro-fabrication techniques to produce deterministic roughness via designed shapes and patterns inside the microchannels. It is well known that almost all mechanical or chemical processing inherently produces random roughness on real surfaces [22] and consequently most engineering surfaces are random. However, the role of random roughness on microfluidic flow behavior remains

relatively unexplored. This aspect will become increasingly important as channel sizes continue to decrease in micro/nanofluidic applications.

1.2 Surface roughness

1.2.1 Surface typology and characterization

Macroscale surface roughness is formed by the surface texture including roughness (micro and nano scale), waviness (macroscale), pattern direction and surface flaws. Figure 1 shows a pictorial display of surface roughness. Within a typical measuring area, flaws and clays formed by the direction of machining can be observed on the surface. In addition, the surface also has waviness over the profile containing micro and nanoscale roughness. As the roughness sampling length falls below the cut-off wavelength value, asperities and valleys can be observed as an inherent characteristic of the surface. Micro- and nanoscale surface roughness, differed from the macroscale roughness, are mainly formed by the fluctuations within short wavelengths.

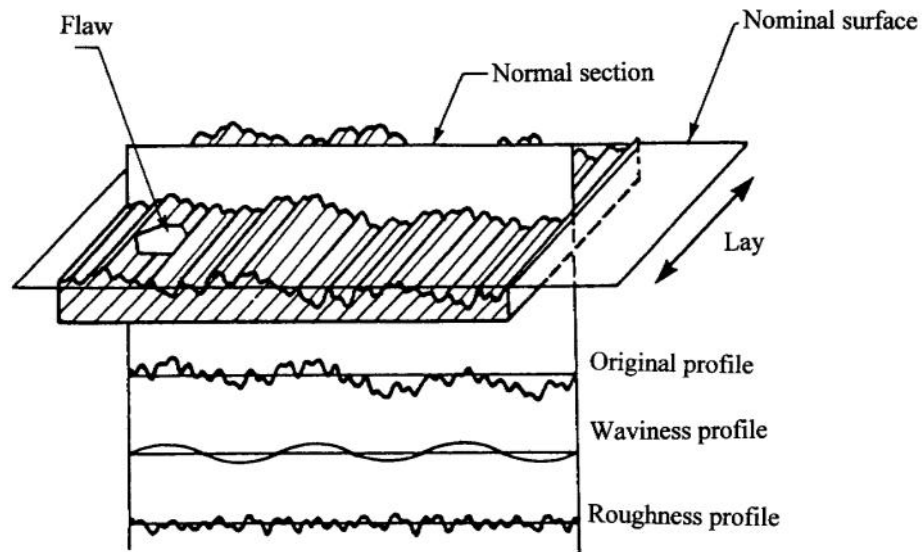


Figure 1. Surface roughness [23]

A general topology of surfaces is shown in figure 2. Solid surface can be categorized into homogeneous (contains one material) and inhomogeneous (contains more than 2 materials) types.

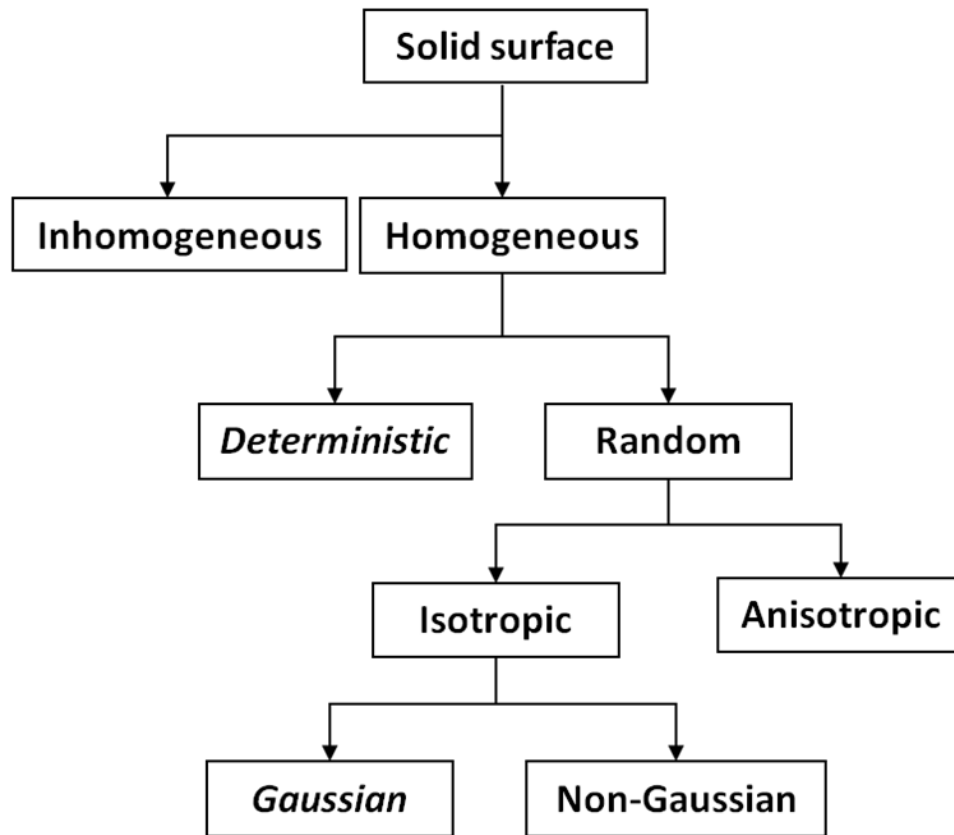


Figure 2. General topology of solid surfaces

Homogeneous surface, as the common type of engineering surfaces, can be both deterministic and random, depending on the processing method and the resulted surface texture. A comparison of typical deterministic and random surfaces is shown in figure 3. Surfaces formed by periodic shapes and patterns are considered as deterministic. Compared to this, as a natural characteristic, most realistic engineering surfaces are random, either isotropic or anisotropic. The surface height distribution is usually divided into Gaussian and non-Gaussian type, which is

also mainly decided by the processing methods. Cumulative processing such as lapping and electropolishing usually result surface roughness with Gaussian distribution, while single-point and extreme-value processing such as shaping and milling leads to anisotropic, non-Gaussian surface distribution.

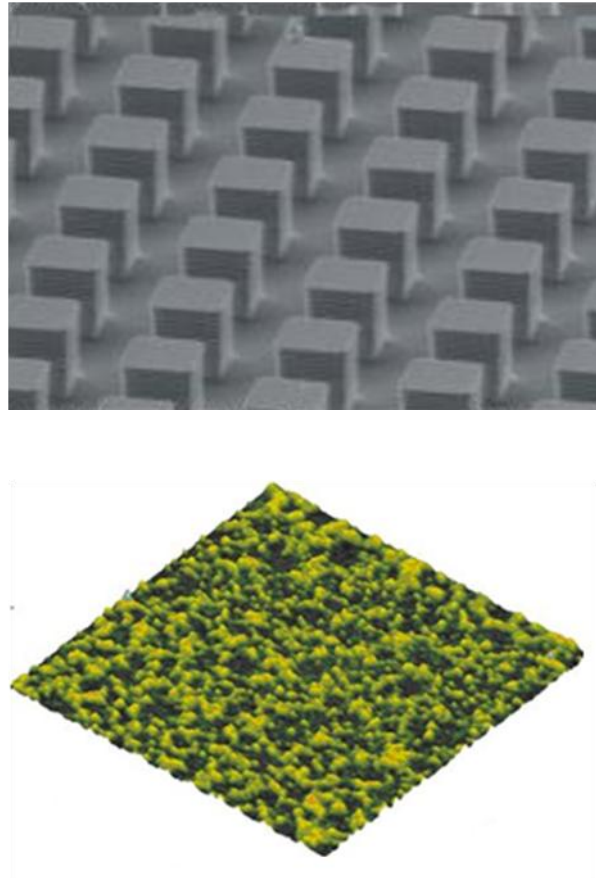


Figure 3. A comparison between deterministic and random surfaces

Roughness is generally characterized by parameters in two directions: amplitude parameters and spatial parameters amplitude parameters measure the surface profile variation in the surface height direction. Common parameters used include Ra, CLA (center-line average), variance, and root mean square (RMS) [23]. In this thesis, Ra and RMS are widely used in difference chapters. The mathematical definition of Ra can be written as

$$Ra = \frac{1}{N} \sum_{i=1}^N |z_i - m| \quad (1)$$

where N is the number of total sampling points, z is the surface height, m is mean line of the surface profile, which is defined as

$$m = \frac{1}{N} \sum_{i=1}^N z_i \quad (2)$$

and RMS is given as

$$RMS = \sqrt{\frac{1}{N} \sum_{i=1}^N z_i^2} \quad (3)$$

Spatial parameters of the surface roughness provide information of the crest spacing, or the wavelength of the surface. Widely used spatial parameters include peak density N and zero crossings density N .

In some cases, surfaces with identical amplitude parameters can have totally different topographical features, thus needs to be characterized by differences in spatial parameters. Another commonly used spatial parameter is the autocorrelation length ACL, which is a measure of the randomness of a surface. Autocorrelation length is defined as the shifting distance over which the autocorrelation function decays to a small fraction of the initial value (which is usually 10% or $1/e$). The autocorrelation function is defined as

$$C(\tau) = \frac{1}{N\sigma^2} \sum_{i=1}^N [z_i(x) - m][z_i(x + \tau) - m] \quad (4)$$

Real engineering surfaces are mostly found to follow an exponential autocorrelation function, which is give as

$$C(\tau) = \exp(-\tau / \beta) \quad (5)$$

As we mentioned previously, that the autocorrelation length is the shifting distance of $\beta^*[C(\tau) = 0.1]$ or $1/e$, as shown in figure 4.

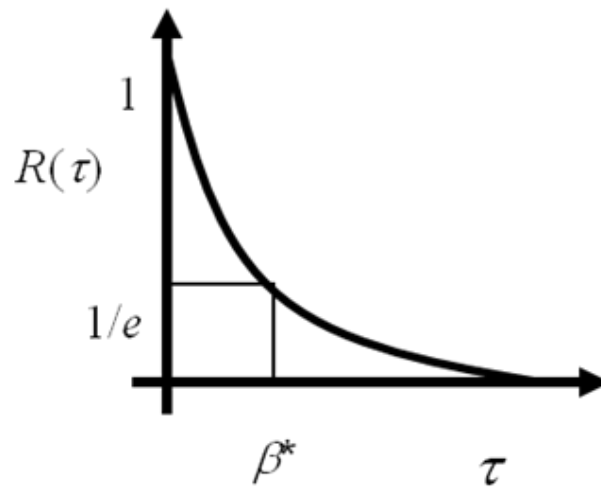


Figure 4. Autocorrelation function and autocorrelation length

In addition to the amplitude and spatial parameters, roughness is studied by using the height distribution of the digitized profile of the surface. For example, the Structure Function [24] which is given as

$$S(\tau) = \frac{1}{N} \sum_{i=1}^N [z_i(x) - z_i(x + \tau)]^2 \quad (6)$$

Besides the SF, Power spectral Density Function (PSDF) and Probability Distribution are also widely used to characterize the engineering surface information.

1.2.2 Roughness characterization techniques

For most engineering and manufacturing surfaces, the roughness is either pre-existed or formed by mechanical or chemical methods such as polishing, grinding, etching, etc. The roughness scale differs from the macro scale roughness (e.g. Surfaces with large waviness), and the nano scale roughness (e.g. the surfaces processed to molecular and atomic scale).

Characterization of macro scale roughness needs to take into consideration of the large scale waviness; while the nano scale or atomic scale roughness usually requires characterization methods such as low energy electron diffraction, scanning tunneling microscopy (STM) and atomic force microscopy (AFM) [23]. For most engineering surfaces, contact-type instruments such as contact profiler and optical methods such as optical profilometer and scanning electron microscopy (SEM) are the most widely used techniques.

Yilbas et al. [25] introduced an optical method based on the reflected beam intensity profile of the He-Ne laser beam and a fibre optic probe for detection, which limits the measurement error within 5% when the Ra value is less than 1 μm . Kuo et al. [26] developed a rapid optical system based on Eximer laser and beam profiler for nano scale poly-Si thin film surface roughness measurement. The error was reported to be less than 2.1% and the measurement time was shortened by up to 83%. Duparre et al. [27] investigated the use of AFM, mechanical profiler, white-light interferometer (WLI), confocal laser scanning microscope (LSM), angle-resolved scattering (ARS) and total scattering [6] on different samples with surface roughness in a wide range. The mechanical profiler is able to provide roughness information on surface with larger amplitude variation up to tens of micrometers. The white-light interferometer

(WLI) is also capable of measuring roughness with a peak to valley height up to 100 μm with resolution of 2 nm. The confocal laser scanning microscope (LSM) is able to measure surface height up to 200 μm . But the resolution compared to the other instruments is much lower (around 100 nm). Regarding the spatial surface roughness, in general, AFM and ARS have higher resolution, compared to other techniques including WLI and LSM.

For nanoscale amplitude and high lateral resolution roughness measurement, AFM and STM are able to provide more concise information compared to other optical instruments. Ren et al. [28] used AFM to characterize the surface roughness of chemically wet etched glass with Ra value less than 40 nm and ACL value less than 4 μm . Yu et al. [29] used STM to obtain the roughness information of a soft x-ray multi-layer film with RMS value less than 5 nm and lateral attribute (RMS average spatial wavelength λ_q) less than 20 nm.

1.3 Surface modification techniques

The purpose of surface modification is to change the physical, chemical or biological properties of materials surfaces (typically solid materials) through different methods. Physical surface properties including surface texture, roughness, waviness and wettability can significantly influence the materials behaviors when brought into contact with other surfaces. Chemical and biological surface properties also play important roles in processes of absorption, penetration, dyeing, and biomedical reaction, etc. [30].

Here we will only focus on the physical and mechanical characteristics change of solid materials surface at micro scale, including surface roughness and surface hydrophilicity. Roughness change of a solid material substrate is usually realized by material removing or adding processes. Polishing, grinding, machining are mostly commonly used material removing

processes in engineering surface modification. Compared to these top-down techniques, coating, thin film deposition, electroplating are used as surface modification methods by adding materials to the substrates.

With the rapid growth of needs to fabricate microscopic mechanical-electrical systems such as MEMS and lab-on-chip, emerging technologies in the past several decades have been developed for microscale surface modification. Micromachining and microfabrication are widely used to process silicon-based materials in the fabrication of minimized structures, such as integrated circuit and semiconductor devices. Chemical reaction is a common process in semiconductor processing, which is able to change the surface roughness of materials by removing a layer or generating a new layer on the substrate [17]. Nabe et al. reported a chemical reaction method using BSA (Bovine Serum Albumin) solutions to modify the surface of polysulfone ultrafiltration membranes [31]. Our previous work [28] experimentally studied the roughness generation on glass substrate by buffered oxide etch, which provides a fast and low-cost method to alter the roughness in a relatively wide range. Plasma treatment is another versatile surface modification technique on various materials. Lai et al. reported a surface roughness and wettability change by microwave-induced argon plasma treatment on polycarbonate (PC), polypropylene [32], polyethylene terephthalate (PET) substrates [33]. In addition, surface modification using plasma treatment has been reported on other materials, such as polyester films [34] and poly(dimethylsiloxane) (PDMS) [35], etc.

Other microscale surface modification methods includes organosilanization, UV irradiation [36], laser-micromachining [37], and oxidization [38].

1.4 Objectives, research plan, challenges and thesis organization

As a prospective application in the biomedical area and lab-on-chip study, techniques to generate and control micro/nano scale surface roughness inside the microfluidic devices needs to be developed. Characterization methods and mathematical models are also in need to analyze the surface properties at small scale. In addition, flow visualization and measurement inside the microfluidic device should be developed to study the impact the micro/nano scale surface roughness on fluidic flow. Keeping this in mind, the objectives of this research are:

1. To obtain a better understanding of the random surface roughness characteristics and characterization methods.
2. To develop a surface tailoring process that can generate and control random roughness on materials which can be further used in microfluidic chip fabrication.
3. To incorporate the surface tailoring process into microfluidic device design and fabrication.
4. To investigate the impact of the small scale random roughness on microfluidic flow behavior.

An outline of the research objectives and the chapter organization of this thesis are shown as figure 5.

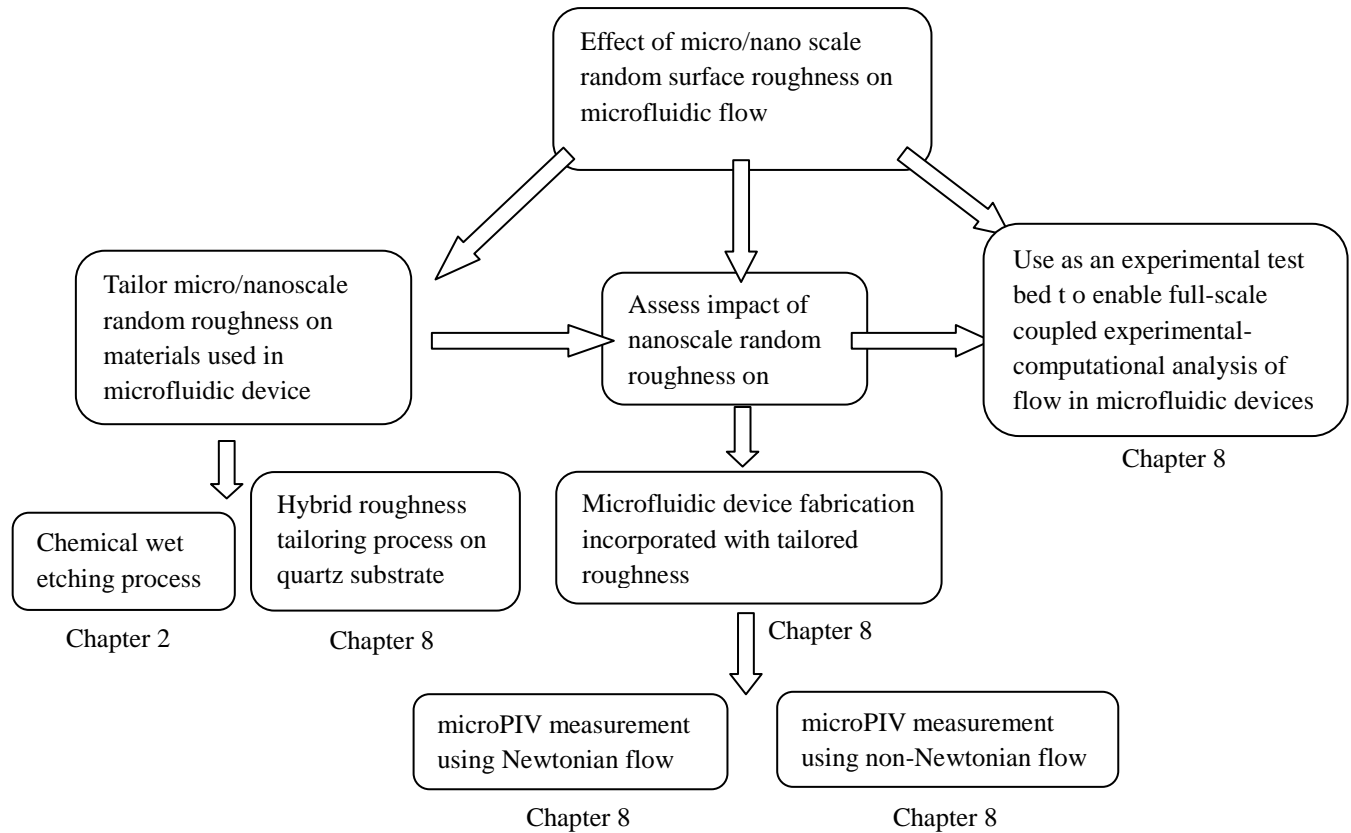


Figure 5. Outline of the research objectives

To achieve objective 1, experimental study was carried out to generate roughness on glass substrate by chemical wet etching. The surface roughness is characterized by parameters in amplitude and spatial directions. The surface height distribution of the processed glass was also studied. The *Kolmogorov-Smirnov test (KS-test)* was applied on the digitalized surface data to verify that the surface follows a T location-scale distribution. This experimental study will be introduced in chapter 3.

To achieve objective 2, a hybrid process combining colloidal masking and reactive ion etching was developed to generate and control surface roughness on quartz substrates. The randomness of the surface in spatial direction was tested and proved using a Pair correlation

function. Based on this, a mathematical model was developed to predict the surface roughness and compared to the experimental results. Chapter 4 will discuss this hybrid process of surface roughness tailoring on quartz substrate, as well as the roughness prediction model and randomness test.

To achieve objective 3, glass substrates with different surface roughness were compared by chemical wet etching. Microfluidic devices were fabricated using PDMS and the processed glass substrates. Surface roughness was measured and compared between different devices. The sealing performance of the final device was tested. The microfluidic device design and fabrication incorporated with roughness tailoring process will be introduced in Chapter 5.

To achieve objective 4, the microPIV technique was used to measure the velocity fields inside the microfluidic channels. Measurements were taken on devices with three different roughness inside the channels using both Newtonian (deionized water) and non-Newtonian (diluted xanthan gum solution) fluids. CFD simulation of the flow was also applied based on the actual surface roughness data to validate the experimental study, which lends to a deeper understanding of the characterization of the fluid flow within the microchannel. In Chapter 6, the experimental work and numerical simulation will be introduced to elucidate how the nanoscale surface roughness affects low Reynolds number Newtonian flow. The working fluid used in was deionized water. Based on this study, the effect of nanoscale surface roughness on non-Newtonian flow is further investigated. The experimental study on diluted xanthan gum solution using microPIV technique will be included in Chapter 7.

1.5 References

1. Taylor, J.B., A.L. Carrano, and S.G. Kandlikar, *Characterization of the effect of surface roughness and texture on fluid flow - past, present, and future*. International Journal of Thermal Sciences, 2006. **45**(10): p. 962-968.
2. COLEBROOK, C.F., *Turbulent Flow in Pipes, with particular reference to the Transition Region between the Smooth and Rough Pipe Laws*. Journal of the ICE, 1939 **11**(4): p. 133 –156.
3. Moody, L.F., *Friction factors for pipe flow*. ASME Trans., 1944. **66**: p. 671-683.
4. Ligler, F.S., et al., *Remote sensing using an airborne biosensor*. Environmental Science & Technology, 1998. **32**(16): p. 2461-2466.
5. Heim, S., et al., *Development of an automated microbial sensor system*. Biosensors & Bioelectronics, 1999. **14**(2): p. 187-193.
6. Schmalzing, D., et al., *DNA typing in thirty seconds with a microfabricated device*. Proceedings of the National Academy of Sciences of the United States of America, 1997. **94**(19): p. 10273-10278.
7. Vo-Dinh, T., *Development of a DNA biochip: principle and applications*. Sensors and Actuators B-Chemical, 1998. **51**(1-3): p. 52-59.
8. Walker, P.A., et al., *Isotachophoretic separations on a microchip. Normal Raman spectroscopy detection*. Analytical Chemistry, 1998. **70**(18): p. 3766-3769.
9. Mousoulis, C., et al., *A Skin-Contact-Actuated Micropump for Transdermal Drug Delivery*. Ieee Transactions on Biomedical Engineering, 2011. **58**(5): p. 1492-1498.
10. Ahn, C.H., et al., *Disposable Smart lab on a chip for point-of-care clinical diagnostics*. Proceedings of the Ieee, 2004. **92**(1): p. 154-173.
11. Yang, D.Y. and Y. Liu, *Numerical simulation of electroosmotic flow in microchannels with sinusoidal roughness*. Colloids and Surfaces a-Physicochemical and Engineering Aspects, 2008. **328**(1-3): p. 28-33.
12. Palasantzas, G. and A. Widom, *Roughness effects on the sliding frictional force of submonolayer liquid films on solid substrates*. Physical Review B, 1998. **57**(8): p. 4764-4767.
13. Kandlikar, S.G., et al., *Characterization of surface roughness effects on pressure drop in single-phase flow in minichannels*. Physics of Fluids, 2005. **17**(10).
14. Bahrami, M., M.M. Yovanovich, and J.R. Culham, *Pressure drop of fully developed, laminar flow in rough microtubes*. Journal of Fluids Engineering-Transactions of the Asme, 2006. **128**(3): p. 632-637.

15. Kandlikar, S.G., S. Joshi, and S.R. Tian, *Effect of surface roughness on heat transfer and fluid flow characteristics at low reynolds numbers in small diameter tubes*. Heat Transfer Engineering, 2003. **24**(3): p. 4-16.
16. Hao, P.F., et al., *Experimental investigation of water flow in smooth and rough silicon microchannels*. Journal of Micromechanics and Microengineering, 2006. **16**(7): p. 1397-1402.
17. Komvopoulos, K., *Surface engineering and microtribology for microelectromechanical systems*. Wear, 1996. **200**(1-2): p. 305-327.
18. Prentner, S., et al., *Effects of Channel Surface Finish on Blood Flow in Microfluidic Devices*. Dtip 2009: Symposium on Design, Test, Integration and Packaging of Mems/Moems, 2009: p. 51-54
- 429.
19. Kang, T., J. Han, and K.S. Lee, *Concentration gradient generator using a convective-diffusive balance*. Lab on a Chip, 2008. **8**(7): p. 1220-1222.
20. Keenan, T.M. and A. Folch, *Biomolecular gradients in cell culture systems*. Lab on a Chip, 2008. **8**(1): p. 34-57.
21. Lin, F., et al., *Generation of dynamic temporal and spatial concentration gradients using microfluidic devices*. Lab on a Chip, 2004. **4**(3): p. 164-167.
22. Thomas, T.R., *Rough surfaces*. 1999: Imperial College Press.
23. Bhushan, B., *Modern tribology handbook*. Vol. 1. 2001, Boca Raton: CRC.
24. Schlautmann, S., et al., *Fabrication of a microfluidic chip by UV bonding at room temperature for integration of temperature-sensitive layers*. Journal of Micromechanics and Microengineering, 2003. **13**(4): p. S81-S84.
25. Yilbas, Z. and M.S.J. Hasmi, *Surface roughness measurement using an optical system*. Journal of Materials Processing Technology, 1999. **88**(1-3): p. 10-22.
26. Kuo, C.C. and C.S. Chao, *Rapid optical measurement of surface roughness of polycrystalline thin films*. Optics and Lasers in Engineering, 2010. **48**(12): p. 1166-1169.
27. Duparre, A., et al., *Surface characterization techniques for determining the root-mean-square roughness and power spectral densities of optical components*. Applied Optics, 2002. **41**(1): p. 154-171.
28. Ren, J., B. Ganapathysubramanian, and S. Sundararajan, *Experimental analysis of the surface roughness evolution of etched glass for micro/nanofluidic devices*. Journal of Micromechanics and Microengineering, 2011. **21**(2).
29. Yu, J., et al., *Surface roughness characterization of soft x-ray multilayer films on the nanometer scale*. Journal of Vacuum Science & Technology B, 1996. **14**(1): p. 42-47.

30. Safonov, V., et al., *The surface parameters modifications at nano scale for biomedical applications*. 16 Iscomp: Progress in Solid State and Molecular Electronics, Ionics and Photonics, 2010. **253**.
31. Nabe, A., E. Staude, and G. Belfort, *Surface modification of polysulfone ultrafiltration membranes and fouling by BSA solutions*. Journal of Membrane Science, 1997. **133**(1): p. 57-72.
32. Milas, M., et al., *Flow and Viscoelastic Properties of Xanthan Gum Solutions*. Macromolecules, 1990. **23**(9): p. 2506-2511.
33. Lai, J.N., et al., *Study on hydrophilicity of polymer surfaces improved by plasma treatment*. Applied Surface Science, 2006. **252**(10): p. 3375-3379.
34. Gupta, B., et al., *Surface modification of polyester films by RF plasma*. Journal of Applied Polymer Science, 2000. **78**(5): p. 1083-1091.
35. Makamba, H., et al., *Surface modification of poly(dimethylsiloxane) microchannels*. Electrophoresis, 2003. **24**(21): p. 3607-3619.
36. Goddard, J.M. and J.H. Hotchkiss, *Polymer surface modification for the attachment of bioactive compounds*. Progress in Polymer Science, 2007. **32**(7): p. 698-725.
37. Chan, C.M., T.M. Ko, and H. Hiraoka, *Polymer surface modification by plasmas and photons*. Surface Science Reports, 1996. **24**(1-2): p. 3-54.
38. Li, L.H., et al., *Improved biological performance of Ti implants due to surface modification by micro-arc oxidation*. Biomaterials, 2004. **25**(14): p. 2867-2875.

CHAPTER 2. Methodology

2.1 Micro/nano scale surface roughness generation and tailoring

2.1.1 Chemical wet etching

In this study, surface roughness was generated on glass substrate by chemical wet etching. Evolution of the amplitude and spatial parameters of the roughness with etching time and orientation was studied. The etchant used is buffered hydrofluoric acid (6:1 volume ratio of 40% NH_4F in water to 49% HF in water). Etching time was limited between 5 minutes to 40 minutes.

Based on our experimental observation, etching times longer than 40 minutes in horizontal orientation resulted in significant surface damage on glass substrate, which led to difficulty in bonding during microchannel fabrication. Furthermore, transparency of the glass surface was significantly compromised. Therefore, in this study the maximum etching time reported is 40 minutes. This method is able to generate roughness in the range of: R_a value less than 40 nm and ACL value less than 4 μm [1]. The detailed process flow of glass surface roughness generation using chemical wet etching is described in Appendix A.

2.1.2 Hybrid tailoring process on quartz substrate

Considering the limitations of the chemical wet etching, a hybrid process was developed to generate and tailor nanoscale surface roughness tailoring on quartz in this study. The process combines surface coating, colloidal particle masking and reactive ion etching. Compared to the chemical wet etching method, this hybrid process is able to generate nanoscale surface roughness in a relatively larger range: amplitude parameter R_a up to 180 nm and spatial parameter ACL between 1-8 μm . In addition, more controllable parameters are enabled in this process, such as

the particle coverage, particle size and etch depth, through adjusting which we are able to tune the specific roughness parameters. A schematic of the process is shown in figure 1.

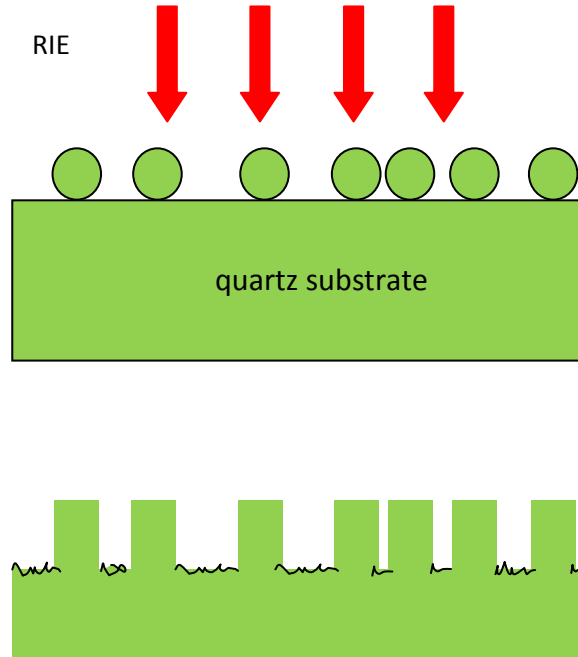


Figure 1. Schematic of Polystyrene particle masking and RIE process

Polystyrene particles are coated onto the quartz substrate and serve as masks during the following reactive ion etching. As the etch rate difference, the area beneath the particles is protected and formed pillar structures, which modifies the roughness of the substrate. Detailed process flow can be found in Appendix A .

2.2 Micro/nano scale surface roughness characterization

2.2.1 Surface roughness characterization using Atomic Force Microscopy (AFM)

In this study, an atomic force microscope (AFM, Dimension 3100, Nanoscope IV, Veeco Instruments, Santa Barbara) was used to measure surface roughness. All the processed samples

were cleaned in acetone and dried by nitrogen to remove organic waste and dust on the surface before taking AFM images. All the AFM scans were acquired in contact mode using a standard Si_3N_4 tip, at a scan resolution of 256×256 points. The scan size was chosen as $75 \mu\text{m} \times 75 \mu\text{m}$ which is comparable to the common size of microchannels used for microfluidic study. Scan areas were chosen to avoid edges of the slides to ensure valid roughness information. Figure 2 shows an example of the AFM scan images of quartz surface after the hybrid tailoring process treatment. The AFM surface height data was exported in ASCII format and MATLAB was used to analyze surface height distribution and to compute amplitude (R_a) and spatial (ACL) roughness parameters.

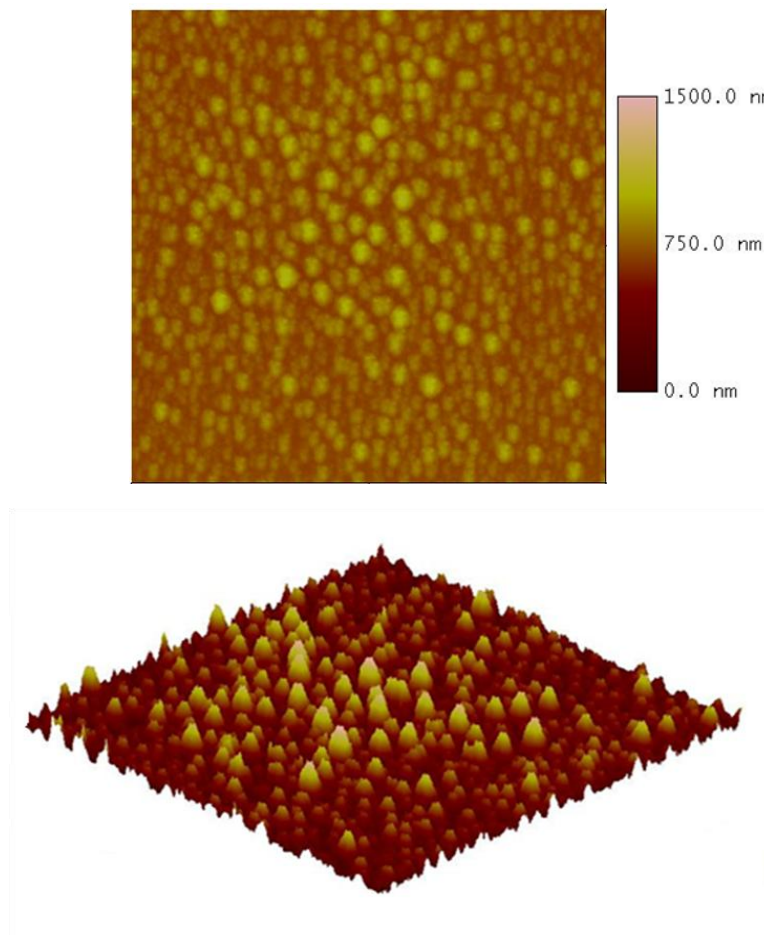


Figure 2. AFM scans of the RIE etched quartz surface

2.2.2 Surface roughness characterization using ZYGO 3D optical profilometer

The microchannel's surface topography was obtained using a 3D Optical Surface Profiler (NewView™ 7100, Zygo Corporation, Middlefield, CT). The optical profilometer provides different scales of scan area based on the objective lens magnification. In this study, a scan area of $480\ \mu\text{m} \times 360\ \mu\text{m}$, with a lateral resolution of $0.73\ \mu\text{m}$ and height resolution of $0.1\ \text{nm}$ was used. Compared to the resolution down to a fraction of nanometer of AFM system, the profilometer has relatively lower resolution. In the other hand, by using white light interference, the scan speed of the profilometer is faster than AFM.

Figure 3 shows an example of the profilometer scan of the glass surface processed by chemical wet etching. The surface height data was exported as ASCII format, and MATLAB was used to analyze surface roughness including amplitude (Ra) and spatial (ACL) roughness parameters.

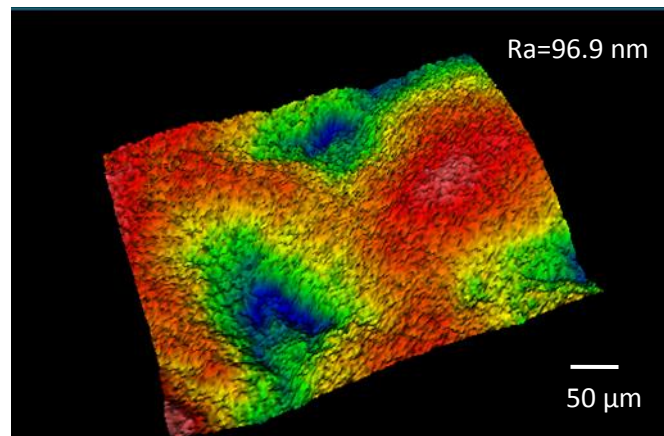


Figure 3. Surface scan of a 40 minutes etched (in buffered HF) glass slide

2.3 Microfluidic device fabrication

The rapid development of MEMS technique leads to increasing applications in bioMEMS and microfluidics. Conventional methods used in microfluidic device fabrication are limited to glass and silicon etching, which is expensive and time-consuming. Alternative fabrication methods of using polymer materials by provide reliable, faster and less-expensive solution. The methods are mainly based on soft lithography, rapid prototyping, imprinting, hot embossing, replica molding, and injection molding, etc. These techniques, compared to the conventional methods, are more accessible to researcher since they do not require a clean room environment [2]. The advantage of using soft lithography method in microfluidic system fabrication goes beyond the cost and easy operation, but more importantly, it can be incorporated to various polymer materials which are bio-compatible to enable biomedical and biological studies. In addition to this, the polymer structure can be easily integrated with other structures through bonding or sealing [3].

A rapid microfabrication technique using glass substrate and Polydimethylsiloxane (PDMS) was applied in this study for microfluidic device fabrication. The process flow is shown in figure 4.

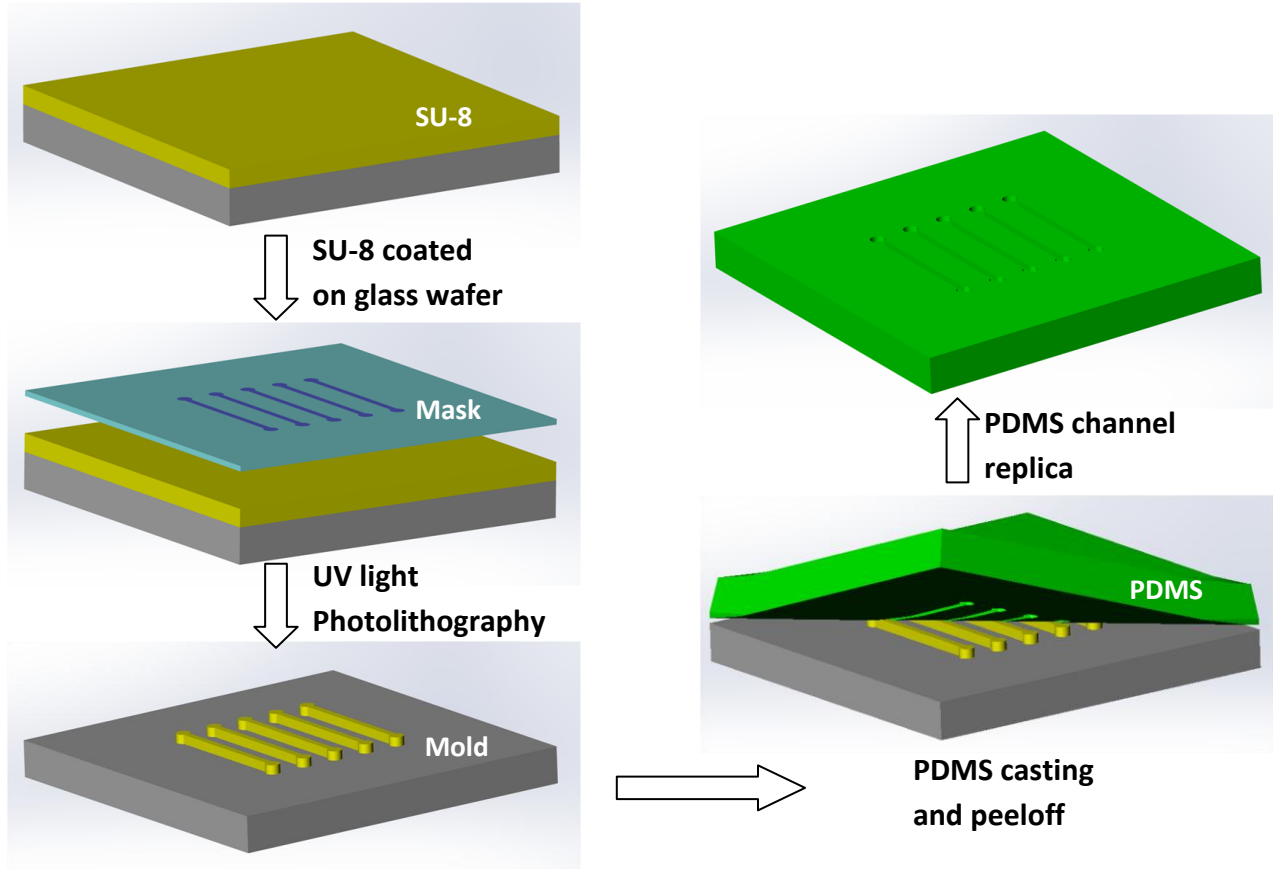


Figure 4. Processed flow of the SU-8 mold fabrication

A SU-8 mold with microfluidic channel features was created on a glass wafer by soft lithography. The microchannel patterns were further transferred to PDMS by casting it onto the SU-8 mold. The PDMS replica was peeled off after heat cure. Microflow inlets and outlets were created by setting screws on the corresponding positions while casting PDMS. An SEM image of the PDMS microfluidic channel replica is shown in Figure 5.

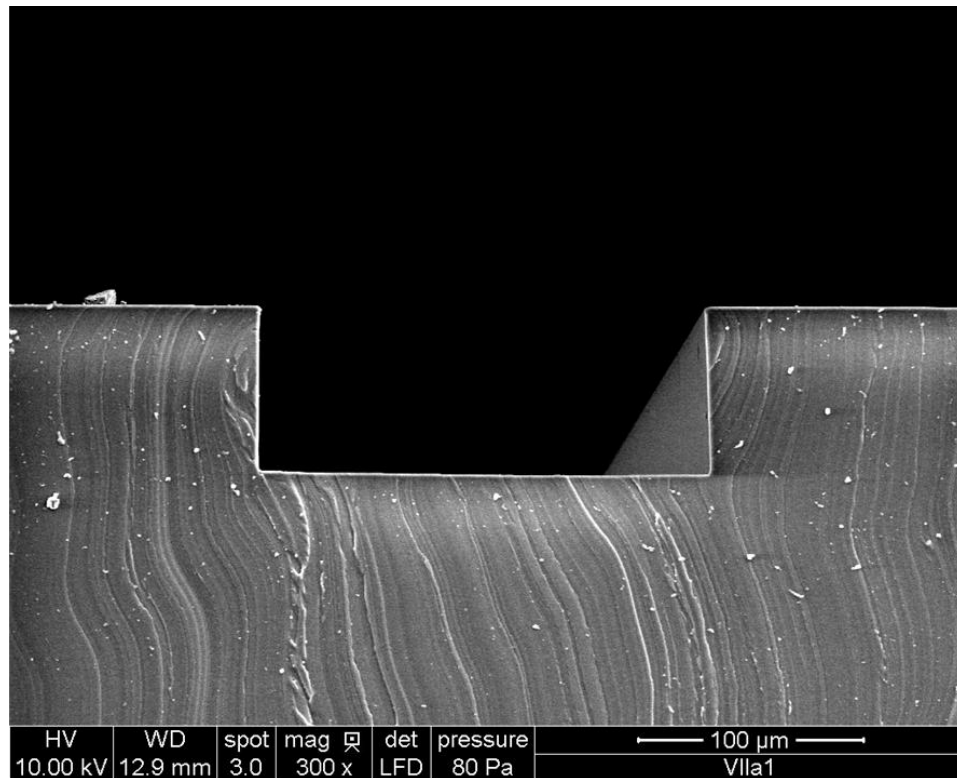


Figure 5. SEM image of the PDMS microchannel replica

The PDMS substrate was further brought into contact with glass substrate after oxygen plasma treatment to enclose the microfluidic channel. Figure 6 shows the final device with tubing attached onto the liquid inlet and outlet. The detailed process flow of SU-8 mold fabrication, PDMS preparation, channel replica molding, and glass-PDMS bonding is provided in Appendix A.

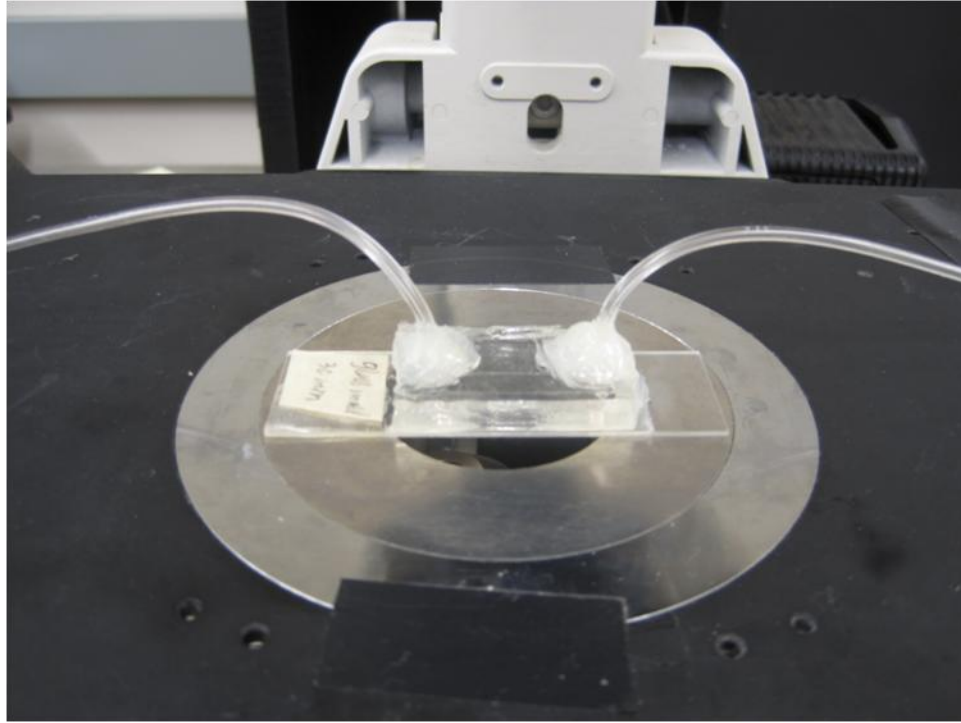


Figure 6. Microfluidic device with tubing attached for the microPIV tests

2.4 Micro Particle Image Velocimetry

In this study, the microfluidic flow visualization and velocity field measurement was realized by a micro Particle Image Velocimetry (microPIV) system.

Particle image velocimetry (PIV) is a well established technique for velocity field measurement of macroscale flow [4, 5]. The theory and experiment system is widely described and used in fluidic flow studies. In double-pulsed PIV, the working fluid is seeded with tracing particles to capture to the motion of the flow. Illumination is provided by a pulsed light source, or by using a continuous light but gating the light signal using a shutter (CCD intensifier plate or other mechanical and electrical shutters). The positions of the tracing particles are recorded at

certain time intervals. The correlation of the particle image pairs are then used to estimate the displacement of the flow statistically.

As the significant progress has been made in the MEMS and lab-on-chip applications, the need for diagnostic techniques to measure the flow performance inside the microscale devices is surged in recent decades. Specifically, a requirement of a resolution on the order of microns needs to be achieved [6]. This is particularly important for microfluidic systems, since the device performance is highly affected by the increased surface-to-volume ratio and dissipation rate [4]. In order to address the flow physics related to the down scaling, micro particle image velocimetry (microPIV) was modified from PIV to access the small scale of microfluidic systems.

The initial ground work of microPIV was developed by Santiago et al. in 1988 [4]. In their experiment, a Hele-Shaw flow inside a 30 micron size diacylinder was seeded with 300 nm polystyrene particles to trace the fluid motion. The tracing particles were tagged with fluorescent dye and continuously illuminated by an Hg-arc lamp. And the light signals were collected by the CCD (Charge Coupled Device) intensifier plate with an exposure time of 2 ms and delay time of 68.5 ms between two exposures. Based on this setup, a bulk velocity with a spatial resolution of $6.9 \mu\text{m} \times 6.9 \mu\text{m} \times 1.5 \mu\text{m}$ was measured.

In 1999, meinhart et al. reported an alternate approach of using two pulsed Nd:YAG lasers to replace the continuous Hg-arc light source in Santiago's microPIV system. This technique was tested on a flow field of $30 \mu\text{m} \times 300 \mu\text{m}$ microchannel. A resulting velocity fields measurement with high resolution of $13.6 \mu\text{m} \times 0.9 \mu\text{m} \times 1.8 \mu\text{m}$ was reported.

MicroPIV is a whole-field and non-destructive technique for flow velocity measurement at micro scale. The working theory of microPIV is similar to PIV. A schematic of a microPIV system is shown in Figure 7.

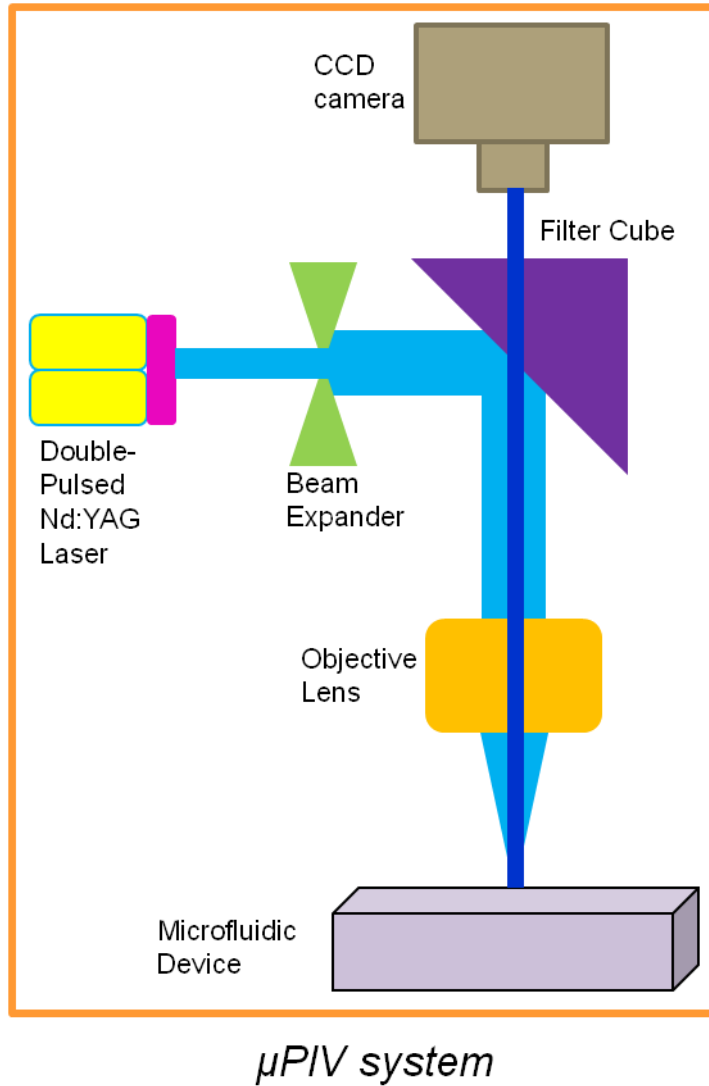


Figure 7. Micro-PIV apparatus and methodology

Fluorescent particles are added into the testing fluid as flow tracing particles. The flow is illuminated by double-pulsed laser light sources. The particles excite at a specific wavelength

and emit at another wavelength. The emitted light signal from the particles along with the reflected light goes through the objective lens, a dichroic mirror and an emission filter, which blocks the reflected laser light and let the emitted light through. The objective lens focuses on one plane of interest at a time, and a 2D image of the moving particles is created afterwards [7, 8]. Keep in mind that the movement of the particles represents the instantaneous flow motion, the system is set to record sufficient images by overlapping the interrogation spots by a certain proportion (usually 50% to satisfy the Nyquist sampling criterion). Using special averaging analysis, we are able to obtain the velocity fields of the flow at the certain plane of interest.

The flow velocity is calculated from the movement of tracing particles, which is shown in figure 8: in a time interval of Δt , a particle moves a distance of Δs , and the velocity is simply given by the ratio of $\Delta s / \Delta t$.

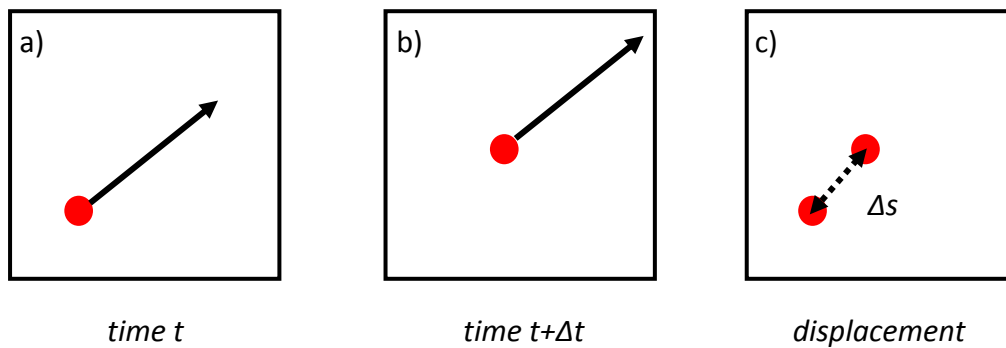


Figure 8. a) shows a tracing particle at time t ; b) the particle moves to another position at time $t+\Delta t$; c) the displacement during the Δt is obtained.

Specific issues of microPIV are also widely discussed, including the flow-tracing particles, fluorescence and the image averaging techniques. There are several requirements for the tracing particles. First of all, the particles are supposed to have the same density as the

working fluid so that it can suspend in the fluid evenly. Secondly, the size of the particle should be small enough to avoid influencing the flow motion; while at the same time should be big enough to emit sufficient light for the image recording, and to maximally decrease the effect of Brownian motion. Thirdly, they should have a sufficiently high light scattering efficiency. Usually high numerical aperture objective lenses are used to capture the emitted light signal as much as possible.

Solid tracing particles are commonly used in hydrodynamic measurements, such as polystyrene and nylon particles, aluminum, and fluorescent particles. Commercial high-quality solid tracing particles developed specifically for microPIV measurements are available from several companies like Kanomax, TSI and Invitrogen, although the prices are usually expensive.

Considering the Brownian motion resulted from the particle sizes of several hundreds of nanometers to several microns, special image analysis technique is required to process the microPIV images. Santiago [4] reported a double-frame cross-correlation algorithm for the vector fields analysis in his first microPIV study of the an elliptical cylinder with diameter of 30 μm . The algorithm calculates the correlation values of the two corresponding interrogation windows. The peak value of the correlation plane is then identified as the means displacement of the particles, and the displacement vectors are then transformed to an instantaneous velocity map.

More advanced optional algorithms are also available in microPIV, such as sum-of-correlation, which is more suitable under the circumstance of low seeding densities and low signal-to-noise ratios [9]. In addition to the image analysis algorithm, specific pre/post processing is also required to minimize the background noise in the image and to improve the data.

In this study, the illumination of the micro-channel was provided by a double-pulsed Nd:YAG Continuum Minilite laser. The working fluids were seeded with 1 μm diameter fluorescent Nile red flow-tracing particles (Nile red FluoSpheres, Invitrogen Corporation). The weight concentration of the particle solution is 0.02% to provide a sufficient particle density for flow velocity tracking [10]. Flow images were captured by a LaVision Imager Intense CCD camera. In this study, a 40 \times 0.6 NA objective was coupled with a 0.45 \times coupler, resulting in a total magnification of 18 \times and a depth of correlation of 4.2 μm [11]. Interrogation windows of 32 \times 32 pixels were chosen. The overlapped area of adjacent interrogation windows is 50%. Delay time of the double-pulsed laser was adjusted at each depth so that the tracing particles move approximately $\frac{1}{4}$ of the interrogation window between the two exposures. 500 microPIV images were acquired at each location and analyzed using the sum of correlation algorithm. Velocity fields were measured at 9 height levels inside the rectangular channel with 5 μm increment between. Three experimental sets were repeated on each channel. Flow rates of 0.1 ml/min and 0.01 ml/min were used in this study.

Velocity fields were computed from the image sets using sum of correlation algorithm. Streamwise and transverse velocities were exported from the velocity field and processed in Matlab. Plane fit was applied to the data to remove the plane resulted un-horizontal effect of the microPIV work station.

2.5 References

1. Ren, J., B. Ganapathysubramanian, and S. Sundararajan, *Experimental analysis of the surface roughness evolution of etched glass for micro/nanofluidic devices*. Journal of Micromechanics and Microengineering, 2011. **21**(2).

2. McDonald, J.C., et al., *Fabrication of microfluidic systems in poly(dimethylsiloxane)*. *Electrophoresis*, 2000. **21**(1): p. 27-40.
3. McDonald, J.C. and G.M. Whitesides, *Poly(dimethylsiloxane) as a material for fabricating microfluidic devices*. *Accounts of Chemical Research*, 2002. **35**(7): p. 491-499.
4. Santiago, J.G., et al., *A particle image velocimetry system for microfluidics*. *Experiments in Fluids*, 1998. **25**(4): p. 316-319.
5. Raffel, M., U. Seelhorst, and C. Willert, *Vortical flow structures at a helicopter rotor model measured by LDV and PIV*. *Aeronautical Journal*, 1998. **102**(1014): p. 221-227.
6. Westerweel, J., *Fundamentals of digital particle image velocimetry*. *Measurement Science & Technology*, 1997. **8**(12): p. 1379-1392.
7. Kirby, B.J., ed. *Micro- and Nanoscale Fluid Mechanics: Transport in Microfluidic Devices*. 2010, Cambridge University Press.
8. Nam-Trung Nguye, S.T.W., ed. *Fundamentals and Applications of Microfluidics*. 2002.
9. Burgmann, S., et al., *Analysis of tracer particle characteristics for micro PIV in wall-bounded gas flows*. *Houille Blanche-Revue Internationale De L Eau*, 2011(4): p. 55-61.
10. Bălan Cătălin Mihai, B.C., *μ PIV measurement and numerical computation of the velocity profiles in micro-channels*. *UPB Scientific Bulletin, Series D: Mechanical Engineering*, 2010. **72**(3).
11. Olsen, M.G. and R.J. Adrian, *Measurement volume defined by peak-finding algorithms in cross-correlation particle image velocimetry*. *Measurement Science & Technology*, 2001. **12**(2): p. N14-N16.

CHAPTER 3. EXPERIMENTAL ANALYSIS OF THE SURFACE ROUGHNESS EVOLUTION OF ETCHED GLASS FOR MICRO/NANO FLUIDIC DEVICES

A paper published in *Journal of Micromechanics and Microengineering*

Jing Ren, Baskar Ganapathysubramanian and Sriram Sundararajan

Department of Mechanical Engineering, Iowa State University, Ames, IA 50011, USA

3.1 Abstract

Roughness of channel surfaces, both deterministic and random, is known to affect the fluid flow behavior in micro/nanoscale fluidic devices. This has relevance particularly for applications involving non-Newtonian fluids, such as in biomedical lab-on-chip devices. While several studies have investigated effects of relative large, deterministic surface structures on fluid flow, the effect of random roughness on micro fluid flow remains unexplored. In this study, the effects of processing conditions for wet etching of glass including etching time and etching orientation on central line average (Ra) and the autocorrelation length (ACL) were investigated. Statistical distribution of the roughness was also studied. Results indicated that ACL can be tailored in the range of 1-4 μm by changing etching time in horizontal etching while Ra was found to increase weakly with etching time in all three etching orientations. Analysis of the experimental data using Kolmogorov-Smirnov goodness-of-fit hypothesis test (K-S test) shows that the glass surface roughness does not follow a Gaussian distribution, as is typically assumed in literature. Instead, the T location-scale distribution fits the roughness data with 1.11% error.

These results provide promising insights into tailoring surface roughness for improving microfluidic devices.

Keywords microfluidic device · surface roughness · autocorrelation length · surface height distribution · goodness-of-fit test

3.2 Introduction

Extensive studies during the past century indicate that surface roughness affects fluid flow behavior in microscale channels. Numerical simulations of micro flow in rough channels [1] showed that bulk flow velocity and the volumetric flow rate decrease in different rates as the roughness increases. Studies on the effect of surface roughness on friction force [2], pressure drop [3, 4], heat transfer in single-phase flow [5] and laminar-turbulent transition [6] indicate the necessity of precise control of the surface morphology inside the fluidic device for the purpose of enhancing the reliability and performance of the fluidic system [7]. Experimental results of blood flow in rough microchannels [8] emphatically showed that surface roughness affects blood viscosity due to boundary effects. Application of surface roughness for gradient generation in microfluidic system has also been widely studied [9-11].

In most of these studies, researchers relied on micro-machining or micro-fabrication techniques to produce deterministic roughness via designed shapes and patterns inside the microchannels. It is well known that almost all mechanical or chemical processing inherently produces random roughness on real surfaces [12] and consequently most engineering surfaces are random. However, the role of random roughness on microfluidic flow behavior remains

relatively unexplored. This aspect will become increasingly important as channel sizes continue to decrease in micro/nanofluidic applications.

In most microfluidic studies, surface roughness is described using only amplitude parameters such as relative roughness [1, 13, 14]. Spatial parameters such as autocorrelation length (ACL) or power spectral density function (PSDF) are rarely used. It is widely known that most important features of random surface roughness can be characterized by amplitude and spatial parameters [15]. Surfaces with identical amplitude parameters can have totally different topographical features that however can be characterized by differences in spatial parameters. A knowledge of both amplitude and spatial parameters can lead to methods to tailor random roughness [16].

The distribution of surface heights is another important aspect in surface roughness study. Surface height distribution is typically related to the nature of the processing method (Bhushan 2001). In most studies random roughness is assumed to possess a Gaussian or Uniform distribution [17-22]. Relatively few works attempt to experimentally verify this assumption for the processed surfaces involved. Zimmer et al. verified a Gaussian distribution for laser-induced backside wet etching on fused silica [23]. Suh and Polycarpou investigated the use of various density functions to describe textured surfaces in magnetic-storage devices [24]. Some chemically and mechanically processed surfaces were proved to be non-Gaussian and even anisotropic [25-28]. It has to be emphasized that the exact height distribution of random surfaces prepared for microfluidic devices has not been reported earlier.

In this paper, random roughness on glass substrates is created by chemical etching. Glass is one of the more important and common materials widely used in micro channel fabrication

[29]. Evolution of amplitude parameter Ra and spatial parameter ACL with etching time and orientation is investigated. Kolmogorov-Smirnov goodness-of-fit hypothesis test is used to verify the approximate distribution of the surface heights.

3.3 Experimental procedure

The surface roughness examined in this study was generated on glass slides (25 mm × 75 mm, Erie Scientific Company, Portsmouth, NH). The glass samples were etched by buffered HF (6:1 volume ratio of 40% NH₄F in water to 49% HF in water) to generate different surface roughness. The etch rate was calibrated as 72 nm/min. Samples were immersed in buffered HF in three different orientations: horizontal, 45° and vertical. In each orientation, samples were prepared at several different etching times. Since the study is focused on how etching condition affects surface roughness for microfluidic applications, the glass surfaces etched by HF should be suitable for micro channel fabrication and further microfluidic experimental techniques, such as Particle Image Velocimetry (PIV), which requires superior channel transparency. Based on our experimental observation, etching times longer than 40 minutes in horizontal orientation resulted in significant surface damage on glass substrate, which led to difficulty in bonding during microchannel fabrication. Furthermore, transparency of the glass surface was significantly compromised. Therefore, in this study the maximum etching time reported is 40 minutes. Two samples were prepared for each etching condition. After HF etching, the samples were rinsed in DI water for 5 minutes and dried by nitrogen. Two smooth (un-etched) glass slides were also prepared for comparison.

An atomic force microscope (AFM, Dimension 3100, Nanoscope IV, Veeco Instruments, Santa Barbara) was used to measure surface roughness of the etched glass samples. All the

etched samples were cleaned in acetone and dried by nitrogen to remove organic waste and dust on the surface before taking AFM images. All the AFM scans were acquired in contact mode using a standard Si₃N₄ tip, at a scan resolution of 256×256 points. The scan size was chosen as 75 μm × 75 μm which is comparable to the common size of microchannels used for microfluidic study. Scan areas were chosen to avoid edges of the slides to ensure valid roughness information. As shown in figure 1, each slide was scanned by AFM from bottom to top in five areas to ensure the overall surface roughness information was obtained. Three AFM images were taken in each area, leading to 15 scans for each glass slide and 30 scans for each etching/orientation condition. The AFM surface height data was exported into MATLAB to analyze surface height distribution and to compute amplitude (Ra) and spatial (ACL) roughness parameters.



Figure 1. A schematic representing the scanned regions of each glass slide. Three AFM scans (75 μm × 75 μm) were acquired in each area to ensure roughness information was obtained over the entire slide.

Center line average (Ra) is the arithmetic mean of the absolute values of vertical deviation from the mean line of the profile which measures the relative departure of the profile in the vertical direction [30]. Ra is calculated as

$$Ra = \frac{1}{N} \sum_{i=1}^N |z_i - m| \quad (1)$$

where N is the number of total sampling points, z is the surface height, m is mean line of the surface profile.

Autocorrelation length (ACL) measures the degree of randomness of the surface roughness, and represents the distance over which two points can be treated as independent in a random process [31]. It is defined as the length over which the autocorrelation function decays to a small fraction of its original value. Many etched surfaces are widely assumed to produce an exponential autocorrelation function [30] given as

$$c(\tau) = \exp(-\tau / \beta) \quad (2)$$

where τ is the spatial separation. Autocorrelation length of this exponential autocorrelation function is defined as the distance at which value of the $C(\tau)$ drops to $1/e$ of the initial value, which is equal to β [32].

Surface height distribution (fitting hypothesis) of the etched glass was validated by the Kolmogorov-Smirnov (K-S) goodness-of-fit test. Details of K-S test procedure are attached in appendix. Here we describe our rationale for sample size selection for the test. The size of the AFM surface roughness height data for each scan is 256×256 . Usually, for small population sizes (<5000), a few dozen data are used for the K-S test. The standard K-S test was designed for

small sample sizes (~100) [33, 34]. Studies have verified that for very large populations, as is the case of our surface roughness data, the choice of sample size will have an effect on the test outcomes. As sample size decreases, goodness-of-fit test is less likely to perform poorly [35]. Determining the exact sample size needed for a given population size is still an open problem. In our study, 100 data was randomly collected from each experimental scan to run the test for both Gaussian and T location-scale fit. 1000 such tests were then executed for each scan to minimize the effect of any sampling bias. Confidence interval used in the test was 95%. Success rate of the 1000 tests was recorded.

3.4 Results and discussion

3.4.1 Surface roughness parameters

Representative AFM images obtained from horizontally etched glass surfaces are shown in Figure 2. Samples etched in the other two directions presented similar surface morphology changes as etching time increases up to 30 minutes. In horizontal etching, when etching time increases to 40 minutes, spreading holes and grooves appeared on the surface which drastically increase the Ra as shown in Figure 2. Noticeable side peaks appear in the AFM image indicating that the surface is becoming less isotropic. Samples became visibly rugged and dark in areas around the surface and were subsequently found to be unsuitable for microchannel fabrication due to poor transparency and bonding. In 45° etching, visible damage also occurred on the surfaces but was less severe. Interestingly, samples etched in vertical orientation did not exhibit this visible damage on the surface.

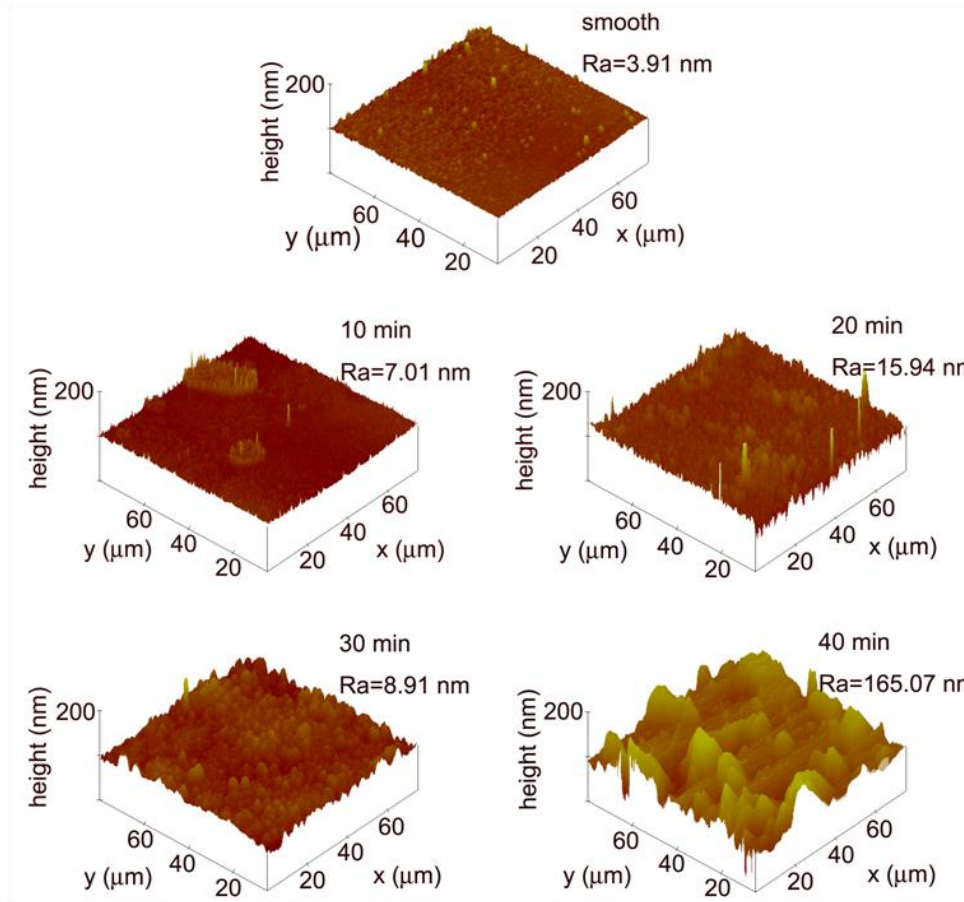


Figure 2. Representative AFM surface height images of horizontally etched glass. The surface morphology changes as etching time increases. When etching time increases to 40 minutes, the roughness increases drastically rendering the surface unsuitable for microchannel fabrication.

Center-line average

Figure 3 shows the effect of etching time on the amplitude parameter Ra for all three etching orientations.

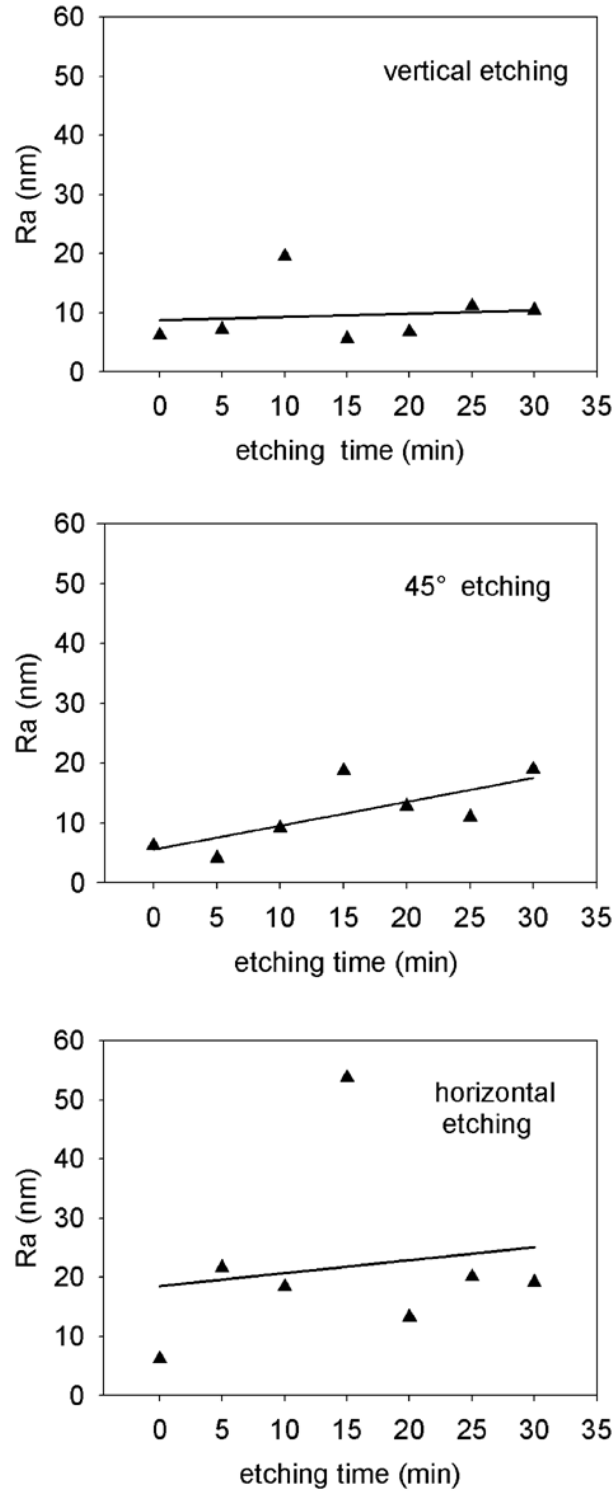


Figure 3. Variation of Ra with etching time in different etching orientations. The data suggest a slight increase of Ra with etching time. In 45° etching, Ra increases with etching time at a faster rate than in the other two orientations. However no strong trends were observed with regression analysis.

The data suggest a slight increase in Ra with etching time. Regression analysis indicated a stronger linear trend ($R^2 = 0.565$) for 45° etching, as compared to horizontal and vertical orientations ($R^2 < 0.1$ for both). The data suggest that generally higher variation in Ra values can be obtained by using horizontal etching, but precise tailoring is subtle under 30 minutes etching time. As discussed earlier, longer etching times resulted in substantial increase in Ra values and poor bonding during microchannel fabrication. For example, in horizontal etching, an etching time of 40 minutes results in a drastic increase in Ra to 149.14 nm compared to less than 60 nm for the other two etching orientations.

Autocorrelation length

Figure 4 shows the ACL evolution with etching time for the three different etching orientations. In vertical etching, ACL value appears to be independent of etching time in our time range. In 45° etching, linear regression shows a slight increase of ACL from 1 μm to 4 μm with etching time, while in horizontal etching, ACL value shows a much faster increase from 1 μm to 4 μm starting from 10 minutes. Therefore, as the etching orientation switching from vertical to horizontal gradually, ACL value shows increasingly obvious trend with etching time. According to the predicted behavior represented by the trend lines, ACL value can be tailored in the range of 1 μm to 4 μm in horizontal etching by controlling etching time.

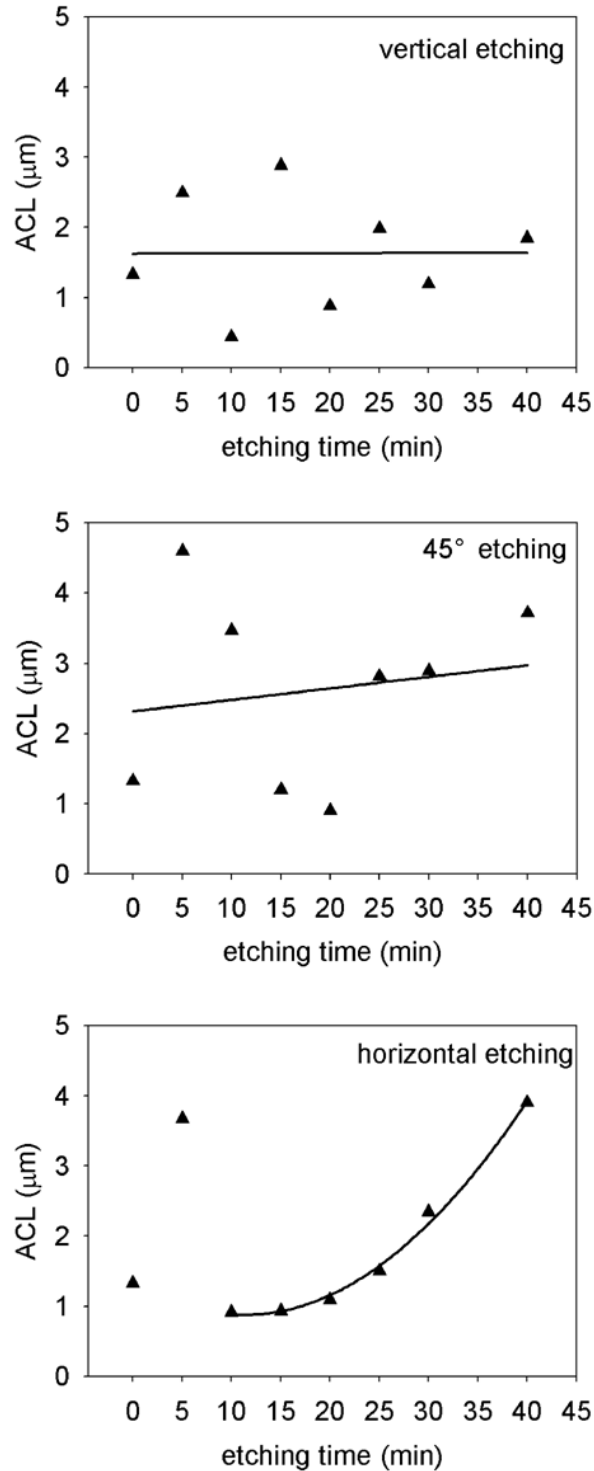


Figure 4. Variation of ACL with etching time in different orientations along with best-fit trend lines. In vertical etching, ACL value is independent of etching time. In 45° etching, ACL value shows a slight increase from 1 μm to 4 μm . In horizontal etching, the increasing behavior is more obvious.

3.4.2 Surface height distribution

Figure 5 shows representative histograms of AFM roughness height data at different etching times in horizontal etching. Statistical distribution of etched material surface has been assumed to be Gaussian in published literature [17, 18]. However, Figure 5 shows that the histogram of the AFM surface height data appears to be more heavy-tailed than Gaussian. We tried to describe the data with other distributions that fit leptokurtic data with heavy tails. T location-scale distribution is more appropriate than Gaussian distribution for modeling data with heavy tails, which is the case in the glass surface roughness height data. The probability density function of T location-scale distribution is defined as:

$$f(x) = \frac{\Gamma\left(\frac{\nu+1}{2}\right)}{\sigma\sqrt{\nu\pi}\Gamma\left(\frac{\nu}{2}\right)} \left[\frac{\nu + \left(\frac{x-\mu}{\sigma}\right)^2}{\nu} \right]^{-\left(\frac{\nu+1}{2}\right)} \quad (3)$$

where Γ is the gamma function, and μ , σ , and ν are mean, standard deviation and degree of freedom, respectively [36]. Figure 5 also shows both Gaussian and T location-scale fits for height data. It can be seen that compared with the Gaussian distribution, T location-scale distribution reproduces the data histogram much better in each case. The other two etching orientations also show similar behavior with the T location-scale showing a much better fit.

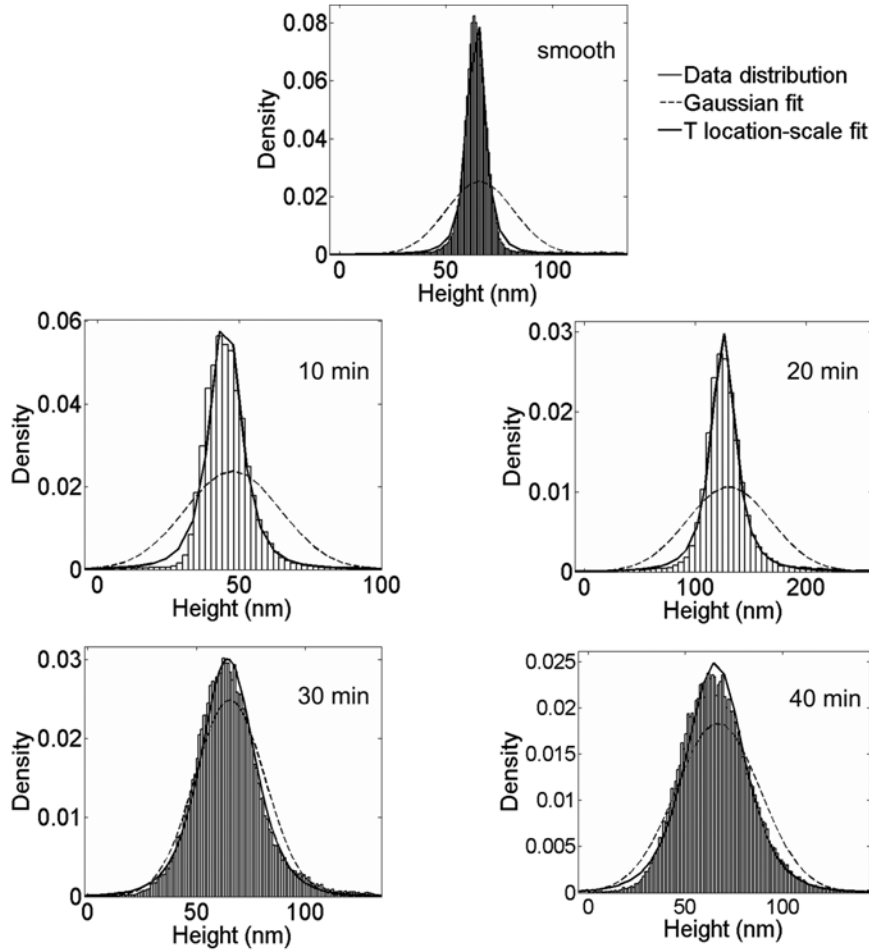
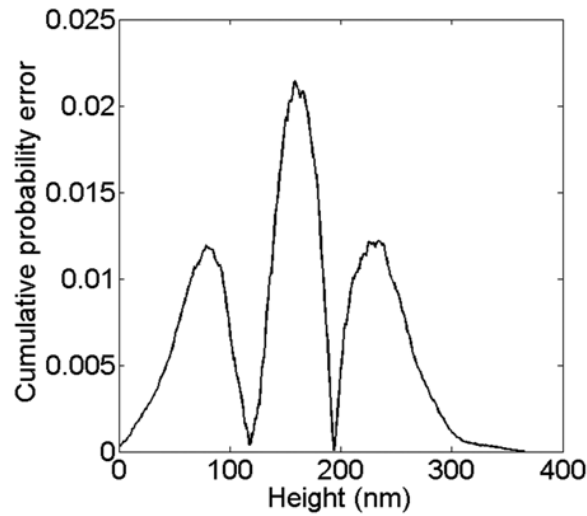


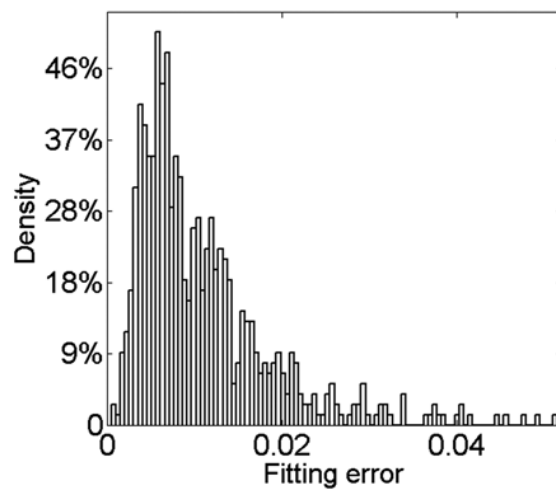
Figure 5. Histograms of the surface height data for horizontally etched glass surfaces at different etching times. Also shown are Gaussian and T location-scale fits of the data. T location-scale distribution fits the data better than Gaussian distribution.

In order to verify the hypothesis that the AFM surface height data follows a T location-scale distribution rather than a Gaussian distribution, the Kolmogorov-Smirnov (K-S) goodness-of-fit test was executed on both fitted distributions. Result of the test showed average success rate of Gaussian distribution fitting to be 0, which means Gaussian distribution fails to fit any of the surface roughness height data. In contrast, the average success rate of T location-scale distribution fitting was 95.5%, indicating an excellent fit between a T location-scale distribution and the experimental data at a 95% confidence interval.

For each data set, an error which is defined as the discrepancy between the empirical cumulative distribution function (CDF) and theoretical CDF of T location-scale distribution, was computed. Figure 6 (a) shows this error of a representative AFM roughness height data set. It can be seen that the error is less than 2.5%. Figure 6 (b) shows the histogram of average fitting error for all the 617 experimental data sets. The average fitting error is about 1.11% while most of the error is less than 2%, which validates the T location-scale distribution as a good fit to the surface height data.



(a)



(b)

Figure 6. Error between empirical CDF of the surface roughness height data and theoretical CDF of a T location-scale distribution: (a) error for one experimental data set; (b) histogram of fitting error for all the 617 experimental data sets.

3.5 Conclusions

In this paper, surface roughness was generated on glass substrate by buffered HF etching and measured by Atomic Force Microscopy. Evolutions of roughness parameters Ra and ACL were characterized as function of etching time and orientation. In addition, the height distribution of the etched glass surface was also analyzed.

The etching orientation of the glass slides affects the evolution of the roughness in addition to etching time. Spatial parameter ACL increases roughly from 1 μm to 4 μm in both 45° and horizontal etching. ACL value shows a weak linear increase with time in 45° etching, and a much faster and predictive increase in horizontal etching, while vertical etching has no discernible effect. This evolution behavior provides a potential way to tailor the random roughness of glass surface in HF etching by controlling etching time and orientation simultaneously. The amplitude parameter Ra shows a weak linear increase with etching time in all etching orientations.

Analysis of the height distribution showed that the etched glass surfaces were non-Gaussian. Instead, a T location-scale distribution was demonstrated to fit the AFM surface height data. In addition, for large data set modeling, the effect of sample size selection on the outcome of goodness-of-fit test needs to be examined.

Evolution of surface roughness with etching time and orientation brings insights into the possibility of tailoring random roughness for designed microfluidic flow performances.

Furthermore, the surface height distribution studied in this paper provides a basis for modeling and analysis of random rough surface and simulations of fluid flow in microscale rough channels.

Current and future work on this study will be to extend surface roughness analysis of other pertinent materials for microfluidic device fabrication, such as silicon, as well as assessing the impact of random roughness on laminar microfluidic flow using particle image velocimetry (PIV) technique [37].

3.6 Acknowledgement

The authors would like to thank Chris Tourek, a Mechanical Engineering graduate student at Iowa State University for assistance with using the AFM in this study.

3.7 Appendix

K-S test is widely used to decide if a sample comes from a population with a specific distribution [38]. It is based on testing the maximum distance between the empirical cumulative distribution function (empirical CDF) and the theoretical cumulative distribution function (theoretical CDF). If the AFM surface height data follows a certain distribution, the empirical CDF is expected to be very close to the theoretical CDF of the specified distribution, e.g. T location-scale distribution. If the distance is not small enough, the hypothesis that the data follows the specific distribution will be considered incorrect and rejected. The test was executed on both Gaussian and T location-scale fitting.

Process of Kolmogorov-Smirnov test for AFM surface height data:

H_0 : The height data is drawn from T location-scale distribution.

H_a : The height data is not drawn from T location-scale distribution.

Test Statistic: the Kolmogorov-Smirnov test statistic is defined as $D_n = \sup_x |S_n(x) - F_x(x)|$
 $D_{n,m} = \sup |S_m(x) - S_n(x)|$, where $S_n(x)$ is the empirical CDF of the sample and $S_n(x)$ is the theoretical CDF.

Significance level: $\alpha = 0.05$. If D_n does not exceed the critical value, the null hypothesis is true and we can conclude that the height data is drawn from the expected distribution. If D_n exceeds the critical value, the null hypothesis is rejected.

3.8 References

1. Yang, D.Y. and Y. Liu, *Numerical simulation of electroosmotic flow in microchannels with sinusoidal roughness*. Colloids and Surfaces a-Physicochemical and Engineering Aspects, 2008. **328**(1-3): p. 28-33.
2. Palasantzas, G. and A. Widom, *Roughness effects on the sliding frictional force of submonolayer liquid films on solid substrates*. Physical Review B, 1998. **57**(8): p. 4764-4767.
3. Kandlikar, S.G., et al., *Characterization of surface roughness effects on pressure drop in single-phase flow in minichannels*. Physics of Fluids, 2005. **17**(10).
4. Bahrami, M., M.M. Yovanovich, and J.R. Culham, *Pressure drop of fully developed, laminar flow in rough microtubes*. Journal of Fluids Engineering-Transactions of the Asme, 2006. **128**(3): p. 632-637.
5. Kandlikar, S.G., S. Joshi, and S.R. Tian, *Effect of surface roughness on heat transfer and fluid flow characteristics at low Reynolds numbers in small diameter tubes*. Heat Transfer Engineering, 2003. **24**(3): p. 4-16.

6. Hao, P.F., et al., *Experimental investigation of water flow in smooth and rough silicon microchannels*. Journal of Micromechanics and Microengineering, 2006. **16**(7): p. 1397-1402.
7. Komvopoulos, K., *Surface engineering and microtribology for microelectromechanical systems*. Wear, 1996. **200**(1-2): p. 305-327.
8. Prentner, S., et al., *Effects of Channel Surface Finish on Blood Flow in Microfluidic Devices*. Dtip 2009: Symposium on Design, Test, Integration and Packaging of MemS/Moems, 2009: p. 51-54
- 429.
9. Kang, T., J. Han, and K.S. Lee, *Concentration gradient generator using a convective-diffusive balance*. Lab on a Chip, 2008. **8**(7): p. 1220-1222.
10. Keenan, T.M. and A. Folch, *Biomolecular gradients in cell culture systems*. Lab on a Chip, 2008. **8**(1): p. 34-57.
11. Lin, F., et al., *Generation of dynamic temporal and spatial concentration gradients using microfluidic devices*. Lab on a Chip, 2004. **4**(3): p. 164-167.
12. Thomas, T.R., *Rough surfaces*. 1999: Imperial College Press.
13. Taylor, J.B., A.L. Carrano, and S.G. Kandlikar, *Characterization of the effect of surface roughness and texture on fluid flow - past, present, and future*. International Journal of Thermal Sciences, 2006. **45**(10): p. 962-968.
14. Rawool, A.S., S.K. Mitra, and S.G. Kandlikar, *Numerical simulation of flow through microchannels with designed roughness*. Microfluidics and Nanofluidics, 2006. **2**(3): p. 215-221.
15. Hu, Y.Z. and K. Tonder, *Simulation of 3-D Random Rough-Surface by 2-D Digital-Filter and Fourier-Analysis*. International Journal of Machine Tools & Manufacture, 1992. **32**(1-2): p. 83-90.
16. Zhang, Y.L. and S. Sundararajan, *Method to generate surfaces with desired roughness parameters*. Langmuir, 2007. **23**(16): p. 8347-8351.
17. Lu, J.Q., A.A. Maradudin, and T. Michel, *Enhanced backscattering from a rough dielectric film on a reflecting substrate*. Journal of the Optical Society of America B-Optical Physics, 1991. **8**(2): p. 311-318.
18. Payne, A.P. and B.M. Clemens, *Influence of Roughness Distributions and Correlations on X-Ray-Diffraction from Superlattices*. Physical Review B, 1993. **47**(4): p. 2289-2300.
19. Lin, G., C.-H. Su, and G.E. Karniadakis, *Random Roughness Enhances Lift in Supersonic Flow*. Physical Review Letters, 2007. **99**(10): p. 104501.
20. Lin, G., C.H. Su, and G.E. Karniadakis, *Stochastic modeling of random roughness in shock scattering problems: Theory and simulations*. Computer Methods in Applied Mechanics and Engineering, 2008. **197**(43-44): p. 3420-3434.

21. Tartakovsky, D.M. and D. Xiu, *Stochastic analysis of transport in tubes with rough walls*. Journal of Computational Physics, 2006. **217**(1): p. 248-259.
22. Ganapathysubramanian, B. and N. Zabarar, *Sparse grid collocation schemes for stochastic natural convection problems*. Journal of Computational Physics, 2007. **225**(1): p. 652-685.
23. Zimmer, K., R. Bohme, and B. Rauschenbach, *Using IR laser radiation for backside etching of fused silica*. Applied Physics a-Materials Science & Processing, 2007. **86**(3): p. 409-414.
24. Suh, A.Y. and A.A. Polycarpou, *Modeling of the effect of preferential texturing on the interfacial forces in sub-5 nm ultralow flying head-disk interfaces*. Journal of Tribology-Transactions of the Asme, 2007. **129**(3): p. 553-561.
25. Chilamakuri, S.K. and B. Bhushan, *Contact analysis of non-Gaussian random surfaces*. Proceedings of the Institution of Mechanical Engineers Part J-Journal of Engineering Tribology, 1998. **212**(J1): p. 19-32.
26. Lee, H.J., Y.B. Chen, and Z.M. Zhang, *Directional radiative properties of anisotropic rough silicon and gold surfaces*. International Journal of Heat and Mass Transfer, 2006. **49**(23-24): p. 4482-4495.
27. Zhu, Q.Z. and Z.M. Zhang, *Anisotropic slope distribution and bidirectional reflectance of a rough silicon surface*. Journal of Heat Transfer-Transactions of the Asme, 2004. **126**(6): p. 985-993.
28. Zhu, Q.Z. and Z.M.M. Zhang, *Correlation of angle-resolved light scattering with the microfacet orientation of rough silicon surfaces*. Optical Engineering, 2005. **44**(7): p. -.
29. Zhang, X.L. and S.J. Haswell, *Materials matter in microfluidic devices*. Mrs Bulletin, 2006. **31**(2): p. 95-99.
30. Bhushan, B., *Modern tribology handbook*. Vol. 1. 2001, Boca Raton: CRC.
31. Zhang, Y.L. and S. Sundararajan, *The effect of autocorrelation length on the real area of contact and friction behavior of rough surfaces*. Journal of Applied Physics, 2005. **97**(10): p. -.
32. Whitehouse, D.J. and J.F. Archard, *The Properties of Random Surfaces of Significance in their Contact*. Proceedings of the Royal Society of London. Series A, Mathematical and Physical Sciences, 1970. **316**(1524): p. 97-121.
33. Ajiferuke, I., D. Wolfram, and F. Famoye, *Sample size and informetric model goodness-of-fit outcomes: a search engine log case study*. Journal of Information Science, 2006. **32**(3): p. 212-222.
34. Strum, D.P., J.H. May, and L.G. Vargas, *Modeling the uncertainty of surgical procedure times - Comparison of log-normal and normal models*. Anesthesiology, 2000. **92**(4): p. 1160-1167.
35. Zhu, B.P., et al., *Factors affecting the performance of the models in the mortality probability model II system and strategies of customization: A simulation study*. Critical Care Medicine, 1996. **24**(1): p. 57-63.

36. J. K. Ghosh, M.D., Tapas Samanta, *An introduction to Bayesian analysis: theory and methods*. 2006: Springer.
37. Ren, J., et al. *Effect of channel surface roughness on microfluidic flow velocity*. in *47th Annual Technical Meeting of Society of Engineering Science*. 2010. Ames, IA.
38. Massey, F.J., *The Kolmogorov-Smirnov Test for Goodness of Fit*. Journal of the American Statistical Association, 1951. **46**(253): p. 68-78.

CHAPTER 4. A HYBRID SURFACE TAILORING PROCESS TO GENERATE NANOSCALE RANDOM ROUGHNESS ON MATERIALS FOR MICROFLUIDIC APPLICATIONS

A paper submitted to *Journal of Micromechanics and Microengineering*

Jing Ren and Sriram Sundararajan*

Department of Mechanical Engineering, Iowa State University, Ames, IA 50011, USA

**E-mail: srirams@iastate.edu*

4.1 Abstract

The fabrication processes involved in generating microfluidic channels result in random roughness at the nanoscale. As the size of modern microfluidic devices continue to shrink, the effect of this nanoscale surface roughness on the flow behavior becomes increasingly important, especially for applications involving non-Newtonian fluids, such as biomedical lab-on-chips. In this paper, a hybrid surface texturing process to tailor nanoscale random roughness on quartz glass substrate is described. The process combines colloidal masking using polystyrene particles and reactive ion etching to generate the final surfaces, where the roughness is created and controlled by the particle diameter and coverage. A large range of particle coverage was achieved through dip coating and drop casting. The randomness of the amplitude and spatial distribution of the final surface data as measured using atomic force microscopy was tested and confirmed. Analysis of the roughness showed that the process is capable of tailoring amplitude roughness

(center-line-average Ra) in the range of 50-190 nm , and spatial parameter autocorrelation length from 1 to 14 μm . A mathematical model was developed to predict the relation between roughness parameters and processing parameters, which agreed well with the experimental results.

Keywords random roughness · roughness tailoring · autocorrelation length · center-line average · quartz · microfluidic device

4.2 Introduction

Extensive studies during the past few decades indicate that surface roughness affects fluid flow behavior in microscale channels. Numerical simulations of micro flow in rough channels [1] showed that bulk flow velocity and the volumetric flow rate decrease in different rates as the roughness increases. An experimental study showed that small levels of roughness (relative roughness of 1%) results in a dramatic decrease in apparent viscosity of horse blood [2]. A recent study reported that nanoscale surface roughness (relative roughness less than 0.01%) has a measurable impact on the transverse velocity perturbations in microfluidic channels for the laminar conditions [3]. Studies on the effect of surface roughness on friction force [4], pressure drop [5, 6], heat transfer in single-phase flow [7, 8] and laminar-turbulent transition [9, 10] indicated the necessity of precise control of the surface morphology inside the fluidic device for the purpose of enhancing the reliability and performance of the fluidic system [11].

However, most studies focus on the flow effects in relation to periodic surface obstructions [12-14]. The substrate materials were mostly processed by micro-machining or micro-fabrication techniques and the surface roughness was formed by repeated shapes and patterns, which is usually large and deterministic. It is well known that almost all mechanical or chemical processing inherently produces random roughness on realistic surfaces and

consequently most engineering surfaces are random [15]. Few studies have reported the impact of small scale random roughness on microfluidic flow behavior. A recent study combining experimental microPIV data and CFD simulation revealed that nanoscale surface roughness causes flow perturbations that extend up to the center plane of a microfluidic channel of $50 \mu\text{m}$ in height [3]. Research has also shown that increasing random surface roughness enhances local Nusselt number in the thermally developing regime in laminar flow [16]. In addition, as surface roughness increases, earlier laminar-turbulent transition at lower Reynolds number occurs [10]. The effect of nanoscale surface roughness on microchannel flow will become increasingly important as micro/nanofluidic device sizes continue to decrease in lab-on-chip applications [17, 18].

In order to study the effect of realistic surface roughness on microfluidic flow behavior, random roughness needs to be generated and tailored inside microfluidic channels on micro/nano scale. An experimental study [19] showed that hydrofluoric etching is capable of generating roughness on glass substrate in a certain range: autocorrelation length increases in the range of 1 to $4 \mu\text{m}$. In addition, the surface height can be characterized by a T location-scale distribution. Nevertheless, etch rate of the chemical wet etching is high and dependent on many factors such as crystallographic orientation, etchant concentration and temperature. These factors increase the difficulty to control the etching process. Compared to wet etching, dry etching is another widely used microfabrication technique [20] which can provide high aspect ratio and precise etch rate.

In this paper, we report a hybrid surface texture tailoring method which combines reactive ion etching and colloidal masking in order to produce random surfaces with desired roughness parameters at the micro/nano scale. The process is demonstrated and analyzed for a quartz substrate, which is a common material for microfluidic device fabrication.

4.3 Experimental Procedure

Figure 1 shows the schematic of the hybrid etching process. First, microparticles are randomly deposited on a quartz substrate using dip coating or drop casting to form a monolayer coating. Next, the substrate is etched using reactive ion etching (RIE), during which the particles serve as temporary masks to protect the area beneath. As a result, the areas uncovered by the particles are etched away first and pillar-shape hillocks are formed at the particle locations. By varying the particle diameter and deposition time, the diameter and surface coverage of the quartz pillars are changed respectively. Details of the process are described below.

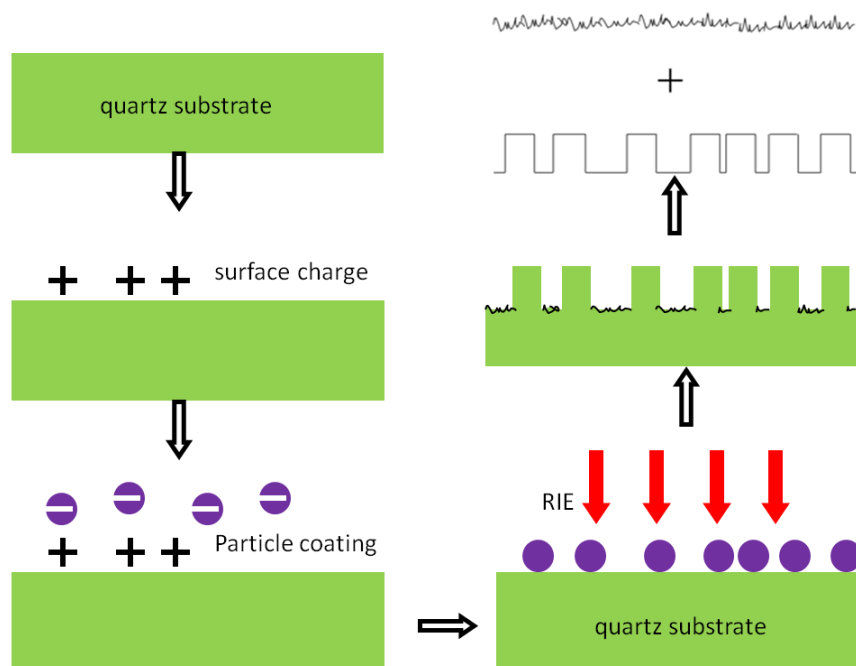


Figure 1. Schematic of the hybrid process used involving random deposition of polystyrene particles onto a substrate followed by reactive ion etching (RIE). The particles act as random masks during the etching process resulting in the final surface, which exhibits pillars corresponding to the particle locations and background roughness from the RIE process.

Prior to particle deposition, quartz slides ($25\text{ mm} \times 25\text{ mm} \times 1\text{ mm}$, Ted Pella, Inc) were cleaned by piranha etch (3:1 mixture of concentrated sulfuric acid to 30% hydrogen peroxide

solution), which resulted in a negatively charged surface [21]. The quartz substrate was coated with a poly(diallyldimethylammonium chloride) (PDDA) monolayer by dipping the slides into 5% PDDA solution, which resulted in a polycationic layer on the surface. Subsequently, a polystyrene colloidal solution (5.0% w/v, Spherotech, Inc) was sonicated for 15 minutes and the particles were deposited onto the quartz slides surface through dip coating or drop casting methods. Polystyrene colloidal solutions with three sets of nominal particle diameters of $1.2\pm 0.2 \mu\text{m}$, $2.7\pm 0.2 \mu\text{m}$ and $5.5\pm 0.5 \mu\text{m}$, respectively was used in this study. During dip coating, the slightly negatively charged particles were absorbed onto the positively charged surface randomly. Dip coating provided good random particle coverage in the range of 5% to 35% via immersion times of 5 minutes to 30 minutes, during which the particle coverage shows a linear increase with immersion time. However, particle agglomeration becomes severe at coverages over 35%. Drop casting on a hotplate was used to achieve higher coverage up to 70% and minimize agglomeration [22]. In drop casting, the quartz substrates were heated to 95 °C on a hotplate, and dilute polystyrene solution (0.05%, 0.1% and 0.5% w/v) was applied to the surface with syringe, resulting in a random coating and wait dry to form a random coating. After particle deposition, the substrates were rinsed in deionized water for 5 seconds to remove the loosely attached particles and dried naturally in room temperature. These methods resulted in particle coverage ranging from around 5% to 70%. While this method reduced the agglomeration up to coverages of 50%, increasing agglomeration was often observed at coverage over 50%. Figure 2 shows coatings resulting from representative particle coverage.

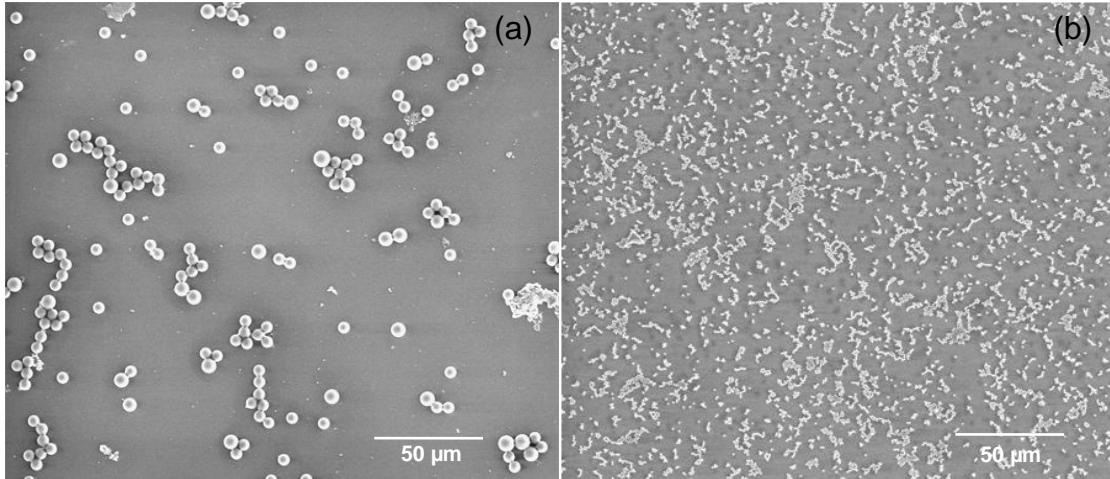


Figure 2. Polystyrene particles deposited onto quartz substrates with (a) particle size of $5.5 \mu\text{m}$ and coverage of 8.5% and; (b) particle size of $1.2 \mu\text{m}$ and coverage of 20.1%.

The coated substrates were then subjected to RIE in a capacitively-coupled plasma (CCP) reactor (PlasmaTherm 790 RIE system). Etching was performed for 6.5 minutes using SF_6 gas at a flow rate of 28 *SCCM*. The base pressure was 0.05 *mTorr*, and the process pressure was 31 *mTorr*. The bias voltage was 500 *V*, and RF power was 420 *W*. These settings resulted in a calibrated etch rate for quartz of about 49 *nm/min*. As a comparison, etch rate of polystyrene with SF_6 gas was reported as about 25 *nm/min* with pressure of 100 *mTorr* and power of 50 *W* [23].

After etching, the remaining particles on the surface were removed by acetone wash for 30 minutes. Figure 3 (a) shows a SEM image of the final surface resulting from particle size of $1.2 \mu\text{m}$. The surface shows the pillar structures due to the particle masking as well as a finer roughness due to the RIE etch of the unmasked quartz surface. The tops of the pillars were roughened by plasma etching, indicating that part of the polystyrene particles did not survive to the end of the etching process. Figure 3 (b) shows a 3D AFM image of a single quartz pillar resulting from masking particle of $2.7 \mu\text{m}$ diameter. The average pillar diameter observed was typically a little smaller than the particle diameter due to particle shrinkage in the plasma

etching. As the polystyrene particles vary in size, the pillar diameter and height change in a certain range correspondingly.

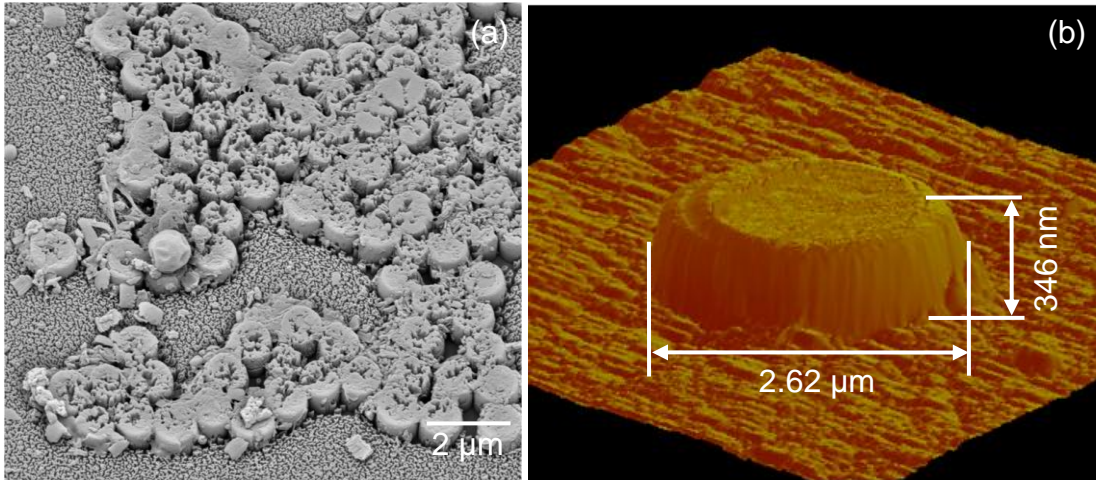


Figure 3. (a) An SEM micrograph of the final surface showing the quartz pillars (formed using particles of $1.2 \mu\text{m}$ diameter). (b) An AFM scan of a single quartz pillar formed by a particle of $2.7 \mu\text{m}$ diameter.

An atomic force microscope (AFM, Dimension 3100, Nanoscope IV, Veeco Instruments, Santa Barbara) was used to measure surface roughness, average height and diameter of the pillars. AFM scans were acquired in contact mode using a standard silicon tip (MikroMasch CSC37 series probe with tip radius of 8 nm), at a scan size was $75 \mu\text{m} \times 75 \mu\text{m}$, and scan resolution of $256 \text{ pixels} \times 256 \text{ pixels}$. The digitized data was exported to analyze the surface randomness and calculate the roughness parameters..

4.4 Result and Discussion

4.4.1 Spatial distribution randomness test

Since the roughness of the processed surface is mainly formed by the quartz pillars resulting from RIE and particle masking, it is necessary to verify the randomness of the pillar

distribution. The pair correlation function $g(r)$ is widely used to study the randomness of physical packing, such as colloidal suspension and random-close-packed particles [24-28]. It is a quantification of the probability density of particles being located in the distance of r from a particle at the coordinate origin. Therefore it can be considered as a measure of spatial ordering of the surface roughness data distribution. The expression of $g(r)$ is given as [29]:

$$g(r) = \frac{S}{2\pi N^2 r} \left[\sum_{i=1}^N \sum_{\substack{j=1 \\ j \neq i}}^N \delta(r - r_{ij}) \right] \quad (1)$$

in which r_{ij} is the vector from point i to point j , S is the total area considered in the data, N is the total number of reference particles considered in the data, and here is the total number detected on one set of digitized data of AFM scan of the surface.

As shown in figure 4, the location of each pillar was detected using bearing height data (refer to section 3.2, figure 7) and circled using a MatLab code. Then the center of the circle was identified and used to locate the position of the pillar. The nearest neighborhood distance was calculated for all the pillars on the surface.

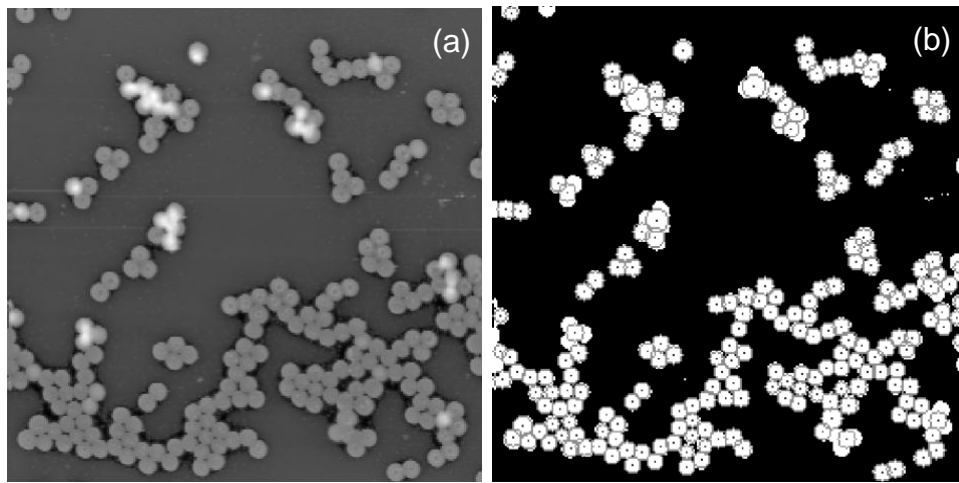


Figure 4. Pillar distribution randomness test methodology: (a) The original image from an AFM scan; (b) pillar detection and circle identification using MatLab.

To calculate the likelihood of finding another pillar within a distance r away from the reference pillar, we count the number of pillars that appear within a resolution distance of $dr=r_0$, where r_0 is the radius of the largest particle in the scanned image. The pair correlation function is obtained by dividing the counts by $2\pi r dr$, which is the area of the ring with resolution of dr . Note that because of the size limit of the image ($256 \text{ pixels} \times 256 \text{ pixels}$), only the particles in the center area (80 pixels away from the edge of the data array) were selected to compute the pair correlation function.

Figure 5 shows that the calculated pair correlation values of the pillar locations on the processed quartz surface shows an exponential decay as a function of r . It has been shown that an exponential decay of the correlations is a characteristic of stochastic or random systems in the studies of physics, mathematics and engineering applications [30-34]. Therefore, it can be concluded from Figure 5 that the pillar locations on the final quartz surface exhibit a stochastic distribution.

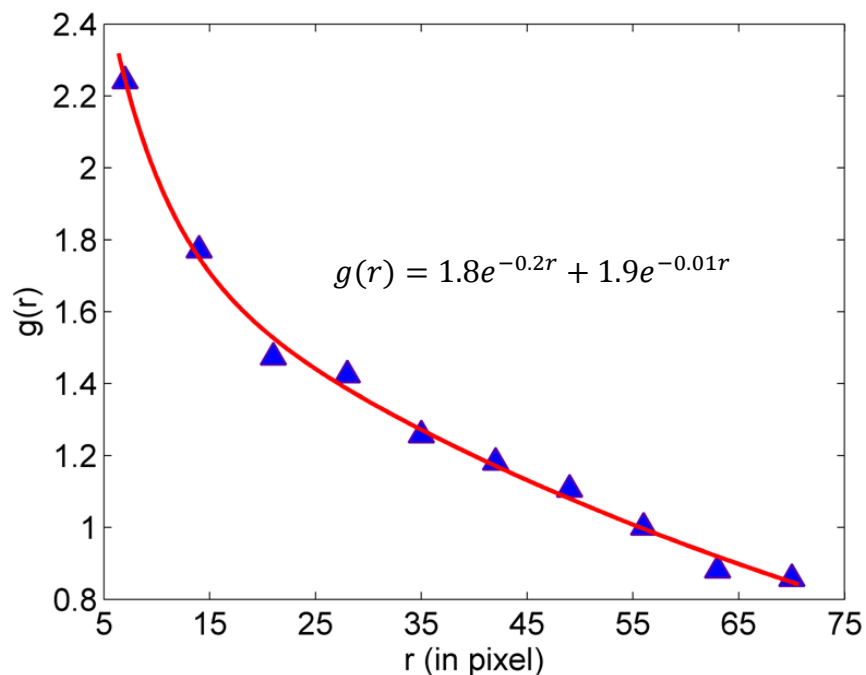


Figure 5. The pair correlation plot of the pillar locations from the experimental data shows an exponential decay with goodness of fit of $R^2=0.99$, indicating a stochastic distribution of the pillar locations on the surface.

4.4.2 Roughness analysis

Generally, surface roughness can be characterized by spatial and amplitude parameters simultaneously [35]. Center-line average (Ra) is one of the mostly commonly used amplitude parameters. Ra is the arithmetic mean of the absolute values of vertical deviation from the mean line of the profile which measures the relative departure of the profile in the vertical direction. The expression of Ra is given by equation 2:

$$Ra = \frac{1}{N} \sum_{i=1}^N |z_i - m| \quad (2)$$

in which N is the number of total sampling points, z_i is the height data, and m is the surface mean line.

According to the treatment process, the final surface can be considered as a sum of two rough surfaces as shown in Figure 4 – one resulting from the pillars (S_1) and the other resulting from the background roughness caused by RIE (S_2). A schematic of a single scan profile of the final surface is shown in figure 6. The pair correlation function evaluation described in the previous section confirmed that the quartz pillars on S_1 are randomly distributed and therefore S_1 can be considered to be a random surface. Anisotropic plasma etching is known to produce surfaces similar to the so-called “grass surface” structure [36, 37], and hence S_2 can also be considered to have a random surface distribution.

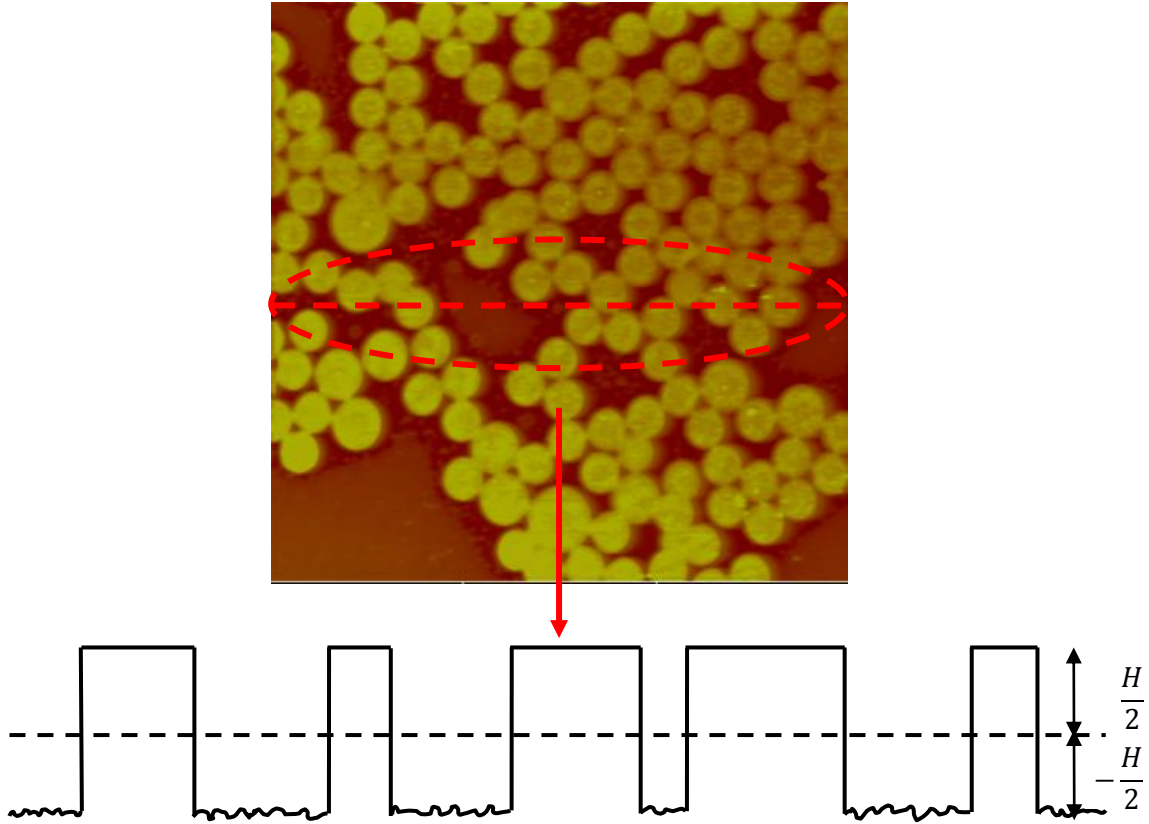


Figure 6. A schematic of a single profile of the final surface showing the combination of pillars and background roughness.

Therefore the local heights z_i of the final surface can be obtained by adding the two random surface heights together [38]:

$$z = z_1 + z_2 \quad (3)$$

If the particle coverage is p , and the average height of the quartz pillars is H , the mean line of the profile can be approximated as:

$$m = (2p - 1) \frac{H}{2} \quad (4)$$

In the experiments with the three sets of particle sizes, the average heights of the quartz pillars were measured as 277 nm, 332 nm and 344 nm, respectively. Local heights z_2 was measured and found to be in the range of 10 nm. Since z_2 is significantly lower than z_1 , we neglect its effect on the amplitude roughness. Therefore the central line average Ra of the final surface can be written as:

$$\begin{aligned} Ra &= p \left(\frac{H}{2} - m \right) + (1 - p) \left(m + \frac{H}{2} \right) \\ &= -2Hp^2 + 2Hp \end{aligned} \quad (5)$$

Particle coverage for the generated surfaces was calculated using Abbott–Firestone curve (or bearing area curve), which is obtained from the AFM surface profile. The Abbott–Firestone curve is a commonly used tool for characterizing random surfaces [39, 40]. It gives the fraction of surface heights which are over a given value. Figure 7 shows the Abbott–Firestone curve of an example roughness data set with 5.5 μm diameter masking particles. Due to the nature of the final surface (formed by pillars and background roughness), the Abbott–Firestone curve shows two major slope increases. The first drop occurs at a normalized height of approximately 0.3 corresponds to the height increase from background surface to the pillars. The second drop corresponds to the height change corresponding to the height of the quartz pillars. Therefore the turning point (obtained as the intersection point of the tangent line fitting of part A and B, marked as in figure 7) is considered as an effective indication of particle coverage.

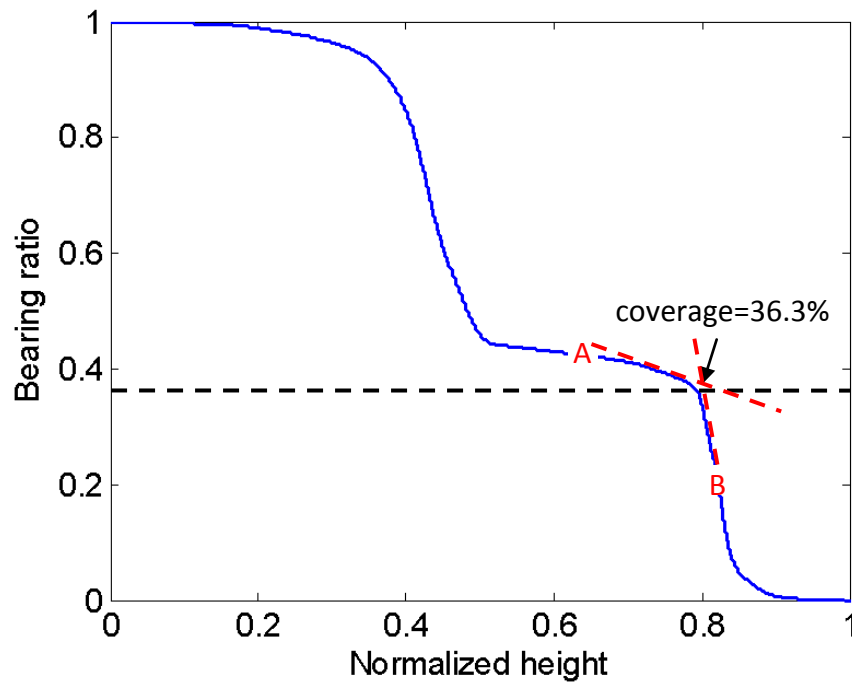


Figure 7. A representative Abbott–Firestone curve of the final surface heights.

Figure 8 shows the Ra of the surfaces generated using $2.7 \mu\text{m}$ diameter particles as well the Ra predicted by equation 5. Uncertainties for the experimental data are also included based on a 90% confidence level. The Ra value from the experiments reaches maximum at about 50% particle coverage, which agrees well with the theoretical prediction. When particle coverage increases beyond 55%, agglomeration of the particles (and hence the pillars) affects the roughness measurement by resulting in a higher mean line m , and thus values that are lower than the theoretical predictions. In addition, agglomeration results in higher uncertainties at high coverages due to the uncertainty in coverage calculation.

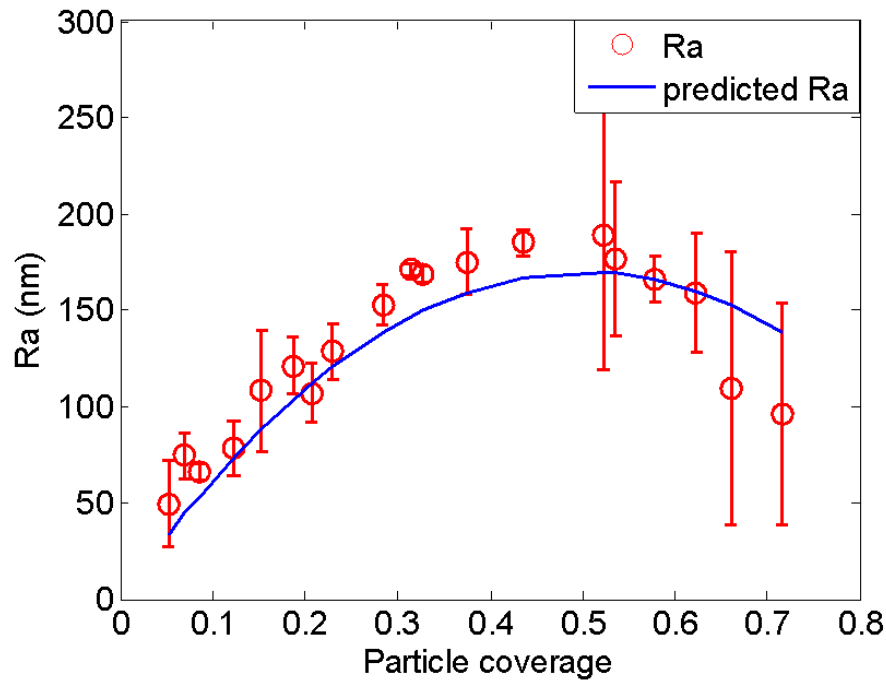


Figure 8. Center-line average (Ra) of the final surfaces (resulted from $2.7 \mu m$ diameter particles) as a function of particle coverage.

Figure 9 shows how particle diameter affects the Ra values as coverage increases. The variation in Ra with coverage obtained from the experiments agrees reasonably well for all three particle diameters. The theoretical prediction shows that Ra will increase with particle diameter (for a given coverage) and this trend is supported by the experimental data. As previously noted, at high coverages, particle agglomeration becomes an issue and experimental results differ from the predictions.

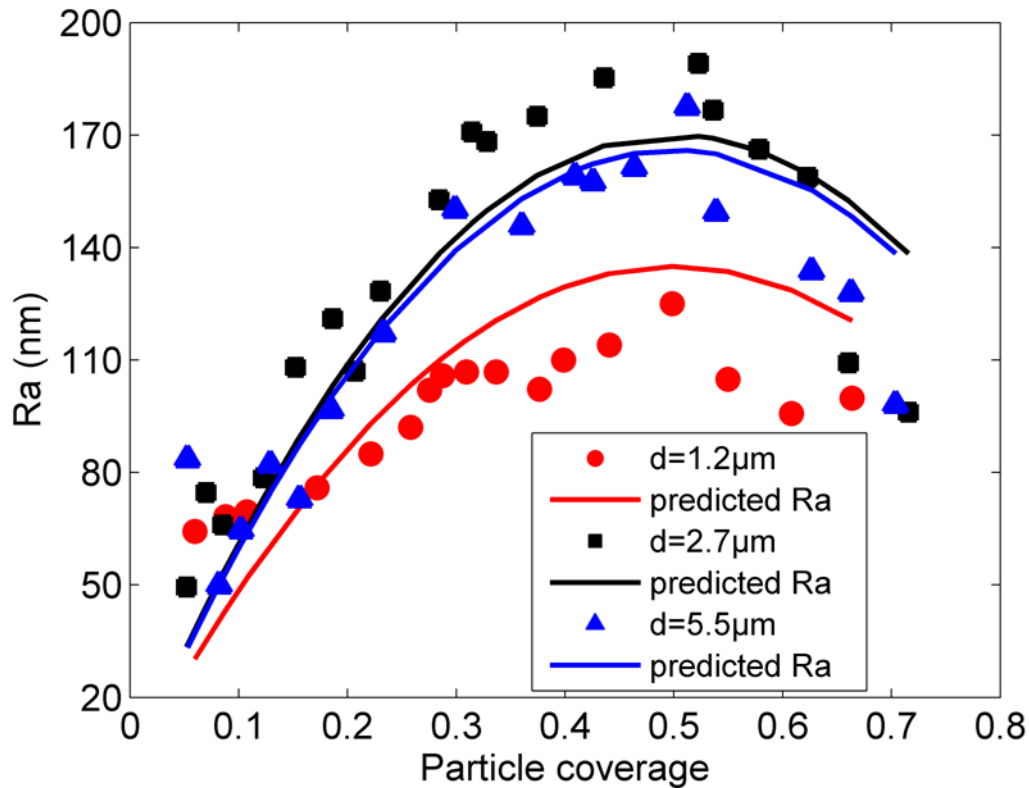


Figure 9. Comparison of center-line average (Ra) of the final surfaces resulted from different particle diameters. The maximum Ra values of all three particle sets are occur at around 50% coverage and follow the predicted curves.

During this process, the $1.2 \mu m$ diameter particles were completely removed by the end of the etching. The 6.5 minutes etching resulted in an average pillar height of $277 nm$. As the particle diameter increases, the pillar height H increases correspondingly as particles still survived on the surface after etching. Pillar heights of $344 nm$ and $332 nm$ were measured when particle diameters are $2.7 \mu m$ and $5.5 \mu m$. Figure 10 shows the Ra evolution with pillar height H . Each Ra value is for a particular particle coverage. The solid line is the predicted Ra using a particle coverage of 20%. Ra shows a linear increase as H increases from $277 nm$ to $344 nm$, which matches the experimental result well.

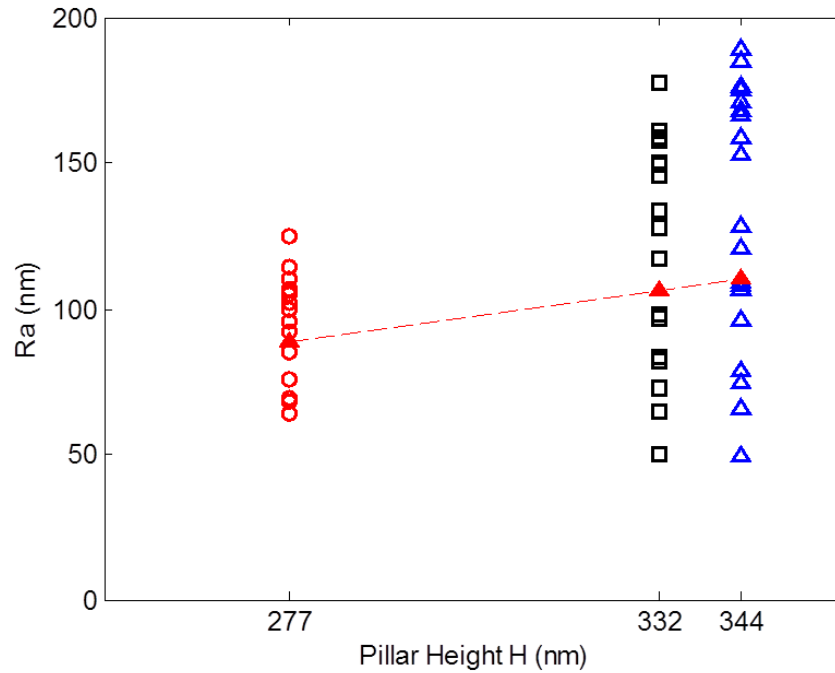


Figure 10. Dependence of center-line average (Ra) on etch depth: 3 particle diameters resulted in different etch depth H . As H increases from 277 nm to 344 nm, Ra shows a slight linear increase.

Autocorrelation length (ACL) is a commonly used spatial roughness parameter, which measures the degree of randomness of the surface roughness, and represents the distance over which two points can be treated as independent in a random process [41]. It is defined as the length over which the autocorrelation function decays to a small fraction of its original value. The expression of autocorrelation function is given as

$$R(\tau) = \frac{1}{N} \sum_{i=1}^N z_i(x)z_i(x + \tau) \quad (6)$$

Similar to the local height, the autocorrelation function of the final surface is a sum of the autocorrelation functions of the two surfaces [40]:

$$R(\tau) = R_1(\tau) + R_2(\tau) \quad (7)$$

Here τ is the spatial separation, and R_1 and R_2 are the autocorrelation functions for surfaces S_1 and S_2 , respectively.

Many etched surfaces are widely assumed to follow an exponential autocorrelation function [35] given as,

$$R(\tau) = \sigma^2 \exp(-\tau/\beta) \quad (8)$$

in which σ is the standard deviation, m is the mean line, and β is the *ACL*. It is therefore reasonable to assume that R_2 is of this form.

For a 1D profile of the processed surface shown in figure 6, which is simplified as square pulses randomly scattered on a line with background roughness, each pulse can be considered as a random and independent event. The appearance of pulses on the profile resembles a random telegraph signal (*RTS*) [42], which is broadly used in characterization of noise and signals in semiconductor structures and devices [43-48]. Previous studies on surface autocorrelation length calculations [49] have utilized this treatment as well. Therefore we assume the number of pillars in the single profile follows the Poisson law, and the surface S_1 can be treated as an *RTS*. Consequently, the arrival rate λ of the pillars on a single profile is approximated as $\lambda = n/L$, in which n is the total number of pillars on the single profile, and L is the profile length. The autocorrelation function of S_1 can then be expressed as follows [42]:

$$R_1(\tau) = \sigma_1^2 \exp(-2\lambda\tau) \quad (9)$$

in which σ_l is the standard deviation of S_l .

Pillar coverage p in a single profile is a function of effective pulse width d_{eff} and number of pulses n ; $p = nd_{eff}/L$. Therefore the autocorrelation function of the final surface is given by

$$R(\tau) = \sigma_1^2 \exp\left(\frac{-2p\tau}{d_{eff}}\right) + \sigma_2^2 \exp\left(\frac{-\tau}{\beta_2^*}\right) \quad (10)$$

Autocorrelation length β^* of the final surface is defined as the distance at which value of the $R(\tau)$ drops to $1/e$ of the initial value [50]. The *ACL* of the final surface satisfies the relation:

$$\frac{2p}{d_{eff}} \beta^* = \ln \sigma_1^2 - \ln \left[\frac{\sigma_1^2 + \sigma_2^2}{e} - \sigma_2^2 \exp\left(\frac{-\beta^*}{\beta_1^*}\right) \right] \quad (11)$$

in which β^* is the *ACL* of the final surface, and β_1^* is the *ACL* of the background surface $S1$.

For S_2 , σ_2 is measured from the experimental data as 67.8 nm. For S_1 , the theoretical standard deviation $\sigma_1 = H/2$. d_{eff} for a given masking particle size was determined by fitting a Gaussian distribution to the PDF of the pillar widths from the AFM scans and obtaining a fitted mean. For the three sets of particle sizes, d_{eff} values were obtained as 0.89 μm , 1.28 μm and 2.77 μm respectively, corresponding to 45%-65% of the nominal size of the particles.

Figure 11 shows the experimental *ACL* of the surface roughness resulted from particles with 2.5-2.9 μm size, and its comparison to the theoretical prediction from equation 11. Uncertainties are also included based a 90% confidence level. *ACL* value of the quartz surface drops exponentially from 5.1 μm to 1 μm . Overall the experimental results follow the theoretical predictions reasonably well. At low coverage (5%-15%), the unevenly distributed particles and

the limited AFM scan scale tend to affect the accuracy of *ACL* measurement, resulting in significantly larger uncertainties.

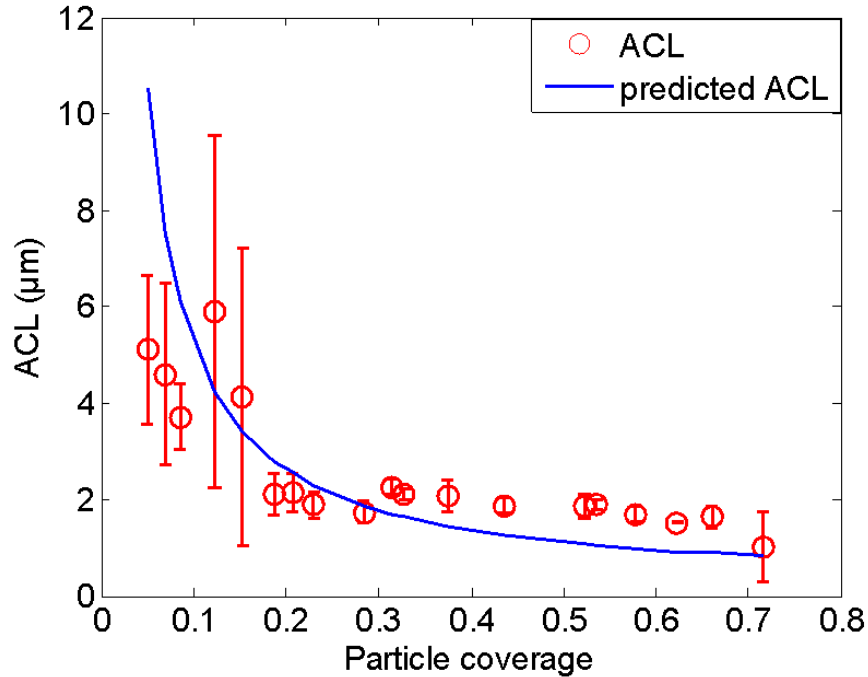


Figure 11. A comparison of the *ACL* values calculated from experiments and the values predicted by equation (10) for a particle diameter of $2.7 \mu\text{m}$ at various coverages.

Figure 12 shows the comparison of autocorrelation length between surfaces generated from different particle sizes. The *ACL* value of the final surfaces generated using the three particle diameters generally follows the same trend and decreases exponentially with coverage. In addition, the *ACL* at different coverages shows an approximately linear increase as particle diameter increases from $1.2 \mu\text{m}$ to $2.7 \mu\text{m}$ and $5.5 \mu\text{m}$. However, at low coverage, some deviation between the experimental result and the prediction was observed. The reason for the deviation is that the RTS model is based on the assumption that the pulses arrival follows a Poisson law, which means that the number of pulses needs to be large. However, at low coverage such as 5%,

the number of pillars on the surface is small, resulting in the mismatch between the model and the experimental results. The results from the model and the experiments agree quite well as coverage increases.

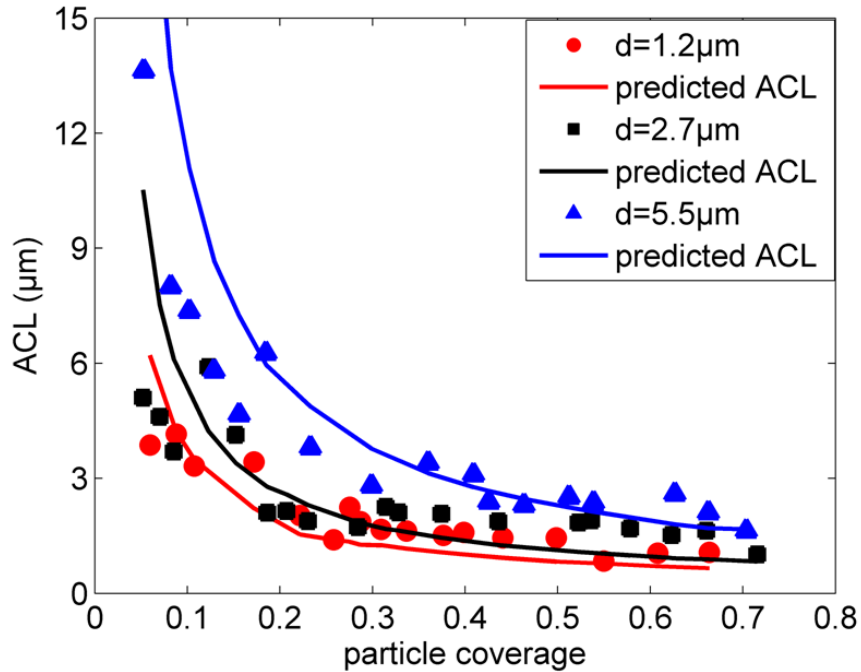


Figure 12. Variation of ACL as a function of coverage for different particle diameters. The figure shows a comparison of experimental data and theoretical predictions.

4.5 Conclusions

In this paper, a hybrid surface tailoring process was developed to impart nanoscale random roughness onto quartz substrates with desired amplitude and spatial roughness parameters. The process combines colloidal particle masking and reactive ion etching to generate and control random surface roughness over a range of average roughness (Ra) and

autocorrelation lengths (ACLs). The spatial randomness of the resulting surfaces was verified using a pair correlation function calculation. A mathematical model was developed to relate the process parameters to the resulting surface roughness parameters, which was further verified experimentally by AFM characterization.

Experimental result shows that through controlling process parameters, surface roughness of the processed substrates can be tailored at nanoscale on a random basis. By adjusting particle coverage and particle diameter, *ACL* of the final surface can be varied in the range of $0.9 \mu\text{m}$ to $14 \mu\text{m}$; while *Ra* can be tailored in the range of 50 nm to 190 nm by controlling particle coverage and etch depth. The study demonstrates that a potential exists to leverage and harness stochastic micro/nanoscale surface roughness in devices that use microchannels such as lab-on-a-chip for their respective applications.

4.6 Acknowledgments

The authors would like to thank Robert Mayer at Microelectronic Research Center in Iowa State University for the help of RIE system usage during this study, Dr. Baskar Ganapathysubramanian and Dr. Yufeng Wu for the discussion and help in the mathematical model in this paper.

4.7 References

1. Yang, D.Y. and Y. Liu, *Numerical simulation of electroosmotic flow in microchannels with sinusoidal roughness*. Colloids and Surfaces a-Physicochemical and Engineering Aspects, 2008. **328**(1-3): p. 28-33.
2. Prentner, S., et al., *Effects of Channel Surface Finish on Blood Flow in Microfluidic Devices*. Dtip 2009: Symposium on Design, Test, Integration and Packaging of MemS/Moems, 2009: p. 51-54
429.
3. Jaeger, R., et al., *Nanoscale surface roughness affects low Reynolds number flow: Experiments and modeling*. Applied Physics Letters, 2012. **101**(18).
4. Palasantzas, G. and A. Widom, *Roughness effects on the sliding frictional force of submonolayer liquid films on solid substrates*. Physical Review B, 1998. **57**(8): p. 4764-4767.
5. Kandlikar, S.G., et al., *Characterization of surface roughness effects on pressure drop in single-phase flow in minichannels*. Physics of Fluids, 2005. **17**(10).
6. Bahrami, M., M.M. Yovanovich, and J.R. Culham, *Pressure drop of fully developed, laminar flow in rough microtubes*. Journal of Fluids Engineering-Transactions of the Asme, 2006. **128**(3): p. 632-637.
7. Kandlikar, S.G., S. Joshi, and S.R. Tian, *Effect of surface roughness on heat transfer and fluid flow characteristics at low reynolds numbers in small diameter tubes*. Heat Transfer Engineering, 2003. **24**(3): p. 4-16.
8. Shen, S., et al., *Flow and heat transfer in microchannels with rough wall surface*. Energy Conversion and Management, 2006. **47**(11-12): p. 1311-1325.
9. Hao, P.F., et al., *Experimental investigation of water flow in smooth and rough silicon microchannels*. Journal of Micromechanics and Microengineering, 2006. **16**(7): p. 1397-1402.
10. Natrajan, V.K. and K.T. Christensen, *The impact of surface roughness on flow through a rectangular microchannel from the laminar to turbulent regimes*. Microfluidics and Nanofluidics, 2010. **9**(1): p. 95-121.
11. Komvopoulos, K., *Surface engineering and microtribology for microelectromechanical systems*. Wear, 1996. **200**(1-2): p. 305-327.
12. Rawool, A.S., S.K. Mitra, and S.G. Kandlikar, *Numerical simulation of flow through microchannels with designed roughness*. Microfluidics and Nanofluidics, 2006. **2**(3): p. 215-221.
13. Jeon, W. and C.B. Shin, *Design and simulation of passive mixing in microfluidic systems with geometric variations*. Chemical Engineering Journal, 2009. **152**(2-3): p. 575-582.

14. Koo, J.M. and C. Kleinstreuer, *Liquid flow in microchannels: experimental observations and computational analyses of microfluidics effects*. Journal of Micromechanics and Microengineering, 2003. **13**(5): p. 568-579.
15. Thomas, T.R., *Rough surfaces*. 1999: Imperial College Press.
16. Natrajan, V.K. and K.T. Christensen, *Non-intrusive measurements of convective heat transfer in smooth- and rough-wall microchannels: laminar flow*. Experiments in Fluids, 2010. **49**(5): p. 1021-1037.
17. Tambe, N.S. and B. Bhushan, *Scale dependence of micro/nano-friction and adhesion of MEMS/NEMS materials, coatings and lubricants*. Nanotechnology, 2004. **15**(11): p. 1561-1570.
18. Taylor, J.B., A.L. Carrano, and S.G. Kandlikar, *Characterization of the effect of surface roughness and texture on fluid flow - past, present, and future*. International Journal of Thermal Sciences, 2006. **45**(10): p. 962-968.
19. Ren, J., B. Ganapathysubramanian, and S. Sundararajan, *Experimental analysis of the surface roughness evolution of etched glass for micro/nanofluidic devices*. Journal of Micromechanics and Microengineering, 2011. **21**(2).
20. Farshad, F., H. Rieke, and J. Garber, *New developments in surface roughness measurements, characterization, and modeling fluid flow in pipe*. Journal of Petroleum Science and Engineering, 2001. **29**(2): p. 139-150.
21. Yeganeh, M.S., S.M. Dougal, and H.S. Pink, *Vibrational spectroscopy of water at liquid/solid interfaces: Crossing the isoelectric point of a solid surface*. Physical Review Letters, 1999. **83**(6): p. 1179-1182.
22. Lee, K., et al., *Uniformly dispersed deposition of colloidal nanoparticles and nanowires by boiling*. Applied Physics Letters, 2007. **91**(17).
23. Chen, X.H., et al., *Polymer pattern formation on SiO₂ surfaces using surface monolayer initiated polymerization*. Journal of Vacuum Science & Technology B, 2001. **19**(6): p. 2013-2019.
24. Narumi, T., et al., *Spatial and temporal dynamical heterogeneities approaching the binary colloidal glass transition*. Soft Matter, 2011. **7**(4): p. 1472-1482.
25. Kurita, R. and E.R. Weeks, *Experimental study of random-close-packed colloidal particles*. Physical Review E, 2010. **82**(1).
26. Pond, M.J., J.R. Errington, and T.M. Truskett, *Implications of the effective one-component analysis of pair correlations in colloidal fluids with polydispersity*. Journal of Chemical Physics, 2011. **135**(12).
27. Desmond, K.W. and E.R. Weeks, *Random close packing of disks and spheres in confined geometries*. Physical Review E, 2009. **80**(5).
28. Kurita, R., D.B. Ruffner, and E.R. Weeks, *Measuring the size of individual particles from three-dimensional imaging experiments*. Nature Communications, 2012. **3**.

29. Hansen, J.-P., and McDonald, I. R., ed. *Theory of Simple Liquids*. 2nd edition ed. 1986, Academic Press: London.
30. Le Doussal, P., Z. Ristivojevic, and K.J. Wiese, *Exact form of the exponential correlation function in the glassy super-rough phase*. *Physical Review B*, 2013. **87**(21).
31. Chernov, N., *Decay of correlations*. *Scholarpedia*, 2008. **3**(4):4862.
32. Ayer, A. and M. Stenlund, *Exponential decay of correlations for randomly chosen hyperbolic toral automorphisms*. *Chaos*, 2007. **17**(4).
33. Decarvalho, R., et al., *THE DECAY OF THE PAIR CORRELATION-FUNCTION IN SIMPLE FLUIDS - LONG-RANGED VERSUS SHORT-RANGED POTENTIALS*. *Journal of Physics-Condensed Matter*, 1994. **6**(44): p. 9275-9294.
34. Ganapathysubramanian, B. and N. Zabaras, *A seamless approach towards stochastic modeling: Sparse grid collocation and data driven input models*. *Finite Elements in Analysis and Design*, 2008. **44**(5): p. 298-320.
35. Bhushan, B., *Modern tribology handbook*. Vol. 1. 2001, Boca Raton: CRC.
36. Dekkers, H.F.W., et al., *Silicon surface texturing by reactive ion etching*. *Opto-Electronics Review*, 2000. **8**(4): p. 311-316.
37. Zaidi, S.H., D.S. Ruby, and J.M. Gee, *Characterization of random reactive ion etched-textured silicon solar cells*. *Ieee Transactions on Electron Devices*, 2001. **48**(6): p. 1200-1206.
38. Bhushan, B., *Modern tribology handbook*. 2001, Boca Raton: CRC.
39. Schmähling, J. and F.A. Hamprecht, *Generalizing the Abbott-Firestone curve by two new surface descriptors*. *Wear*, 2007. **262**(11-12): p. 1360-1371.
40. Bhushan, B., ed. *Modern tribology handbook*. Vol. 1. 2011, CRC: Boca Raton.
41. Zhang, Y.L. and S. Sundararajan, *The effect of autocorrelation length on the real area of contact and friction behavior of rough surfaces*. *Journal of Applied Physics*, 2005. **97**(10): p. 103526-1-103526-7.
42. Henry Stark, J.W.W., ed. *Probability and Random Processes with Applications to Signal Processing*. Third ed. 2002, Prentice-Hall: Upper Saddle River.
43. Efros, A.L. and M. Rosen, *Random telegraph signal in the photoluminescence intensity of a single quantum dot*. *Physical Review Letters*, 1997. **78**(6): p. 1110-1113.
44. Shi, Z.M., J.P. Mieville, and M. Dutoit, *Random Telegraph Signals in Deep-Submicron N-Mosfets*. *Ieee Transactions on Electron Devices*, 1994. **41**(7): p. 1161-1168.
45. Mueller, H.H. and M. Schulz, *Random telegraph signal: An atomic probe of the local current in field-effect transistors*. *Journal of Applied Physics*, 1998. **83**(3): p. 1734-1741.
46. Compagnoni, C.M., et al., *Statistical model for random telegraph noise in Flash memories*. *Ieee Transactions on Electron Devices*, 2008. **55**(1): p. 388-395.

47. Simoen, E. and C. Claeys, *Random Telegraph Signal: a local probe for single point defect studies in solid-state devices*. Materials Science and Engineering B-Solid State Materials for Advanced Technology, 2002. **91**: p. 136-143.
48. Ohata, A., et al., *Observation of Random Telegraph Signals - Anomalous Nature of Defects at the Si/SiO₂ Interface*. Journal of Applied Physics, 1990. **68**(1): p. 200-204.
49. Zhang, Y.L. and S. Sundararajan, *Method to generate surfaces with desired roughness parameters*. Langmuir, 2007. **23**(16): p. 8347-8351.
50. Whitehouse, D.J. and J.F. Archard, *The Properties of Random Surfaces of Significance in their Contact*. Proceedings of the Royal Society of London. Series A, Mathematical and Physical Sciences, 1970. **316**(1524): p. 97-121.

CHAPTER 5. INCORPORATING NANOSCALE RANDOM SURFACE ROUGHNESS BY DESIGN INTO MICROFLUIDIC DEVICE FABRICATION

A paper in preparation for submission to *Journal of Micromechanics and Microengineering*

Jing Ren¹ and Sriram Sundararajan¹

¹ *Department of Mechanical Engineering, Iowa State University, Ames, IA 50011, USA*

E-mail: srirams@iastate.edu

5.1 Abstract

As the size of modern microfluidic devices continue to shrink from millimeters to the level of 1-100 μm , the effect of nanoscale surface roughness on microfluidic flow becomes increasingly important. In this paper, we introduce a process that incorporates nanoscale random surface roughness into microfluidic device design and fabrication. Desired roughness was generated on glass substrate by chemical wet etching and characterized by 3D optical profilometer. The etching time was able to influence the RMS roughness and autocorrelation length of the surfaces. The processed glass substrate was then bonded to PDMS channels to form enclosed microfluidic devices. Micro Particle image velocimetry (microPIV) measurement was applied to test the effect of two different levels of roughness (relative roughness of 0.004% and 0.02%) on microfluidic flow under laminar condition. Deionized water was tested as a Newtonian fluid, while dilute xanthan gum solution with concentrations of 0.025% and 0.1% was used as non-Newtonian blood analog fluids. Autocorrelation analysis of the flow velocity in transverse direction reveals a noticeable effect of the nanoscale random surface roughness on the

three working fluids: a 4.9 fold increase in relative roughness causes measurable flow perturbation enhancement, which was quantified by an increase of 1.56%, 7.87% and 9% respectively in the average autocorrelation length, and an increase of 8.38%, 11.63% and 14.35% respectively in autocorrelation length at the center layers of the two devices.

5.2 INTRODUCTION

Realistic random roughness of channel surfaces is known to affect fluid flow behavior in microfluidic devices. This has relevance particularly for applications involving non-Newtonian fluids, such as biomedical lab-on-chip devices. Extensive studies during the past century indicate that surface roughness affects fluid flow behavior in microscale channels. Numerical simulations of micro flow in rough channels [1] showed that bulk flow velocity and the volumetric flow rate decrease in different rates as the roughness increases. Previous study on nanoscale roughness effect on laminar flow [2] indicated that increasing surface autocorrelation length has measurable impact on the transverse flow. Studies on the effect of surface roughness on friction force [3], pressure drop [4, 5], heat transfer in single-phase flow [6] and laminar-turbulent transition [7] indicated the necessity of precise control of the surface morphology inside the fluidic device for the purpose of enhancing the reliability and performance of the fluidic system [8].

In most of the current studies, surface was processed by micro-machining or micro-fabrication techniques and the roughness was formed by repeated shapes and patterns. Roughness formed by these processes is usually large and deterministic. It is well known that almost all mechanical or chemical processing inherently produces random roughness on realistic surfaces and consequently most engineering surfaces are random [9]. There are a few studies reported on the effect of random roughness on microfluids. Study reveals that increasing random

surface roughness enhances local Nusselt number in the thermally developing regime in laminar flow [10]. In addition, as surface roughness increases, earlier laminar-turbulent transition at lower Reynolds number was reported [11]. However, the impact of small scale random roughness on microfluidic flow behavior still remains relatively unexplored. Our recent study revealed that with low Reynolds number deionized water, nanoscale surface roughness (relative roughness less than 0.01%) causes flow perturbations that extend up to the center plane of a microfluidic channel of 50 μm in height [12]. This study provides insights in roughness harness for non-Newtonian fluids, which are frequently encountered in lab-on-chip and bioMEMS applications such as reagent mixing and single cell manipulation.

Effect of nanoscale random roughness will become increasingly important as microfluidic channels shrink in dimensions. Keeping this in mind, in this paper, we introduce a fabrication process which combines nanoscale random surface roughness tailoring and microfluidic channel fabrication. The devices were further applied to investigate the effect of nanoscale surface roughness on non-Newtonian blood analog fluid behavior in the laminar region using microParticle Image Velocimetry (microPIV) technique. Flow velocity was measured at the 9 layers in the microchannels. Autocorrelation length was computed to analyze the perturbation difference in transverse velocity.

5.3 Microchannel fabrication

In microfluidic chip fabrication, generating and controlling random surface roughness inside microfluidic channels becomes a challenging aspect due to the small size. Previous study on roughness tailoring on quartz [13] provide insights to application of microparticle masking and Reactive Ion Etching on roughness design in microfluidic chip fabrication. Experimental

study [14] shows that hydrofluoric etching is capable of generating roughness on glass substrate in a certain range: autocorrelation length increases in the range of 1 μm to 4 μm . In this study, we applied this method to our rapid fabrication process to obtain desired roughness in microfluidic channels. The effect on the nanoscale roughness on non-Newtonian blood analog fluid is also investigated.

Poly(dimethylsiloxane) (PDMS) is the most common materials used for microfluidic and lab-on-chip device fabrication [15-21]. PDMS presents high transparency, spontaneous adhesion and excellent biocompatibility [22]. In addition, it is easily to obtain submicron size structures with smooth surface condition by PDMS casting in rapid prototyping [23, 24]. Considering the application in non-Newtonian blood analog fluid and the transparency requirement of velocity field measurement using microPIV in this study, these attractive features of PDMS provide a preferable solution for microfluidic device fabrication.

Figure 1 shows the process flow of the rapid microfluidic device fabrication. SU-8 mold was fabricated by lithography on a glass wafer. PDMS replica containing the microfluidic channels was then obtained by casting PDMS onto the mold. A processed glass substrate with desired random roughness is bonded to the channel replica to enclose the channels.

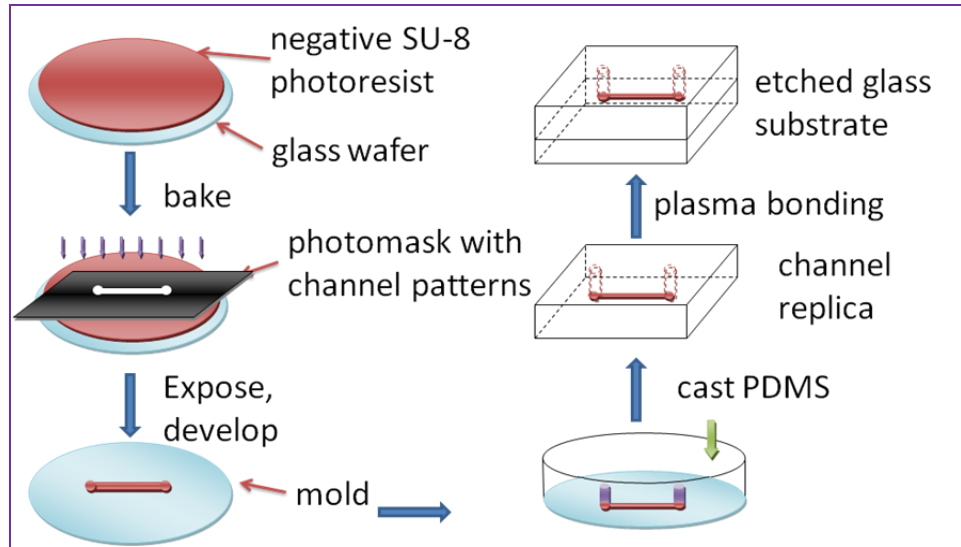


Figure 1. Processed flow of the microchannel fabrication

5.3.1 SU-8 mold fabrication

The SU-8 mold is a template for making the PDMS top-cover layer of the microfluidic channel. The microchannel structure was defined by photolithography on a glass wafer. Before coating, a 3 inch glass wafer was cleaned by a standard procedure and baked at 120 °C for 1 hour in oven to dehydrate. Then 3ml SU-8 negative photoresist (SU-8 2050, MicroChem Corp., Newton, MA) was spin coated on the wafer at a spin rate of 3000 rpm to achieve a 50um thickness. After coating, the wafer was soft baked on a hotplate for 10 minutes with temperature ramped to 65 °C. Then the temperature was ramped to 95 °C and kept for 130 minutes. The wafer was left on the hotplate until it cools down to room temperature. During the soft baking process, a glass beaker was used to cover the wafer to slow down the evaporation and prevent rugged surface of the SU-8 coating. Afterwards, the microchannel structure was transferred to the SU-8 by UV light exposure and post exposure baked at 55 °C for 2 hours. A glass beaker was still used during post exposure bake (PEB) to help obtaining higher quality SU-8 structures. The

wafer was later developed in a SU-8 developer (MicroChem Corp., Newton, MA) for 6 minutes and rinsed in isopropyl alcohol (IPA) for 10 seconds.

This process flow of SU-8 mold fabrication has three technical issues. The first issue is the SU-8 coating thickness, which is controlled through the spin rate, however needs to be adjusted several times to achieve a high accuracy. The second issue is the rugged surface of SU-8 observed after baking. Except using a glass beaker to cover the wafer during soft bake and post exposure bake, it also needs to mention that the hotplate should be ramped to the target temperature while baking and let cool to room temperature after baking. Another technical issue is that the thorough development of SU-8 is hard to achieve since the features are small (400 μm in width and 50 μm in height). Ultrasonic bath was used to help accelerate the dissolving of the photoresist.

5.3.2 PDMS casting and liquid inlet/outlet shaping

PDMS was prepared by mixing 1:10 ratio of curing agent and PDMS monomers (Sylgard 184, Dow Corning Corp.). The mixture was then degassed in a vacuum pump for 1 minute and placed still inside for 2 hours to expel remaining air bubbles inside. Afterwards, the PDMS was poured onto the SU-8 mold to replicate the channel structure. Regarding the creation of liquid inlet and outlet, several methods have been reported, including lithography, etching, ultrasonic machining, punching or drilling, and using o-rings while curing PDMS [25-29]. Punching or drilling method is fast and easy to operate, however cracks were usually observed in the near-hole area as the PDMS replica is thicker than 500 μm . Here we place two metal screws on the location of fluid inlet and outlet respectively while casting PDMS. After the PDMS is cured and peeled off from the SU-8 master, the two screws were carefully removed to form inlet and outlet

ports. The beaker container was baked in an oven at 60 °C for 8 hours. After curing, the PDMS replica was peeled off from the SU-8 mold carefully. SEM image in figure 2 shows the dimension of SU8 mold.

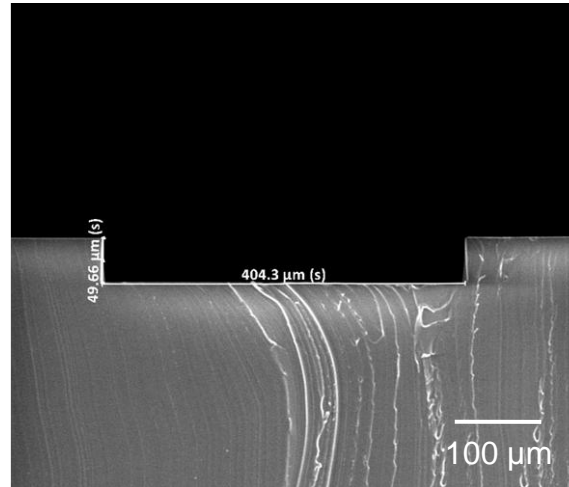


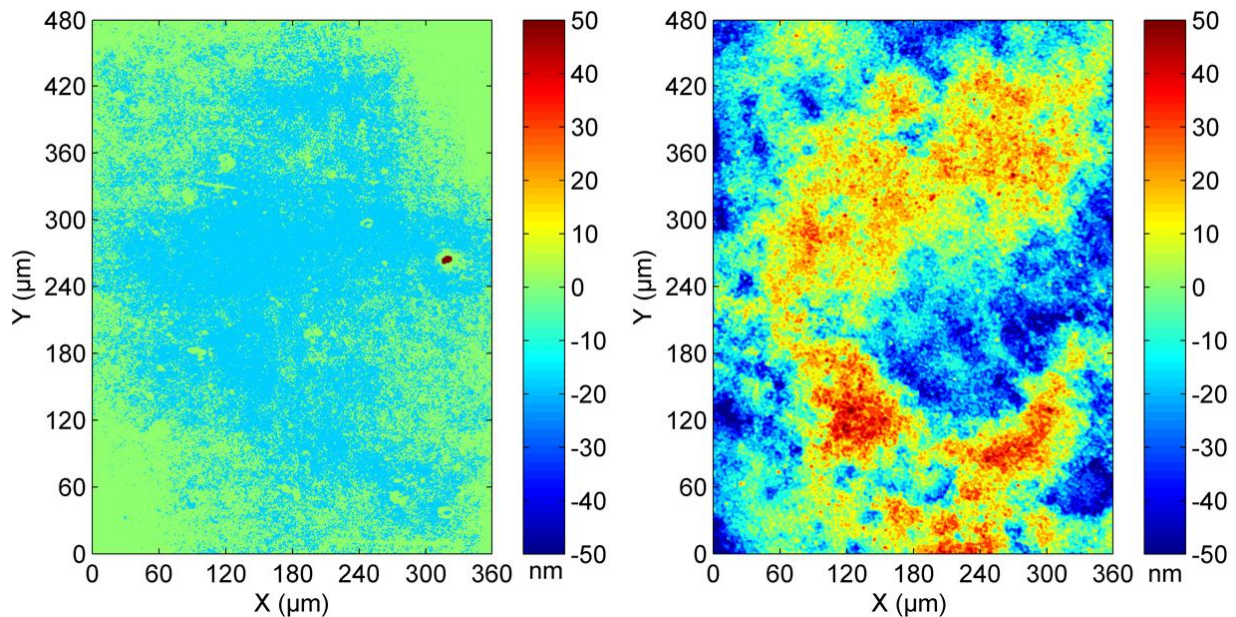
Figure 2. SEM image of the PDMS replica containing the microfluidic channel cross section

5.3.3 Preparation of glass substrate with nanoscale random surface roughness

The surface roughness examined in this study was generated on glass slides (25 mm × 75 mm, Erie Scientific Company, Portsmouth, NH). The glass samples were etched by buffered HF (6:1 volume ratio of 40% NH₄F in water to 49% HF in water) to generate different surface roughness. The etch rate was calibrated as 72 nm/min. Based on our previous experimental observation [14], etching times longer than 40 minutes results in significant surface damage on glass substrate, which significantly compromised the optical properties. Furthermore, the over-roughened surface will also lead to difficulty in bonding during microchannel fabrication. Since the device will be further used for microfluidic applications and measurements, the glass substrate etched by HF should still have favorable transparency. In our study, we use micro Particle Image Velocimetry (microPIV) to measure the velocity fields of close-wall area inside

the microfluidic chip, which requires superior channel transparency. Therefore, samples were etched for 30 minutes to obtain an amplitude roughness of 19.13 nm (Ra). After HF etching, the samples were rinsed in DI water for 5 minutes and dried by nitrogen. In addition, un-etched glass samples were also prepared for fabricating channels for comparison.

Surface topography of the processed glass substrate was obtained using a 3D Optical Surface Profiler (NewView™ 7100, Zygo Corporation, Middlefield, CT). The optical profilometer provided a scan area of $480 \mu\text{m} \times 360 \mu\text{m}$, with a lateral resolution of $0.73 \mu\text{m}$ and height resolution of 0.1 nm . As it is shown in figure 3, 30 minutes buffered HF etching significantly roughens the surface. The surface height data was exported into MATLAB to analyze surface roughness including amplitude (Ra) and spatial (ACL) roughness parameters. Here we report surface roughness as amplitude parameter Ra (center line average), spatial parameter ACL (autocorrelation length) [30] and relative roughness [31], which is defined as the roughness height to hydraulic diameter of the channel [1, 4, 32].



(b)

Figure 3. A schematic representing the scanned surface of each etching time: un-etched (left) and 30 min etched (right) surface: Ra=3.1 and 18.3 nm, respectively.

Surface roughness of the PDMS replica is also measured and listed in table 1. The Ra and ACL are respectively 2.44 nm and 0.69 μm , which are comparable to the roughness of un-etched glass substrate. As a result of wet etching, relative roughness of the glass wall of the microchannel increases from 0.004% to 0.02%

Table 1. Comparison of surface roughness of processed glass and PDMS

Roughness	Surface type		
	Un-etched glass	30-minute-etched glass	PDMS
Ra (nm)	3.28	19.13	2.44
ACL (μm)	1.33	2.34	0.69
Relative roughness	0.00%	0.02%	0.00%

5.3.4 Microfluidic channel bonding, inspection and testing

Following the PDMS replica fabrication from the SU-8 mold and glass substrate processing with tailored surface roughness, bonding method needs to be developed to enclose the two parts and form a sealed microfluidic device. Common methods of bonding polymer substrates and films to glass include use of adhesives [33], UV curable glues [34, 35], lamination [27, 36] and temperature annealing [37]. Surface plasma oxidization has also been reported as an effective bonding method for a number of materials including PDMS, polyethylene, polystyrene, silicon, glass and quartz [38-41]. The oxygen plasma treatment helps to activate the surface of PDMS by introducing silanol groups of Si-OH. These polar groups condense with OH and COOH groups on another surface and form bonds while they are brought into contact [42-44]. In our process, the PDMS replica with the microfluidic channel features was bonded to the etched

glass substrate after plasma treatment. Oxygen plasma was provided by a plasma cleaner system (PDC-32G, Harrick Plasma, Ithaca, NY). Both the PDMS replica and the glass substrate were placed into the chamber and treated with medium-level oxygen plasma for 55 seconds. The surface-activated PDMS and glass were then taken out of the plasma chamber and brought into contact. The two parts seals quickly and form a very hard-to-break bond as appropriate pressure applied.

Tubing was attached to the fluid inlet and outlet, which is shown in Figure 4. Sealing performance of the devices was tested by pumping deionized water with tracing particles (nile red FluoSpheres, Invitrogen Corporation) through and the sealing performance was proved satisfying.

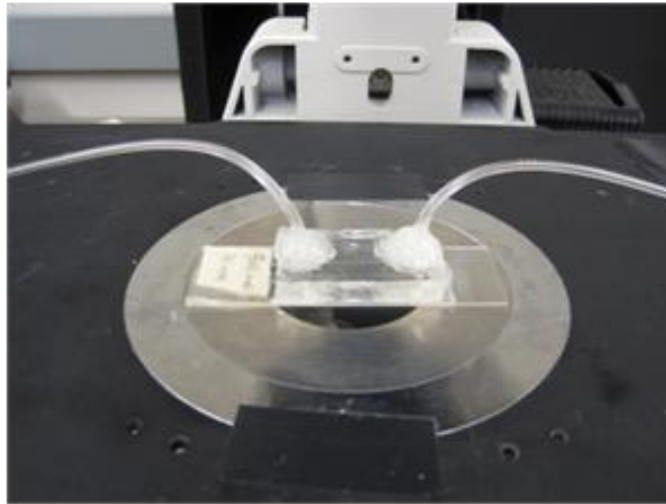


Figure 4. Final device with the tailored wall roughness

The sealing performance of the microfluidic device was test by a micro Particle Image Velocimetry (μ PIV) system to investigate the roughness impact on microflow behavior.

5.4. Effect of the nanoscale surface roughness on Non-Newtonian blood analog fluidic flow

5.4.1 Blood analog fluid

The shear thinning and viscoelastic behavior of blood are resulted from the red blood cells. The erythrocyte concentration, aggregation and deformation plays an important role in the rheological characteristics of the human blood [45]. Blood analog fluids need be meet the shearing thinning and viscoelastic behavior as non-Newtonian fluids.

In most of the current blood analog, non-Newtonian fluids measurement study, dilute xanthan gum is widely used due to its weak-gel shear-thinning property. In addition, xanthan gum is soluble in water, providing high viscosity at very low concentrations [46-50]. Good pseudoplasticity allows the solution to be poured and pumped easily [50, 51]. These properties of xanthan gum solution make it an ideal analog fluid for rheology study of non-Newtonian fluids. Bandulasena et al. reported a use of low concentration xanthan gum to study the shear-thinning behavior of power law non-Newtonian fluids [52]. Weight concentrations of 0.005%, 0.01% and 0.025% were used in the study. The velocity fields of the dilute xanthan gum solution in a microchannel were measured by microPIV. Compared to the CFD simulation, the measurement error was less than 5%. This study provides insights of using microPIV equipment in non-Newtonian fluid flow measurement. Gijsen et al. [53] used KSCN-X, mixed concentrated potassium thiocyanate in water (71% in weight) with addition of 250 ppm Xanthan gum. The KSCN solution was used as a Newtonian control fluid which has good transparency for Laser Doppler Anemometry measurement. And the added xanthan gum solution provide the shear thinning and viscoelastic behavior as non-Newtonian fluid. Wickramasinghe et al. [54] used a

very dilute xanthan gum (0.0075%-0.04%) added into deionized water/glycerol or deionized water solution as a blood analog fluid. A power law model was used in the simulation to predict the rheological behavior.

In this study, very dilute xanthan gum solution was used as a blood analog fluid. Two weight concentrations of 0.025% and 0.1% were used. The xanthan gum powder was diluted in deionized water with pH value of 7. The low conductivity of the deionized water helps reduce the agglomeration of the seeding particles [55], which is extremely helpful in this study since the bottom rough wall tends to trap particles and form agglomeration. In addition, the same deionized water was also tested as a working fluid for comparison as a Newtonian fluid.

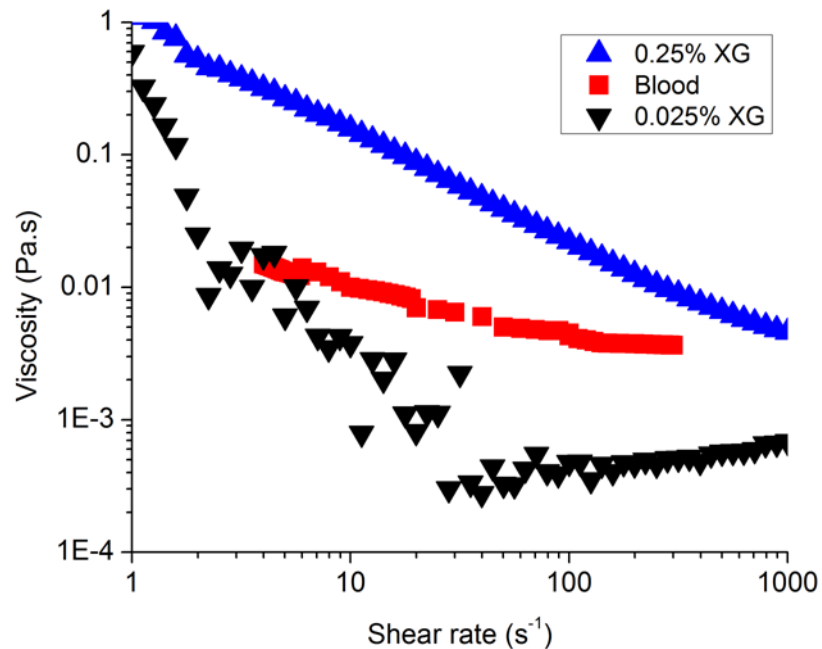


Figure 5. Steady shear properties of the dilute xanthan gum solution, compared to the property of blood. The blood data was taken from Shin (2002) [56].

Viscosity of blood is in a relative wide range (0.001-0.1) based on hematocrit difference and varies among donors [56]. The data in figure 5 shows the viscosity of blood lies between xanthan gum solution with concentrations of 0.025% and 0.25%. In this study, xanthan gum solution with 0.025% and 0.1% concentration, which is considered as reasonable blood-analogue fluid, was used for the microPIV measurement.

5.4.2 Micro-PIV measurement

A schematic of microPIV system is shown in figure 6. Illumination of the micro-channel was provided by a double-pulsed Nd:YAG Continuum Minilite laser. The working fluids were seeded with 1 μ m diameter fluorescent Nile red flow-tracing particles (Nile red FluoSpheres, Invitrogen Corporation). The weight concentration of the particle solution is 0.02% to provide a sufficient particle density for flow velocity tracking [57]. Flow images were captured by a LaVision Imager Intense CCD camera. In this study, a 40 \times 0.6 NA objective was coupled with a 0.45 \times coupler, resulting in a total magnification of 18 \times and a depth of correlation of 7.8 μ m [58]. Interrogation windows of 32 \times 32 pixels were chosen. The overlapped area of adjacent interrogation windows is 50%. Delay time of the double-pulsed laser was adjusted at each depth so that the tracing particles move approximately $\frac{1}{4}$ of the interrogation window between the two exposures. 500 microPIV images were acquired at each location and analyzed using the sum of correlation algorithm. Velocity fields were measured at 9 height levels inside the rectangular channel with 5 μ m increment between. Three experimental sets were repeated on each channel. Flow rate of 0.1 ml/min was used in this study.

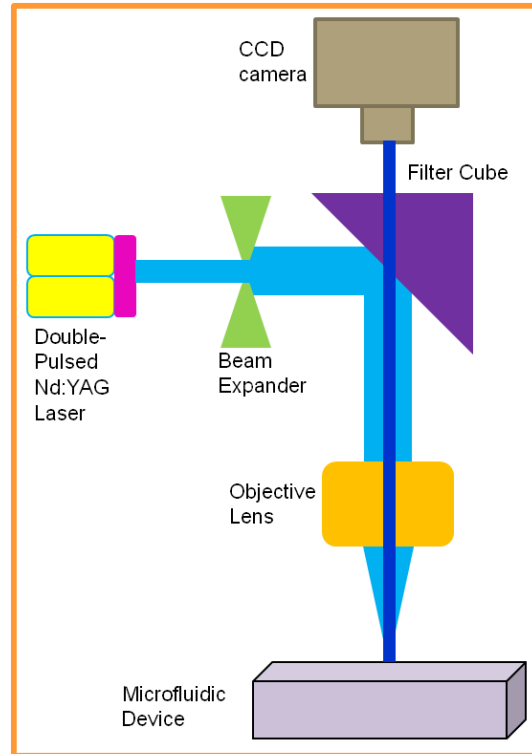


Figure 6. Micro-PIV apparatus and methodology

Velocity fields were computed from the image sets using sum of correlation algorithm. Streamwise and transverse velocities were exported from the velocity field and processed in Matlab. Plane fit was applied to the data to remove the plane resulted un-horizontal effect of the microPIV work station. As the surface roughness parameters of the bottom and top walls of the tested two microchannels are listed in the table 1, notice the relative roughness is very small (from 0.004% to 0.02%), To our knowledge, it is the first attempt to directly measure and quantify the effect of surface roughness on the velocity field at this very small scale.

The effect of surface roughness was investigated by focusing on the velocity perturbations caused by the roughness itself. In this study, autocorrelation analysis was used in order to characterize the flow perturbations. The autocorrelation function, $C(\tau)$ was estimated for a

velocity field in a plane to find β^* , the autocorrelation length. The autocorrelation length is defined as the lag distance where the autocorrelation function decays to $1/e$. Autocorrelation analysis was performed on velocity fields in the xy-plane. The autocorrelation length is calculated using the velocity field obtained from microPIV measurement. The interrogation region was taken toward the center area of the channel away from the side-walls and liquid inlet/outlet to eliminate the side-wall boundary layer and boundary condition effects. In order to simplify the description, here we will call the microfluidic device with un-etched glass wall as device 1, and the one with 30-minute-etched glass wall as device 2. There is a 4.9 fold increase of the relative roughness on the glass walls between the two devices.

Figure 7 shows the variation of autocorrelation length in transverse velocity between the two devices: through the bottom to the top of two devices, the ACL values of V_x are comparable, while the rougher device has slightly higher ACL than the smoother device (average increase of 1.56%). An 8.4% increase of ACL is observed at the center layer of the microchannels, which is the 25 μm height position. This is close to our previous study [12] combined microPIV measurement and DNS simulation, which shows a 11.8% increase between two microfluidic devices with the same experimental parameters but slightly different channel shapes as in this study.

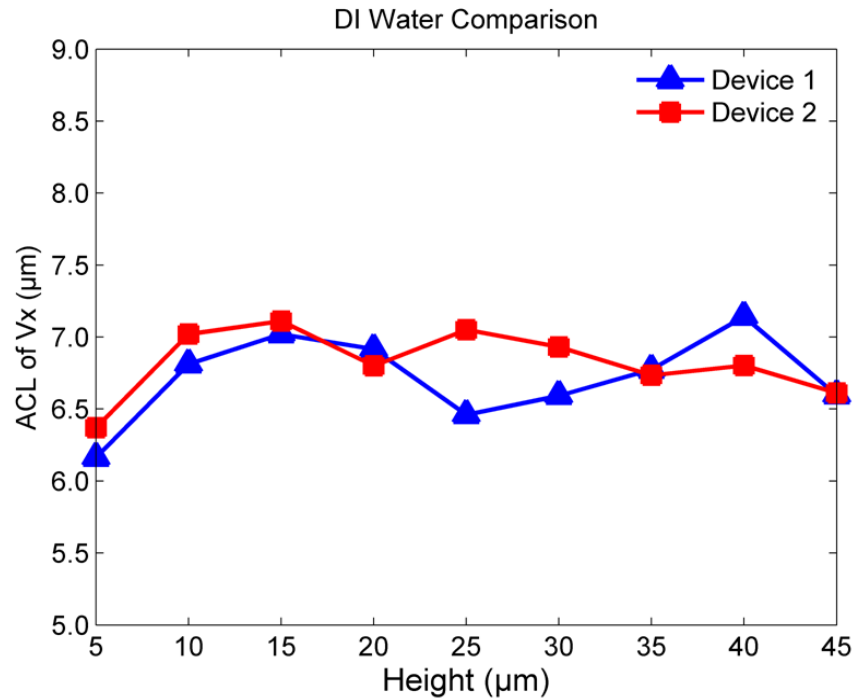


Figure 7. Autocorrelation length comparison between the two devices using deionized water as working fluid.

Regarding the non-Newtonian blood analog fluid, the relative roughness increase between the two devices further differs the autocorrelation length of transverse velocity. As it is shown in Figure 8, a general increase of 7.87% in ACL of V_x was observed from device 1 to device 2. This indicates that the effect of roughness differences on the flow perturbation increases as the working fluid switch to 0.025% xanthan gum solution from deionized water.

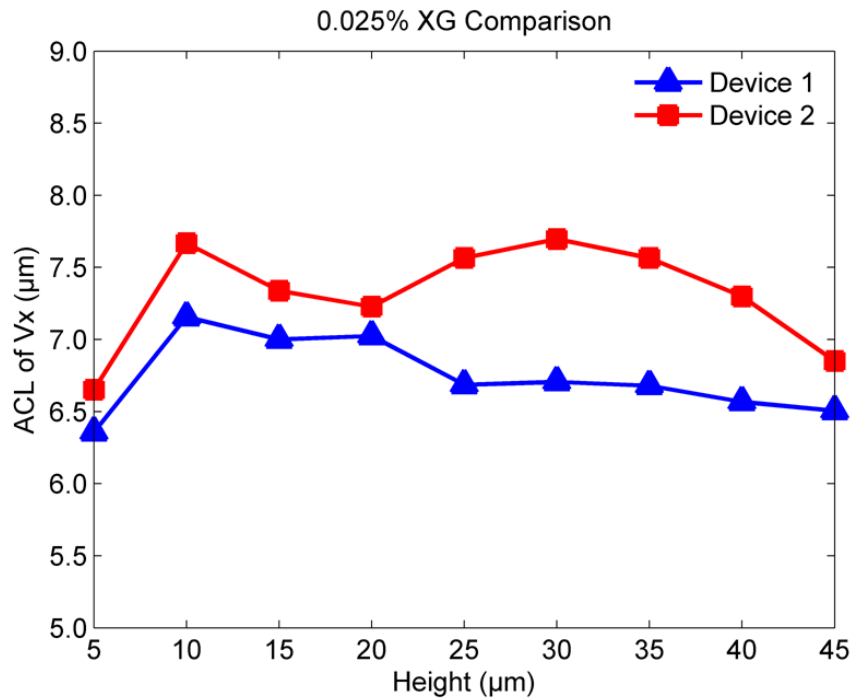


Figure 8. Autocorrelation length comparison between the two devices using 0.025% xanthan gum solution as working fluid.

The comparison of ACL in V_x between the two devices using 0.1% xanthan gum solution is shown in figure 9. Similar to figure 8, the autocorrelation length curve also has an obvious shift-up from device 1 to device 2. Quantitatively, compared to the 1.56% and 7.87% in figure 7 and figure 8, this shift increases to 9% in figure 9, indicating a larger flow perturbation caused by the roughness differences.

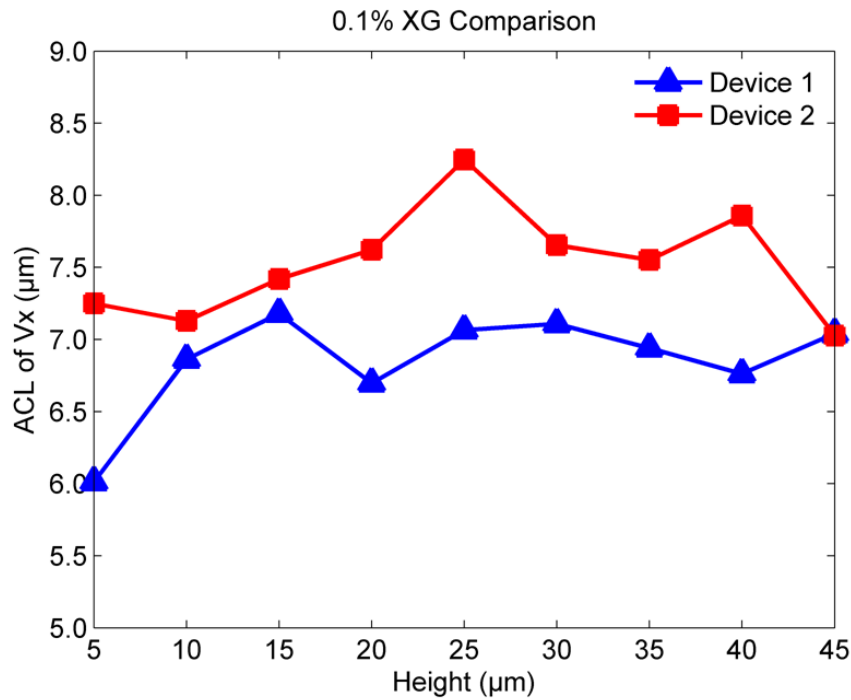


Figure 9. Autocorrelation length comparison between the two devices using 0.1% xanthan gum solution as working fluid.

A plausible explanation for this observation is that originating at the bottom glass wall, higher relative roughness causes larger velocity plums. The plum structures erupt up to the center layer of the channel and the autocorrelation length achieves a maximum. The size of plum structure grows larger as the height increases in the rougher channel. As the measurement height keep increasing to the top wall (PDMS cover), the flow plum structure caused by surface roughness on this wall shrinks accordingly, which is reflected by the slight decrease in autocorrelation length of V_x . The detailed mechanism of the flow structure above the center layer will be investigated in our further study.

5.5 Conclusions

A rapid fabrication process of incorporating nanoscale random surface roughness by design into microfluidic device and its impact on non-Newtonian blood analog fluid was introduced in this study. Two microfluidic channels with different levels of wall roughness were fabricated. Channel dimension is 25mm (L) $400\ \mu\text{m}$ (W) \times $50\ \mu\text{m}$ (H). Relative roughness was characterized by a 3D optical profilometer and estimated as 0.004% and 0.02%, respectively. The devices were successfully applied to analyze the impact of nanoscale random surface roughness on Newtonian and non-Newtonian flow in the laminar flow region using microPIV technique. Three different working fluids were investigated in this study: deionized water as a Newtonian fluid, 0.025% and 0.1% xanthan gum solution as non-Newtonian blood analog fluid. Flow rate of 0.1ml/min was used in the microPIV measurement.

Autocorrelation analysis of the flow velocity in transverse direction was applied to investigate the effect of roughness differences on flow perturbation of the three working fluids. Results were compared between the two devices with the three kinds of working fluids respectively. It is shown that an order increase of relative roughness between the two devices leads to a noticeable increase of the autocorrelation length in transverse velocity: the average increases of 1.56%, 7.87% and 9% in ACL of V_x are observed when using deionized water, 0.025% and 0.1% xanthan gum solution, respectively. This indicates a quantifiable flow perturbation increase between the two devices caused by the different levels of nanoscale random surface roughness.

This impact starts at the bottom of the microfluidic channels, where the channel wall was processed for desired roughness levels, and accumulates up to the center layer of the channels.

At 25 μm height position, the three working fluids are showing 8.38%, 11.63% and 14.35% increase of ACL in transverse velocity from device 1 to device 2, respectively. Above the center layer, the accumulation trend slows down and the ACL of V_x starts to decrease as the measurement layer moving up to the top wall (PDMS cover). One thing need to be point out is that, this decrease is also more obvious in device 2 among the three working fluids.

This study experimentally proves that nanoscale surface roughness affects microfluidic flow in the laminar region and this effect can be realized through the rapid fabrication process and further captured by microPIV technique. By design nanoscale random roughness tailoring into microfluidic channel fabrication, this process provides a fast, low-cost and reliable solution for future studies on microfluidic applications such as droplet control, cell sorting, molecular manipulation and chemical detection, etc., through nanoscale surface tailoring technique.

5.6 References

1. Yang, D.Y. and Y. Liu, *Numerical simulation of electroosmotic flow in microchannels with sinusoidal roughness*. Colloids and Surfaces a-Physicochemical and Engineering Aspects, 2008. **328**(1-3): p. 28-33.
2. R. Jaeger, J.R., Y. Xie, M. Olsen, S. Sundararajan, B. Ganapathysubramanian, *Investigating the effect of nanoscale surface roughness on microfluidic flow: experiment, theory and modeling*. in preparation.
3. Palasantzas, G. and A. Widom, *Roughness effects on the sliding frictional force of submonolayer liquid films on solid substrates*. Physical Review B, 1998. **57**(8): p. 4764-4767.
4. Kandlikar, S.G., et al., *Characterization of surface roughness effects on pressure drop in single-phase flow in minichannels*. Physics of Fluids, 2005. **17**(10).

5. Bahrami, M., M.M. Yovanovich, and J.R. Culham, *Pressure drop of fully developed, laminar flow in rough microtubes*. Journal of Fluids Engineering-Transactions of the Asme, 2006. **128**(3): p. 632-637.
6. Kandlikar, S.G., S. Joshi, and S.R. Tian, *Effect of surface roughness on heat transfer and fluid flow characteristics at low reynolds numbers in small diameter tubes*. Heat Transfer Engineering, 2003. **24**(3): p. 4-16.
7. Hao, P.F., et al., *Experimental investigation of water flow in smooth and rough silicon microchannels*. Journal of Micromechanics and Microengineering, 2006. **16**(7): p. 1397-1402.
8. Komvopoulos, K., *Surface engineering and microtribology for microelectromechanical systems*. Wear, 1996. **200**(1-2): p. 305-327.
9. Thomas, T.R., *Rough surfaces*. 1999: Imperial College Press.
10. Natrajan, V.K. and K.T. Christensen, *Non-intrusive measurements of convective heat transfer in smooth- and rough-wall microchannels: laminar flow*. Experiments in Fluids, 2010. **49**(5): p. 1021-1037.
11. Natrajan, V.K. and K.T. Christensen, *The impact of surface roughness on flow through a rectangular microchannel from the laminar to turbulent regimes*. Microfluidics and Nanofluidics, 2010. **9**(1): p. 95-121.
12. Jaeger, R., et al., *Nanoscale surface roughness affects low Reynolds number flow: Experiments and modeling*. Applied Physics Letters, 2012. **101**(18).
13. Ren, J., et al., *A HYBRID SURFACE TAILORING PROCESS TO GENERATE ROUGHNESS AON QUARTZ*. Under review, 2013.
14. Ren, J., B. Ganapathysubramanian, and S. Sundararajan, *Experimental analysis of the surface roughness evolution of etched glass for micro/nanofluidic devices*. Journal of Micromechanics and Microengineering, 2011. **21**(2).
15. Chao, S.H., R. Carlson, and D.R. Meldrum, *Rapid fabrication of microchannels using microscale plasma activated templating (mu PLAT) generated water molds*. Lab on a Chip, 2007. **7**(5): p. 641-643.
16. Patel, J.N., et al., *PDMS as a sacrificial substrate for SU-8-based biomedical and microfluidic applications*. Journal of Micromechanics and Microengineering, 2008. **18**(9).
17. Becker, H. and L.E. Locascio, *Polymer microfluidic devices*. Talanta, 2002. **56**(2): p. 267-287.
18. Zhang, X.L. and S.J. Haswell, *Materials matter in microfluidic devices*. Mrs Bulletin, 2006. **31**(2): p. 95-99.
19. Kim, M.S., et al., *Fabrication of microchip electrophoresis devices and effects of channel surface properties on separation efficiency*. Sensors and Actuators B-Chemical, 2005. **107**(2): p. 818-824.

20. Fiorini, G.S. and D.T. Chiu, *Disposable microfluidic devices: fabrication, function, and application*. Biotechniques, 2005. **38**(3): p. 429-446.
21. Chow, W.W.Y., et al., *Microfluidic channel fabrication by PDMS-interface bonding*. Smart Materials & Structures, 2006. **15**(1): p. S112-S116.
22. Peterson, S.L., et al., *Poly(dimethylsiloxane) thin films as biocompatible coatings for microfluidic devices: Cell culture and flow studies with glial cells*. Journal of Biomedical Materials Research Part A, 2005. **72A**(1): p. 10-18.
23. Xia, Y.N. and G.M. Whitesides, *Soft lithography*. Annual Review of Materials Science, 1998. **28**: p. 153-184.
24. Sun, X.H., et al., *Rapid prototyping of poly(methyl methacrylate) microfluidic systems using solvent imprinting and bonding*. Journal of Chromatography A, 2007. **1162**(2): p. 162-166.
25. Ichiki, T., Y. Sugiyama, and Y. Horiike, *Miniaturized capillary electrophoresis fabricated on pyrex glass chips using deep dry etching and anodic bonding*. Journal of Photopolymer Science and Technology, 2002. **15**(2): p. 311-316.
26. Arakawa, T., et al., *Pinhole-free pyrex glass etching using HF-H₂SO₄ mixed acid and its applications for a PDMS microflow system*. Transducers '05, Digest of Technical Papers, Vols 1 and 2, 2005: p. 1489-1492.
27. Yamada, H., et al., *Fabrication of gravity-driven microfluidic device*. Review of Scientific Instruments, 2008. **79**(12).
28. Abgrall, P., et al., *A novel fabrication method of flexible and monolithic 3D microfluidic structures using lamination of SU-8 films*. Journal of Micromechanics and Microengineering, 2006. **16**(1): p. 113-121.
29. Liu, J.S., et al., *Electrostatic bonding of a silicon master to a glass wafer for plastic microchannel fabrication*. Journal of Materials Processing Technology, 2006. **178**(1-3): p. 278-282.
30. Bhushan, B., ed. *Modern tribology handbook*. Vol. 1. 2001, CRC: Boca Raton.
31. Moody, L.F., *Friction factors for pipe flow*. Transactions of the ASME, 1944. **66**(8): p. 671-684.
32. Rawool, A.S., S.K. Mitra, and S.G. Kandlikar, *Numerical simulation of flow through microchannels with designed roughness*. Microfluidics and Nanofluidics, 2006. **2**(3): p. 215-221.
33. McDonald, J.C., et al., *Fabrication of microfluidic systems in poly(dimethylsiloxane)*. Electrophoresis, 2000. **21**(1): p. 27-40.
34. Schlautmann, S., et al., *Fabrication of a microfluidic chip by UV bonding at room temperature for integration of temperature-sensitive layers*. Journal of Micromechanics and Microengineering, 2003. **13**(4): p. S81-S84.

35. Hartmann, D.M., et al., *A low-cost, manufacturable method for fabricating capillary and optical fiber interconnects for microfluidic devices*. Lab on a Chip, 2008. **8**(4): p. 609-616.
36. Rossier, J.S., et al., *Topography, crystallinity and wettability of photoablated PET surfaces*. Langmuir, 1999. **15**(15): p. 5173-5178.
37. Kricka, L.J., et al., *Fabrication of plastic microchips by hot embossing*. Lab on a Chip, 2002. **2**(1): p. 1-4.
38. Liston, E.M., L. Martinu, and M.R. Wertheimer, *Plasma Surface Modification of Polymers for Improved Adhesion - a Critical-Review*. Journal of Adhesion Science and Technology, 1993. **7**(10): p. 1091-1127.
39. Bhattacharya, S., et al., *Studies on surface wettability of poly(dimethyl) siloxane (PDMS) and glass under oxygen-plasma treatment and correlation with bond strength*. Journal of Microelectromechanical Systems, 2005. **14**(3): p. 590-597.
40. Belford, R.E. and S. Sood, *Surface activation using remote plasma for silicon to quartz wafer bonding*. Microsystem Technologies-Micro-and Nanosystems-Information Storage and Processing Systems, 2009. **15**(3): p. 407-412.
41. Hall, J.R., et al., *Activated Gas Plasma Surface Treatment of Polymers for Adhesive Bonding*. Journal of Applied Polymer Science, 1969. **13**(10): p. 2085-&.
42. Chaudhury, M.K. and G.M. Whitesides, *Direct Measurement of Interfacial Interactions between Semispherical Lenses and Flat Sheets of Poly(Dimethylsiloxane) and Their Chemical Derivatives*. Langmuir, 1991. **7**(5): p. 1013-1025.
43. Chaudhury, M.K. and G.M. Whitesides, *Correlation between Surface Free-Energy and Surface Constitution*. Science, 1992. **255**(5049): p. 1230-1232.
44. Morra, M., et al., *On the Aging of Oxygen Plasma-Treated Polydimethylsiloxane Surfaces*. Journal of Colloid and Interface Science, 1990. **137**(1): p. 11-24.
45. Chien, S., et al., *Shear-Dependent Deformation of Erythrocytes in Rheology of Human Blood*. American Journal of Physiology, 1970. **219**(1): p. 136-&.
46. Schorsch, C., C. Garnier, and J.L. Doublier, *Viscoelastic properties of xanthan/galactomannan mixtures: comparison of guar gum with locust bean gum*. Carbohydrate Polymers, 1997. **34**(3): p. 165-175.
47. Kim, C. and B. Yoo, *Rheological properties of rice starch-xanthan gum mixtures*. Journal of Food Engineering, 2006. **75**(1): p. 120-128.
48. Whitcomb, P.J. and C.W. Macosko, *Rheology of Xanthan Gum*. Journal of Rheology, 1978. **22**(5): p. 493-505.
49. Milas, M., et al., *Flow and Viscoelastic Properties of Xanthan Gum Solutions*. Macromolecules, 1990. **23**(9): p. 2506-2511.

50. Casas, J.A., A.F. Mohedano, and F. Garcia-Ochoa, *Viscosity of guar gum and xanthan/guar gum mixture solutions*. Journal of the Science of Food and Agriculture, 2000. **80**(12): p. 1722-1727.
51. Sikora, M., et al., *Rheological and sensory properties of dessert sauces thickened by starch-xanthan gum combinations*. Journal of Food Engineering, 2007. **79**(4): p. 1144-1151.
52. Bandulasena, H.C.H., W.B. Zimmerman, and J.M. Rees, *An inverse method for rheometry of power-law fluids*. Measurement Science & Technology, 2011. **22**(12).
53. Gijssen, F.J.H., F.N. van de Vosse, and J.D. Janssen, *The influence of the non-Newtonian properties of blood on the flow in large arteries: steady flow in a carotid bifurcation model*. Journal of Biomechanics, 1999. **32**(6): p. 601-608.
54. Wickramasinghe, S.R., C.M. Kahr, and B.B. Han, *Mass transfer in blood Oxygenators using blood analogue fluids*. Biotechnology Progress, 2002. **18**(4): p. 867-873.
55. Liu, Y., M.G. Olsen, and R.O. Fox, *Turbulence in a microscale planar confined impinging-jets reactor*. Lab on a Chip, 2009. **9**(8): p. 1110-1118.
56. Shin, S. and D.Y. Keum, *Measurement of blood viscosity using mass-detecting sensor*. Biosensors & Bioelectronics, 2002. **17**(5): p. 383-388.

CHAPTER 6. NANOSCALE SURFACE ROUGHNESS AFFECTS LOW REYNOLDS NUMBER FLOW: EXPERIMENTS AND MODELING

A paper in preparation R. Jaeger[#], J. Ren[#], Y. Xie[#], S. Sundararajan, M. G. Olsen, B.

Ganapathysubramanian¹

Jing Ren¹ and Sriram Sundararajan¹

¹ *Department of Mechanical Engineering, Iowa State University, Ames, IA 50011, USA*

#These authors contributed equally to this work

E-mail: baskarg@iastate.edu

6.1 Abstract

Most micro-channel fabrication strategies generate nano-to-micro-scale, stochastic surface roughness. This inherent stochasticity can potentially be harnessed to direct microfluidic operations such as self-cleaning behavior and localized mixing. This work investigates the effect of stochastic nanoscale roughness on low to moderate Reynolds number Newtonian flow using concurrent modeling and experiments. We fabricate a microscopic channel with tailored hydrofluoric-acid-etched rough surfaces. Optical profilometry and micro-particle-image-velocimetry are used to characterize the surface roughness and flow field, and is integrated with Direct Numerical Simulation that resolves effects of nanoscale roughness. Results indicate that

nanoscale roughness causes flow perturbations that extend up to the mid-plane and is insensitive to flow-rates.

6.2 Introduction

Soft lithography using SU-8 photoresist and poly(dimethylsiloxane) (PDMS) is a commonly used technique to fabricate microchannels. This method in conjunction with hydrofluoric acid (HF) etching is an effective rapid prototype microfabrication process of microchannels [1, 2, 3]. A byproduct of such fabrication is an inherent, stochastic surface roughness [4]. The surface roughness can exhibit variations in root-mean-squared roughness from microns to nanometers. Interestingly, surface roughness at these scales has been shown to lead to hydrophobicity, which can result in self-cleaning surfaces [35], which is especially useful for biological analysis and separation, biomedical testing and nano-manufacturing applications [36]. Furthermore, stochastic roughness (or texturing) in micro-channels can be harnessed for multi-functional properties like anti-reflectivity and optical transparency [33]. Recent work has shown that this roughness can be ‘tailored’ by tuning the fabrication process [4, 34] and open up promising avenues to enhance microfluidic applications. These promising developments necessitate a thorough understanding of the flow characteristics of fluids in rough microchannels and have been the focus of recent studies [5,6,7].

The effect of *micro-scale surface roughness* ($\gamma = 1.6\%$, where $\gamma = 100\% * \text{roughness height} / D_H$, and D_H is the hydraulic diameter of the channel) was examined [8] experimentally by using micro-PIV and comparing with a *smooth* computational fluid dynamics (CFD) simulation of a channel of the same geometry. Flow effects in relation to *periodic micro-scale obstructions* in height have also been investigated using CFD

by various authors [9, 10, 11]. These analyses usually focus on periodic roughness and are invariably limited to 2D [12, 13, 15, 16]. In one study, Valdes et. al [14] used pyramidal shapes in a 3-dimensional domain that were randomly placed throughout the channel surface in accordance to data acquired from an actual surface. *However, the CFD surface did not mimic the actual surface exactly.* Instead, relative roughness and peak density values were acquired from the actual surface to generate the CFD surface. As a result, the true effect of a tangible surface was not investigated. Recently, Liu et.al [12] analyzed three-dimensional surface roughness using molecular dynamics in nanochannels with $\gamma=3\%$, and found that random roughness had a greater effect on flow than periodic obstructions. While molecular dynamics simulations are exceedingly useful in gaining insight into the mechanics involved, they are limited to very small domains and time-scales due to their prohibitive computational cost.

6.3 Experimental procedure

We focus on two key issues that have not been addressed by previous investigations on roughness effects: We directly model realistic surface roughness that is extracted using optical profilometry. This is made possible by using high resolution DNS analysis (that is validated using concurrent micro-PIV experiments) which allows us to link nano-scale roughness to far-field flow features. We also focus on flows at low Reynolds number where viscous forces dominate, which is common for microfluidic devices, and extensively characterize the effect of varying surface roughness.

The experimental microchannel in this study was fabricated using PDMS and glass. The PDMS part was a replica made from an SU-8 mold and forms three walls of the microchannel. The PDMS part and a glass substrate (slide) were then oxygen-plasma bonded together, creating

a completely enclosed microchannel for fluid transport, with the glass forming the fourth [131] wall of the channel. We implemented hydrofluoric acid (HF) etching to create a surface roughness on the glass substrate that is reproducible and characterizable as a function of etching time [4]. A desired stochastic surface roughness can be fabricated according to the etching time and solution concentration [4].

In this study, we used an unetched glass and a roughened glass obtained as follows. A glass slide (25 mm × 75 mm, Erie Scientific Company, Portsmouth, NH) was etched in buffered HF (6:1 volume ratio of 40% NH_4F in water to 49% HF in water; etch rate calibrated to 72 nm/min) for 30 minutes and immediately rinsed in deionized water for 5 minutes. After rinsing, the etched-glass slide was dried using nitrogen gas before being oxygen-plasma bonded to the PDMS replica. Etching time was limited below 40 minutes since longer etching times compromised the glass transparency necessary for micro-PIV measurements. The 30-minute etched glass is referred to simply as "etched glass" from here onward.

The microchannel's surface topography was obtained using a 3D Optical Surface Profiler (NewView™ 7100, Zygo Corporation, Middlefield, CT). The optical profilometer provided a scan area of 470 μm × 350 μm , with a lateral resolution of 0.73 μm and height resolution of 0.1 nm. The surface data obtained by the optical profilometer was directly used to model the surface roughness on the bottom surface of the CFD microchannel at the same spatial resolution.

In our experiments, micro-PIV visualization of microfluidic flow was realized with a microscopic imaging system that visualizes a small area within the microchannel. In this micro-PIV experiment, the working fluid, deionized water, was seeded with 1 μm diameter Nile-red fluorescent carboxylate-modified microspheres (FluoSpheres, Invitrogen Corporation) as flow-tracing particles at a concentration of 0.04%. The seed particles were illuminated using a double-

pulsed Nd:YAG laser. Images of the illuminated tracing particles were captured using a CCD camera. A 40x 0.6 NA objective lens paired with a 0.45x coupling, resulted in a total magnification of 18X and a depth of correlation of 7.8 μm [17]. Further details of the micro-PIV system can be found in Li and Olsen [18]. The overlapped area of adjacent interrogation windows was 50% resulting in an in-plane velocity vector spacing of 1.5 μm . In total, 1500 micro-PIV image pairs were captured at each depth and analyzed using the sum-of-correlation algorithm [19,20,21] to obtain the velocity field.

6.4 Modeling

The surface data obtained by the optical profilometer was used to model the surface roughness on the bottom surface of the CFD microchannel at the same spatial resolution. This ensured that the surface roughness used for CFD simulations was experimentally derived and non-periodic. Figure 1 shows the computational domain. The trapezoidal shape of the micro-PIV experimental microchannel (caused by the fabrication process) has identical cross-sectional dimensions as the CFD microchannel. The length of the channel was 350 μm (this is more than 10 times the surface roughness autocorrelation length (12.9 μm for the etched surface)). The channel is 390 μm wide on the top and 470 μm on the bottom. The height of the channel is 51.03 μm . The grid was composed of 12.3 million hexahedral elements. The elements were concentrated near the walls to accurately capture the effect of the surface roughness and boundary layers. The clustering of hexahedral elements was greater near the rough surface. For the etched glass, the roughness of the glass is one order of magnitude larger than the roughness of the PDMS. Since we expect the effect of PDMS roughness to be small in comparison with the glass roughness (this hypothesis is validated via comparison between CFD and PIV data) the

PDMS surface roughness is neglected and we assume a smooth top surface for the CFD simulations [37].

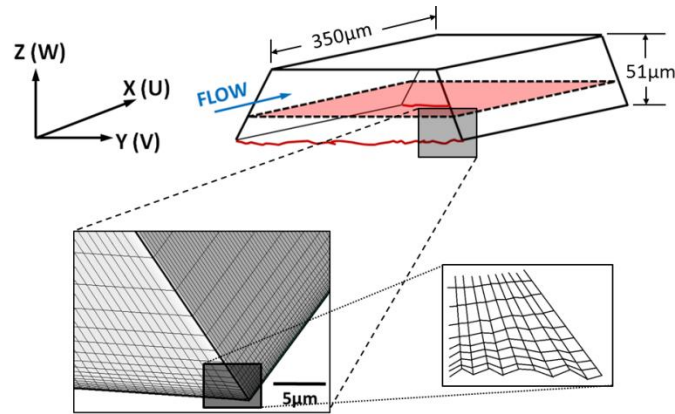


Figure 1 - The geometry and mesh detail of the computational microchannel domain. The roughness height on the zoomed-in section is exaggerated for clarity. The width of the channel is $460\mu\text{m}$ at the rough surface.

The full Navier-Stokes equations were solved assuming incompressible flow and constant fluid temperature. We utilized a highly scalable implementation of an incompressible flow solver using the Finite Element Method that incorporates Streamline-upwind/Petrov-Galerkin (SUPG) [22] and pressure-stabilizing/Petrov-Galerkin (PSPG) [23] terms for numerical stabilization. The applicability of the Navier-Stokes equation (validity of the continuum hypothesis) is ensured due to the fact that the Knudson number calculated on the smallest element (2.7×10^{-4}) was less than 10^{-2} [24]. We applied no-slip boundary conditions on the walls. Zhu et al. [25] showed that for a microchannel with hydrophilic surfaces and a hydraulic diameter larger than $30\ \mu\text{m}$, the no-slip boundary condition is valid. In addition to PDMS being hydrophilic, the etched glass is also hydrophilic [26]. Both surfaces underwent an oxygen plasma treatment during the fabrication process, which is known to increase hydrophilicity [27]. Water contact angle measurements on etched glass yielded a value of 29.5° , confirming its hydrophilicity. Potential micro-sized air

bubbles will also have no effect on slip [28]. A pressure drop boundary condition between inlet and outlet was maintained. An *initial guess* for the pressure drop was to match the experimentally determined flow rate using the Hagen-Poiseuille flow equation (which is for a circular channel), $\Delta P = \frac{128\mu L Q}{\pi D^4}$, where L is the length of the channel, μ is the dynamic viscosity, Q is the volumetric flow rate, and D is the hydraulic diameter. We analyzed cases using flow rates of 0.001mL/min, 0.01mL/min, 0.1mL/min which corresponds to a Reynolds number of 0.065, 0.65, and 6.5, respectively.

The effect of surface roughness was investigated by looking at the fluid structures that evolve from the rough surface. We focused on fluid structures consisting of velocity perturbations caused by the roughness itself. In order to characterize these velocity perturbations, we used autocorrelation analysis, energy spectrum analysis, and visual analysis. By examining the fluid structure characteristics as a function of height from the rough surface, a zone of influence from the rough surface was established.

The autocorrelation function, $C(\tau)$ was estimated for a velocity field in a plane to find β^* , the autocorrelation length. The autocorrelation length is defined as the lag distance where the autocorrelation function decays to $1/e$. Autocorrelation analysis was performed on velocity fields as slices in the xy-plane, highlighted in Fig. 1, at increasing heights from the rough surface, in order to extract the influence of surface roughness as a function of height. Note that the autocorrelation is calculated using the velocity-component deviations from ideal flow (perturbations). The interrogation region was taken toward the center of the microchannel away from the side-walls and entrance/exit to eliminate the side-wall boundary layer and boundary condition effects. The ACL of the v-velocity perturbations was used for validation between experiments and computational results.

6.5 Result and discussion

Figure 2 shows the ACL as a function of height from the rough surface for computational results as well as experimental data. The uncertainty bars for the experimental data represent one standard deviation from the mean value. The experimental ACL was taken at 25.5 μm above the rough surface. The relationship and value of ACL between etched and unetched surfaces was consistent between computations and experiments. Table I summarizes and compares the ACL values between experiments and CFD at 25.5 μm above the rough surface for etched and unetched surfaces.

Table I. Comparison of experimental and DNS metrics at 25 μm from rough surface [μm].

Flow Rate [ml/min]	Surface Type	ACL		Energy Spectra Slope Ratio	
		Exp.	DNS	Exp.	DNS
0.1 (Re = 6.5)	Etched	17.4 \pm 1.7	17.3 \pm 0.6	1.73 \pm 0.04	1.82 \pm 0.03
	Unetched	14.2 \pm 3.4	15.0 \pm 2.7		
0.01 (Re = 0.6)	Etched	16.7 \pm 1.6	17.5 \pm 1.2	2.86 \pm 0.17	2.15 \pm 0.04
	Unetched	16.8 \pm 1.4	15.0 \pm 2.9		

If the roughness effect on the fluid did not persist above the surface, then the ACL values would tend toward zero (i.e. uncorrelated noise). However, the ACL starts small and increases to

a constant value. This suggests that the effect from the surface roughness persists in the flow well above the rough surface. The coherent structures start small near the rough surface and combine with increasing height from the rough surface. Figure 2 shows that the ACL as a function of height from the rough surface is very consistent across flow rates. Notice that while the ACL is insensitive to flow rate for these diffusion-dominated flows, it is sensitive to the roughness characteristic of the surface.

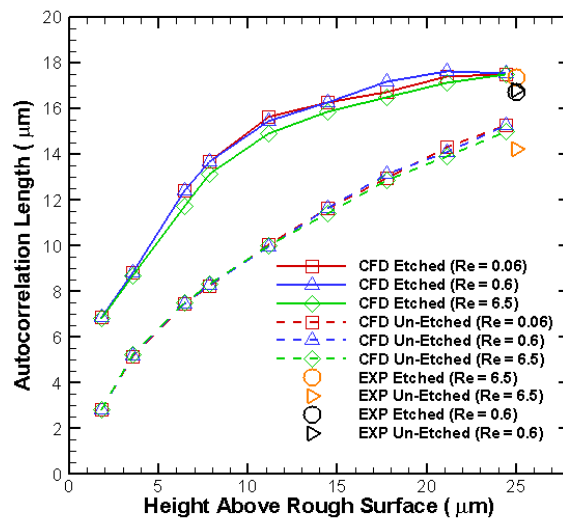


Figure 2 - Autocorrelation lengths (ACL) of experimental and CFD v -velocity-component perturbations for both etched and unetched surfaces at all flow rates, Q [ml/min].

While the autocorrelation length gives valuable information about the fluid structures, an energy spectra analysis can reveal the energy cascading effects of the surface roughness. Energy spectra analysis has been used successfully for velocity field analysis in a variety of fluid phenomena [30]. The energy spectrum is denoted as $E(k)$, where \hat{u} is the discrete Fourier transform of the velocity field [31] on a structured mesh with $n \times m$ points, where $\bar{E}(k) = \frac{1}{2} |\hat{u}(k, t)|^2$.

$$\hat{u}(\mathbf{k}_x, \mathbf{k}_y, t) = \frac{1}{\sqrt{mn}} \sum_{j_1=0}^{m-1} \sum_{j_2=0}^{n-1} u(x, y, t) e^{-i\left(\frac{j_1 k_x}{m} + \frac{j_2 k_y}{n}\right)} \quad (1)$$

$$E(\mathbf{k}) = \sum_{\mathbf{k}-\Delta\mathbf{k} \leq \mathbf{k} \leq \mathbf{k}+\Delta\mathbf{k}} \bar{E}(\mathbf{k}_x, \mathbf{k}_y) \quad (2)$$

Figure 3 shows the energy spectra of the total velocity perturbations. Figure 3a reveals that the energy cascade across wavelengths has a very similar structure throughout the spectrum of flow rates over etched glass, *again supporting the notion of insensitivity of effect of surface roughness as a function of flow rate*, at small flow rates. Clearly, the energy spectra in Figure 3b reveal that larger amounts of energy in the form of velocity perturbations are produced by etched glass. Also, Fig. 3b shows that the energy produced by etched glass persists higher into the microchannel compared to unetched glass. There is a greater decay in the energy for unetched glass as the height from the rough surface increases, whereas the energy from the etched glass tends to persist. This is clearly seen in the slope of the energy spectra. For the etched and unetched surfaces this is approximately -4.75 and -8.64, respectively. Not only is the perturbation energy larger for etched glass, but the larger slope for etched glass compared to unetched glass means there is a greater transfer of energy for etched glass [32]. Table I also compares the energy spectra slope ratios between experiments and simulations. The ratio is defined as the energy spectra of unetched/etched surfaces, and the numerical results agree with the experimental results within 5% for the higher flow rate.

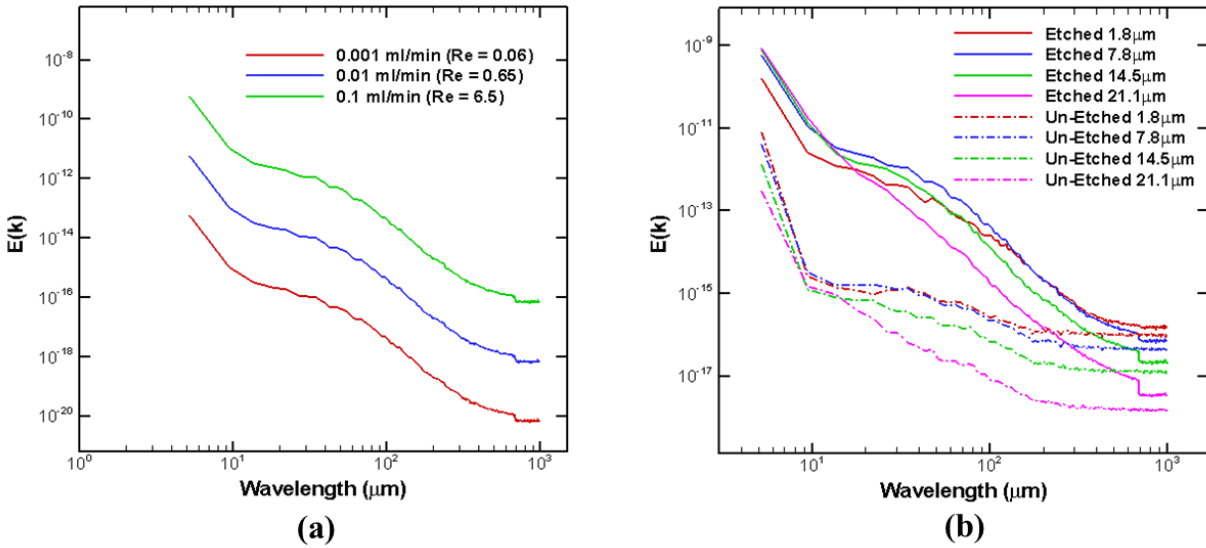


Figure 3 - Energy spectra analysis of u-v-w velocity perturbation sum of squares: energy spectra of the velocity field as a function of flow rate (a) at $7.82 \mu\text{m}$ above the rough surface of etched glass, and the energy spectra (b) of $Re = 6.5$ of etched and unetched surfaces.

Finally, we utilized visual representation of the velocity to investigate the fluid structure away from the surface by plotting velocity contours in the xz -plane. Note the dramatic effects due to roughness as seen in Fig. 4(a-d) which shows the v -velocity contours for both unetched and etched glass at multiple flow rates. There are large velocity plumes that originate from the rough surface and erupt to the mid-plane of the microchannel. The R_{rms} of the etched glass (~ 19 nm) is slightly more than an order of magnitude greater than the un-etched glass (~ 1 nm), and not surprisingly, there is an order of magnitude increase in the velocity fluctuations between the etched and unetched surfaces. What is interesting is that the small perturbations originating from the rough surface seem to combine and merge into larger structures as the height from the surface increases. These combinations give rise to the velocity plumes seen in Fig. 4.

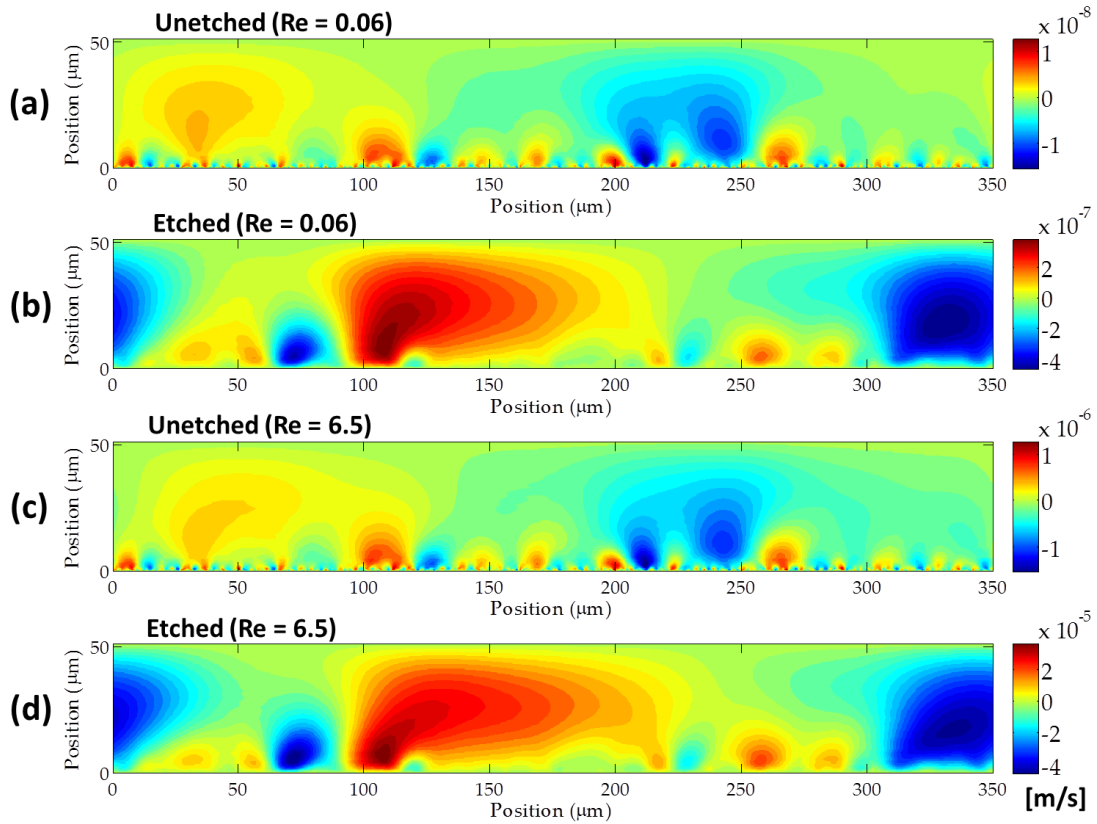


Figure 4 – V-velocity component contour plots of (a) $Re = 0.06$ un-etched, (b) $Re = 0.06$ etched, (c) $Re = 6.5$ un-etched, and (d) $Re = 6.5$ etched (fluid flow goes from left to right). The xz -plane slices were taken $175\mu\text{m}$ away from the microchannel side wall.

We have shown that the effect of stochastic nano-scale surface roughness on microfluidic flow can be studied using computational fluid dynamic DNS simulations. Additionally, we have shown that validation between micro-PIV experiments and a large DNS simulation is possible using autocorrelation and energy spectra. CFD analysis lends to a deeper understanding of the characterization of the fluid flow within the microchannel, and the highly resolved DNS simulations reveal the flow to be characterizable. We show that for a range of flow rates that are diffusion dominated, the energy transfer is consistently characterizable. Autocorrelation and velocity contour analyses showed that the nano-scale surface roughness produced small

structures that combine and persist well above the rough surface. In addition, the energy spectra analyses show the small eddies produced by the etched surface give rise to higher energy eddies that decay more slowly than eddies produced by the unetched surface.

6.6 Conclusions

The chemical etching surface treatment and other stochastic rough surfaces, even at the nano-scale, can be characterized and potentially be harnessed across a range of fluid flow rates. Devices that use microchannels such as lab-on-a-chip medical devices can potentially be tuned and further optimized for their respective applications such as reagent mixing, bubble creation and transport, fluid transport, cell manipulation by leveraging the effects of stochastic surface roughness. We envision this effect to be particularly useful in non-Newtonian fluids, which are frequently encountered in lab-on-a-chip medical devices.

6.7 References

1. I. Rodriguez, P. Cpicar-Mihalic, C. Kuyper, G. Fiorini, and D. Chiu, *Analytica Chimica Acta*. **496**, 205–215 (2003).
2. M. Kolli, M. Hamidouche, N. Bouaouadja, and G. Fantozzi, *J. of the European Ceramic Society* **29**, 2697–2704 (2009).
3. A. Muscat, A. Thorsness, and G. Montano-Miranda, *J. Vac. Sci. Technol. A* **19**, 1854–1861 (2001).
4. J. Ren, B. Ganapathysubramanian, and S. Sundararajan, *Journal of Micromechanics and Microengineering*. **21**, 025012 (2011).
5. K. Hosokawa, T. Fujii, and I. Endo, *Anal. Chem.* **71** (20), 4781-4785 (1999).

6. G. Londe, A. Chunder, A. Wesser, L. Zhai, and H.J. Cho, *Sensors and Actuators B: Chemical*. **132** (2), 431-438 (2008).
7. A. Gunther, S. Khan, M. Thalmann, F. Trachsel, and K. Jensen, *Lab on a chip*. **4**, 278-286 (2004).
8. G. Silva, N. Leal, and V. Semiao, *International J. of Heat and Fluid Flow*. **29**, 1211-1220 (2008).
9. A.S. Rawool, S.K. Mitra, and S.G. Kandlikar, *Microfluid Nanofluid*. **2**(3), 215-221 (2005).
10. W. Jeon and C.B. Shin, *Chemical Engineering Journal*. **152**, 575-582 (2009).
11. J. Koo and C. Kleinstruer, *Journal of Micromechanics and Microengineering*. **13**, 568-579 (2003).
12. J. Liu, M. Wang, S. Chen, and M. Robbins, *Journal of Computational Physics*. **229**, 7824-7847 (2010).
13. J. Valdes, M. Miana, J.L. Pelegay, J.L. Nunez, and T. Putz, *International Journal of Heat and Mass Transfer*. **50**, 1865-1878 (2007).
14. J. Valdes, M. Miana, M. Martinez, L. Gracia, and T. Putz, *International Journal of Heat and Mass Transfer*. **51**, 4573-4582 (2008).
15. R. Xiong, *Journal of Fluids Engineering*. **133**, 031102-1-031102-7 (2010).
16. R. Xiong and J.N. Chung, *International J. of Heat and Mass Transfer*. **53**, 3284-3291 (2010).
17. C. J. Bourdon, M.G. Olsen, and A.D. Gorby, *Journal of Fluids Engineering-Transactions of the Asme*. **128**(4): p. 883-886 (2006).
18. H. Li and M.G. Olsen, *International Journal of Heat and Fluid Flow*. **27**, 123-134 (2006).
19. C.D. Meinhart, S.T. Wereley, and J.G. Santiago, *J. of Fluids Engineering*. **122**, 285-289 (2000).
20. M.G. Olsen, and R.J. Adrian, *Experiments in Fluids*. **29**, S166-S174 (2000).
21. C.J. Bourdon, M.G. Olsen, and A.D. Gorby, *Meas. Science and Technology*. **15**, 318-327 (2004).
22. T. Hughes and A. Brooks, *Finite Element Methods for Convection Dominated Flows* (ed. Hughes T.J.R.) ASME New York, Wiley (1979).
23. T.E. Tesduyar, S. Mittal, S.E. Ray, and R. Shih, *Computer Methods in Applied Mechanics and Engineering*. **95**, 221-242 (1991).
24. M. Gad-el-Hak, *Trans. ASME J: J. Fluids Engineering*. **121**, 5-33 (1999).
25. L. Zhu, D. Tretheway, L. Petzold, and C. Meinhart, *Journal of Computational Physics*. **202**, 181-195 (2005).
26. S. Sikalo, M. Marengo, C. Tropea, and E.N. Ganic, *Experimental Thermal and Fluid Science*. **b**, 503-510 (2002).
27. H. Gulec, K. Sarioglu, and M. Mutlu, *Journal of Food Engineering*. **75**, 187-195 (2006).

28. Micro-sized air bubbles have been known to create an effective slip at the wall by forming an immiscible fluid layer where the slip increases. However, if the capillary pressure is great enough to force the air out of the surface features, then the no-slip boundary condition is again valid, as proved by Barrat and Bocquet [29]. The minimum pressure required to force fluid into a parallel slit of width h is: $P_o = \frac{2(\gamma_{LS}-\gamma_{SV})}{h}$ which is smaller than the pressure gradient applied in these experiments.
29. J. Barrat and L. Bocquet, *Physical Review Letters*. **82 (23)**, 4671-4674 (1999).
30. S. Singh and S. Mittal, *International J. of Computational Fluid Dynamics*. **18**, 671-679 (2004).
31. W.H. Press, S.A. Teukolsky, W.T. Vetterling, & B.P. Flannery, *Numerical Recipes in C: The Art of Scientific Computing*, Second Edition (New York: Cambridge University Press, 1992).
32. P.K. Kundu and I.M. Cohen, *Fluid Mechanics*, Fourth Edition (Kidlington, Oxford: Elsevier Inc., 2008).
33. E. Gogolides, M. Vlachopoulou, K. Tsougeni, N. Vourdas, A. Tserepi, *International Journal of Nanomanufacturing (IJNM)*, **6**, 152-163 (2010).
34. E. Gogolides, V. Constantoudis, G. Kokkoris, D. Kontziampasis, K. Tsougeni, G. Boulousis, M. Vlachopoulou, A. Tserepi, *J. Phys. D: Appl. Phys.* **44**, 174021 (2011).
35. B. Bhushan, Y. C. Jung, *Prog. Mater. Sci.* **56**, 1–108 (2011)
36. K. Tsougeni, D. Papageorgiou, A. Tserepi and E. Gogolides, *Lab Chip* **10**, 462–9 (2010)
37. All the data analysis (for both experimental and CFD) is done on regions far from the entrance, exit and side walls, thus effects of entrance, exit and side-walls can be safely neglected.

CHAPTER 7. INVESTIGATION OF NANOSCALE SURFACE ROUGHNESS ON NON-NEWTONIAN MICROFLUIDIC FLOW-EXPERIMENT

Jing Ren, Baskar Ganapathysubramanian, Michael Olsen and Sriram Sundararajan

7.1 Abstract

Surface roughness was identified as an essential parameter in microfluidics and widely studied during the past several decades. While the studies on fluid flow over patterned, deterministic rough surface have provided us understanding of large level of roughness (roughness height with the order of several microns) effect on flow behavior, recent study has shown that realistic random surface roughness, even at nanoscale, has measurable effect on Newtonian microfluidic flow. This provides insights in roughness harness for lab-on-chip and bioMEMS applications involving non-Newtonian fluids, such as reagent mixing and single cell manipulation. In this study, the influence of random surface roughness on non-Newtonian microfluidic flow was investigated. Dilute xanthan gum was used as a blood-analog fluid for evaluation. Microfluidic devices with desired roughness on the channel walls were fabricated. The surface roughness was characterized using an optical 3D Profilometer. Micro Particle image velocimetry (microPIV) was utilized to measure the flow velocity fields inside the microchannels to assess the affect of random roughness.

Keyword

Random roughness · blood analog fluid · PIV · microfluidics · laminar flow · non-Newtonian flow

7.2 Introduction

A large number of studies over the past century have steadily advanced our understanding of the surface roughness effect on fluidic flow performance. Experimental studies were carried out to investigate mainly the pressure drop and friction factor in fluidic tubes with different relative roughness, through which the surface roughness was considered an important parameter in fluid flow. A detailed summary on the characterization of surface roughness effect on fluid flow can be found in Taylor et al. [1]. The pioneering work of Colebrook [2], Moody [3] and Nikuradse [4] provided us a mathematical estimate of surface roughness effect on fluidic system with relative roughness (roughness height/ D_H , and D_H is the hydraulic diameter of the channel) under 5%. Kandlikar et al. [5, 6] further modified the traditional characterization methods by adding the effect of constricted flow diameters and extended this investigation to 14% relative roughness.

Over the past several decades, Advances in microfabrication techniques facilitate the development of MEMS and lab-on-chip, bringing out exciting revival of classical fluidic theories. The size of modern microfluidic devices keep shrinking from millimeter to the level of 1-100 μm . Size effect and device downscaling leads to many interdisciplinary researches, including microscale fluid mechanics, computational fluid dynamics, micro/nano scale surface processing and measurement, etc. Beyond the academic perspective, the benefits of downscaling reach to medical and biological areas. The ability of processing large amount of fluid mixing and

chemical reaction at small volumes simultaneously opens possibility of diverse application in biology and biotechnology. Modern applications of using microfluidic chip includes pathogen detection [7, 8], DNA culture and analysis [9, 10], electrophoretic separations [11], etc.

Novel products have been developed based on complex microfluidic systems to provide faster speed, better and more reliable performance at more affordable prices. For example, small size skin-contact-actuated dispenser/pump has been produced to help patients with convenient transdermal drug injection and delivery [12]. Disposable smart lab-on-chip device has been developed for clinical point-of-care testing and diagnostics [13].

Keep in mind that due to the small scale size effect and size shrinking, especially some flow applications are at extremely small scale like several micrometers, even several nanometers, a more complete understanding of the flow behavior inside the microfluidic devices is required in order to further improve the design of current bioMEMS and lab-on-chip products. As the size of fluidic devices “going micro”, the relative roughness inside the microfluidic channel increases significantly. As a result, surface roughness somehow should not be neglected anymore as in most previous microfluidic studies. As many flow operations are necessarily executed under low Reynolds number conditions, surface roughness therefore becomes a more essential parameter that affect the flow [14].

Of particular interest, results of extensive studies indicate that surface roughness affects fluid flow behavior under low Reynolds numbers in microfluidic channels. Numerical simulations of micro flow in rough channels [15] showed that bulk flow velocity and the volumetric flow rate decrease in different rates as the roughness increases. Studies on the effect of surface roughness on friction force [16], pressure drop [6, 17], heat transfer in single-phase flow [5] and laminar-turbulent transition [18] indicate the necessity of precise control of the

surface morphology inside the fluidic device for the purpose of enhancing the reliability and performance of the fluidic system [19]. Experimental results of blood flow in rough microchannels [20] emphatically showed that surface roughness affects blood viscosity due to boundary effects. Application of surface roughness for gradient generation in microfluidic system has also been widely studied [21-23].

In most of these studies, researchers relied on micro-machining or micro-fabrication techniques to produce deterministic roughness via designed shapes and patterns inside the microchannels. It is well known that almost all mechanical or chemical processing inherently produces random roughness on real surfaces [24] and consequently most engineering surfaces are random. However, the role of random roughness on microfluidic flow behavior remains relatively unexplored. This aspect will become increasingly important as channel sizes continue to decrease in micro/nanofluidic applications.

Experimental work on surface roughness tailoring by Ren et al. [25] showed that hydrofluoric etching is capable of generating roughness on glass substrate in a certain range: autocorrelation length increases in the range of 1 to 4 μm . Besides the chemical wet etching, a hybrid surface tailoring method combining reactive ion etching and colloidal masking to produce random surfaces with desired roughness parameters at the micro/nano scale was also reported [26].

Our recent study combining experimental microPIV data and CFD simulation revealed that under low Reynolds number condition, nanoscale surface roughness (relative roughness less than 0.01%) causes flow perturbations that extend up to the center plane of a microfluidic channel of 50 μm in height [27]. The study focused on flows at low Reynolds number where viscous forces dominate, and directly modeled the realistic roughness which was extracted from

the digitized optical profilometry image of the channel surface. Through high resolution DNS analysis and microPIV validation, the nano-scale surface roughness was successfully linked to far-field features.

Based on this result, in this study, we investigated the effect of stochastic nanoscale surface roughness on non-Newtonian flow through micro particle image velocimetry (microPIV) measurement. We fabricated three rectangular microfluidic devices using PDMS and glass substrate. The surface roughness generation method using hydrofluoric etching was adopted to the fabrication process to obtain desired roughness on the glass channel wall of each device. We will describe the experimental methods of roughness generation and characterization, microfluidic device fabrication, and the microfluidic flow measurement using microPIV.

7.3 Experimental methods

7.3.1 Roughness generation and measurement

Glass is one of the more important and common materials widely used in micro channel fabrication [28]. In this study, we use glass and PDMS for microfluidic device fabrication, due to the transparency requirement of velocity measurement using micro particle Image Velocimetry (microPIV) system. Glass slides (25 mm × 75 mm, Erie Scientific Company, Portsmouth, NH) were etched in buffered HF (6:1 volume ratio of 40% NH₄F in water to 49% HF in water) for 30 and 40 minutes to obtain difference level surface roughness. Etch rate was calibrated as 72 nm/min. After etching, the slides were rinsed in DI water for 5 minutes then dried in nitrogen flow. An un-etched glass slide was also prepared for comparison.

The microchannel's surface topography was obtained using a 3D Optical Surface Profiler (NewView™ 7100, Zygo Corporation, Middlefield, CT). The optical profilometer provided a

scan area of $480 \mu\text{m} \times 360 \mu\text{m}$, with a lateral resolution of $0.73 \mu\text{m}$ and height resolution of 0.1 nm . The surface height data was exported into MATLAB to analyze surface roughness including amplitude (Ra) and spatial (ACL) roughness parameters.

A comparison of the surface morphology between the three glass substrates is shown in figure 1. The chemical wet etching significantly roughened the glass surface within 40 minutes. Also the surface shows larger structures as etching time increases.

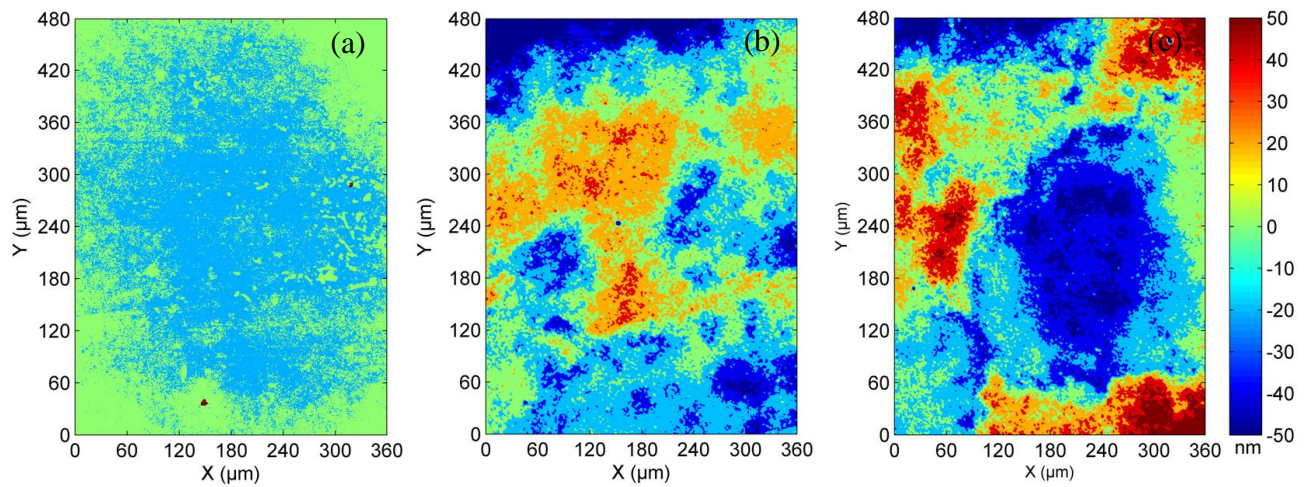


Figure 1. A schematic representing the scanned surface of each etching time: (a) un-etched glass; (b) 30 min etched; (c) 40 min etched glass surface.

Random surface roughness can be characterized by amplitude and spatial parameters [29]. Center Line average (Ra) is a most commonly used amplitude parameter, which measures the relative departure of the profile in the vertical direction [29]. The definition of Ra is given as

$$Ra = \frac{1}{N} \sum_{i=1}^N |z_i - m| \quad (1)$$

where N is the number of total sampling points, z is the surface height, m is mean line of the surface profile.

Autocorrelation length (ACL) is a common spatial parameter which measures the degree of randomness of the surface roughness [30]. It is defined as the length over which the autocorrelation function decays to a small fraction of its original value. Many etched surfaces are widely assumed to produce an exponential autocorrelation function [29] given as

$$c(\tau) = \exp(-\tau / \beta) \quad (2)$$

where τ is the spatial separation. Autocorrelation length of this exponential autocorrelation function is defined as the distance at which value of the $c(\tau)$ drops to $1/e$ of the initial value, which is equal to β [31].

Another commonly used parameter for roughness characterization is the relative roughness, which is defined as $\gamma = 100\% * Ra/D_H$, and D_H is the hydraulic diameter of the channel. Table 1 listed the values of roughness parameters including Ra, ACL and γ of the three tested microfluidic channels. Notice that the relative roughness is very small (from 0.02% to 0.1%), to our knowledge, it is the first attempt to directly measure and quantify the effect of surface roughness on the velocity field at this very small scale.

Table 1. Comparison of surface roughness of processed glass and PDMS

Surface type	Roughness		
	Ra (nm)	ACL (μm)	γ
un_etched	3.28	1.33	0.003%
30 min	24.65	21.9	0.02%
40 min	94.86	39.11	0.1%
PDMS	2.44	0.69	0.002%

7.3.2 Microfluidic device fabrication

In this study, microchannels were fabricated using the etched glass substrate and PDMS. Figure 2 shows the process flow of the channel fabrication. SU8 mold containing the microfluidic channel features was fabricated using lithography technique. Replica was made by pouring PDMS on the SU8 mold and unmolding the cured PDMS part carefully. Finally, the PDMS replica with the microfluidic channel features was bonded to the etched quartz substrate after oxygen plasma treatment. Detailed fabrication process can be found in Ren, et al. [32].

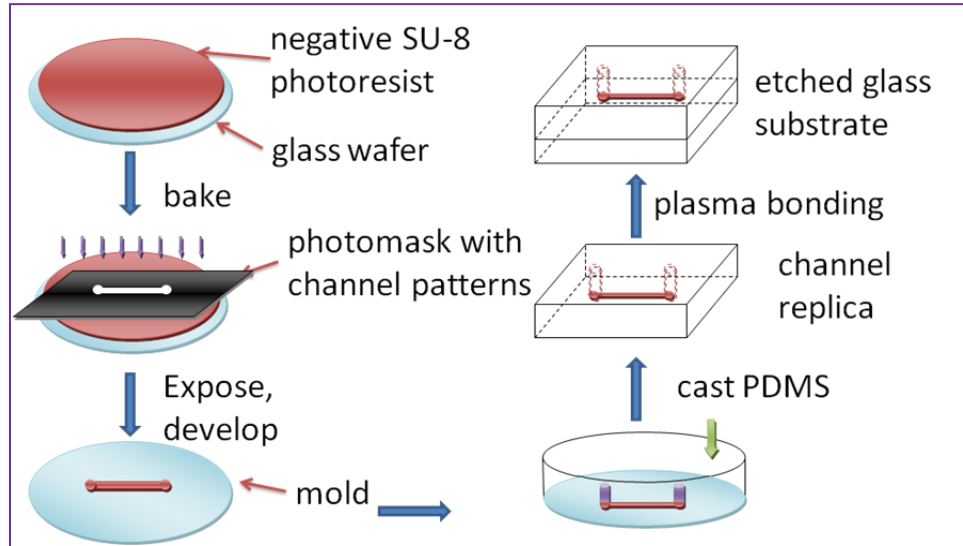


Figure 2. Processed flow of the microchannel fabrication

A SEM image of the PDMS replica made from the SU-8 mold containing the microchannel structure before bonded to the glass substrate is shown in figure 3. The height was measured as $49.66 \mu\text{m}$ and width was $404.3 \mu\text{m}$. The length of the microfluidic channel was 25mm. Hydraulic diameter of the channel $D_H = \frac{4A}{P} = 88.46 \mu\text{m}$.

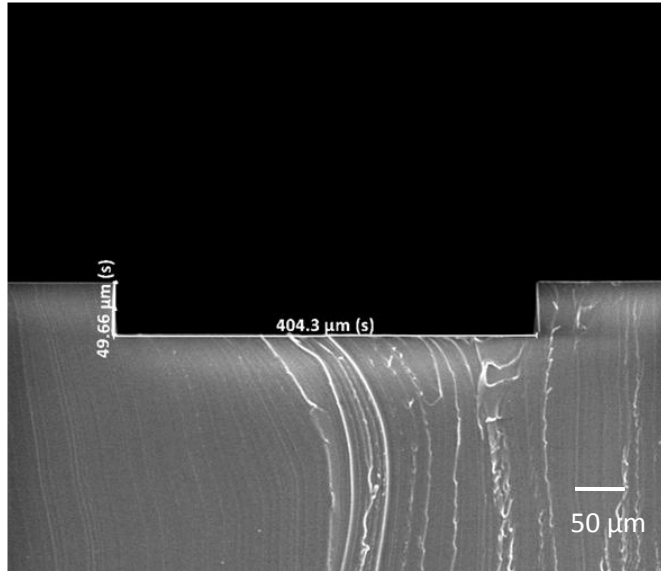


Figure 3. A PDMS replica containing the microchannel structure before bonded to the glass substrate

Tubing was attached to the inlet and outlet of the microfluidic channel. Sealing performance of the devices was tested by pumping DI water with tracing particles (nile red FluoSpheres, Invitrogen Corporation) through and the sealing performance was proved satisfying.

7.3.3 Blood analog fluid

The shear thinning and viscoelastic behavior of blood are resulted from the red blood cells. The erythrocyte concentration, aggregation and deformation plays an important role in the rheological characteristics of the human blood [33]. Blood analog fluids need be meet the shearing thinning and viscoelastic behavior as non-Newtonian fluids.

In most of the current blood analog, non-Newtonian fluids measurement study, dilute xanthan gum is widely used due to its weak-gel shear-thinning property. In addition, xanthan gum is soluble in water, providing high viscosity at very low concentrations [34-39]. Good

pseudoplasticity allows the solution to be poured and pumped easily [39, 40]. These properties of xanthan gum solution make it an ideal analog fluid for rheology study of non-Newtonian fluids.

Bandulasena et al. reported a use of low concentration xanthan gum to study the shear-thinning behavior of power law non-Newtonian fluids [41]. Weight concentrations of 0.005%, 0.01% and 0.025% were used in the study. The velocity fields of the dilute xanthan gum solution in a microchannel were measured by microPIV. Compared to the CFD simulation, the measurement error was less than 5%. This study provides insights of using microPIV equipment in non-Newtonian fluid flow measurement.

Gijssen et al. [42] used KSCN-X, mixed concentrated potassium thiocyanate in water (71% in weight) with addition of 250 ppm Xanthan gum. The KSCN solution was used as a Newtonian control fluid which has good transparency for Laser Doppler Anemometry measurement. And the added xanthan gum solution provide the shear thinning and viscoelastic behavior as non-Newtonian fluid.

Wickramasinghe et al. [43] used a very dilute xanthan gum (0.0075%-0.04%) added into deionized water/glycerol or deionized water solution as a blood analog fluid. A power law model was used in the simulation to predict the rheological behavior.

In this study, very dilute xanthan gum solution was used as a blood analog fluid. Two weight concentrations of 0.025% and 0.1% were used. The xanthan gum powder was diluted in deionized water with pH value of 7. The low conductivity of the deionized water helps reduce the agglomeration of the seeding particles [44], which is extremely helpful in this study since the bottom rough wall tends to trap particles and form agglomeration. In addition, the same deionized water was also tested as a working fluid for comparison as a Newtonian fluid.

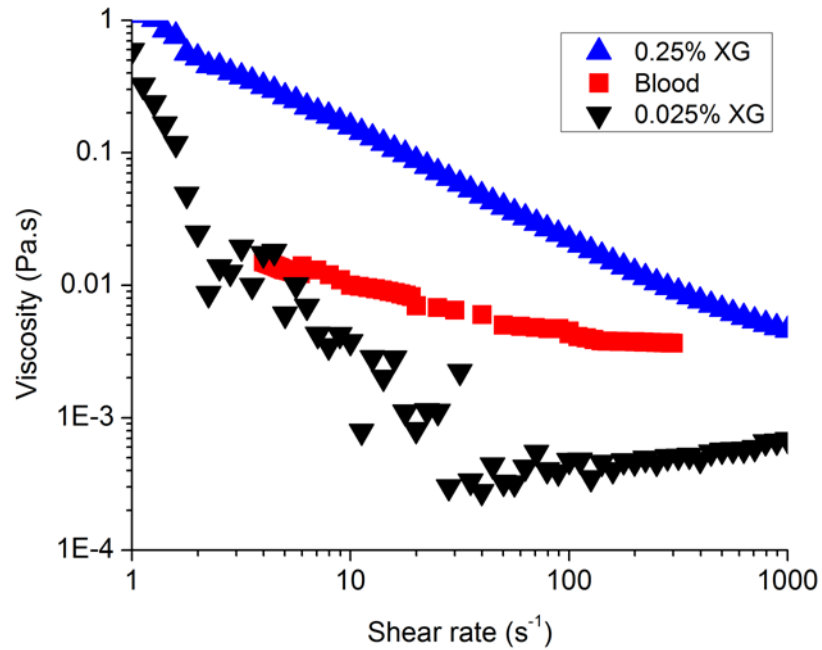


Figure 4. Steady shear properties of the dilute xanthan gum solution, compared to the property of blood. The blood data was taken from Shin (2002) [45].

Viscosity of blood is in a relative wide range (0.001-0.1) based on hematocrit difference and varies among donors [45]. The data in figure 4 shows the viscosity of blood lies between xanthan gum solution with concentrations of 0.025% and 0.25%. Therefore xanthan gum solution with 0.025% and 0.1% concentration can be considered as reasonable blood-analogue fluids.

7.4 PIV measurement of the velocity field

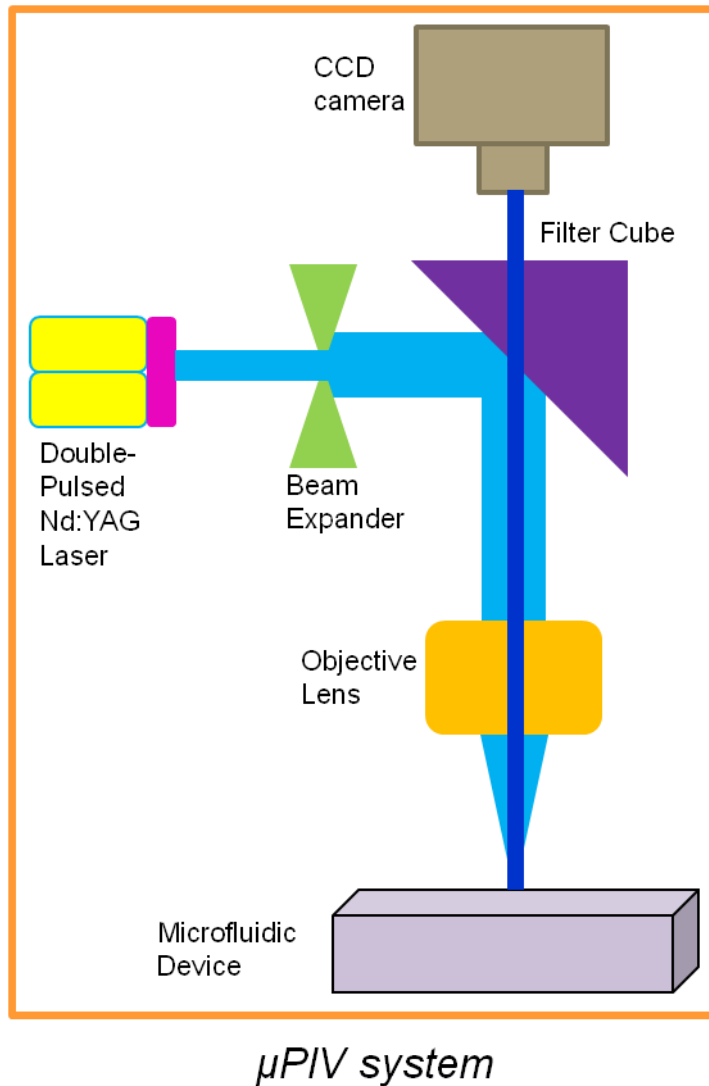


Figure 5. Micro-PIV apparatus and methodology

The working fluids were seeded with 1 μ m diameter fluorescent Nile red flow-tracing particles (Nile red FluoSpheres, Invitrogen Corporation). The weight concentration of the particle solution is 0.02% to provide a sufficient particle density for flow velocity tracking [46].

Illumination of the micro-channel was provided by a double-pulsed Nd:YAG Continuum Minilite laser. Flow images were captured by a LaVision Imager Intense CCD camera. In this

study, a 40×0.6 NA objective was coupled with a $0.45 \times$ coupler, resulting in a total magnification of $18 \times$ and a depth of correlation of $7.8 \mu\text{m}$ [47]. Interrogation windows of 32×32 pixels were chosen. The overlapped area of adjacent interrogation windows is 50%. Delay time of the double-pulsed laser was adjusted at each depth so that the tracing particles move approximately $\frac{1}{4}$ of the interrogation window between the two exposures. 500 μPIV images were acquired at each location and analyzed using the sum of correlation algorithm. Velocity fields were measured at 9 different depths from the bottom wall (rough glass substrate) to the top wall (PDMS), respectively at $5 \mu\text{m}$, $10 \mu\text{m}$, $15 \mu\text{m}$, $20 \mu\text{m}$, $25 \mu\text{m}$, $30 \mu\text{m}$, $35 \mu\text{m}$, $40 \mu\text{m}$, $45 \mu\text{m}$. Three experimental sets were repeated on each channel. Two flow rates of 0.1ml/min and 0.01ml/min were applied.

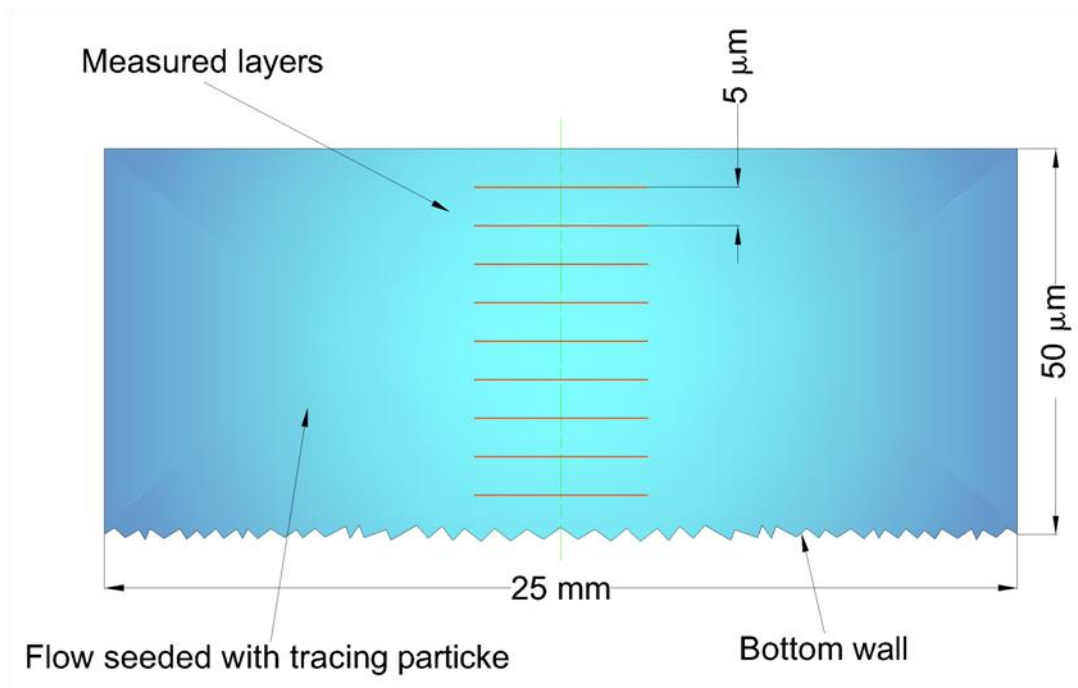


Figure 6. Measured depths in micro-PIV experiment

7.5 Result and discussion

Velocity field was computed from the microPIV images using sum of correlation algorithm. Flow velocities were exported and processed in Matlab. Plane fit was applied to the data to remove the plane resulted un-horizontal effect of the μ PIV work station.

Streamwise velocity

Figure 7 shows the streamwise u-velocity of the 0.025% xanthan gum in three microfluidic channels.

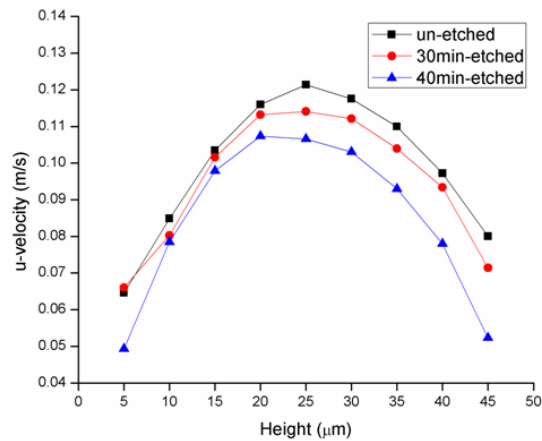
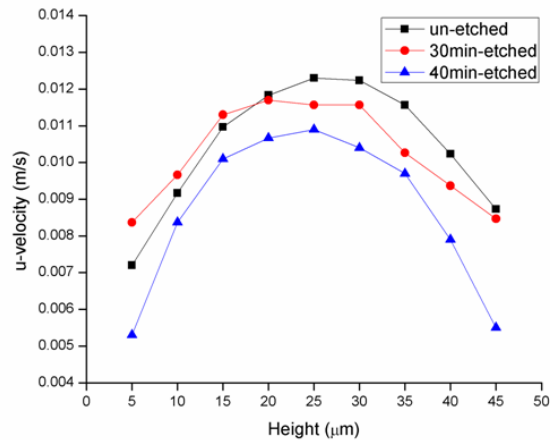


Figure 7. 0.025% xanthan gum solution tested on three devices (top: 0.01ml/min; bottom: 0.1ml/min)

Figure 8 shows the streamwise u-velocity of the 0.1% xanthan gum in three microfluidic channels.

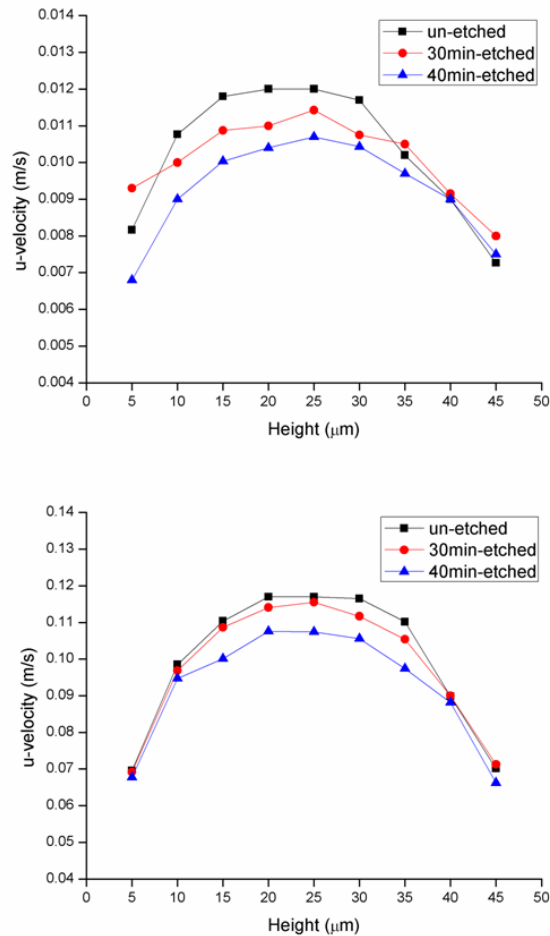


Figure 8. 0.1% xanthan gum solution tested on three devices (top: 0.01ml/min; bottom: 0.1ml/min)

As a comparison, the streamwise u-velocity of the DI water in three microfluidic channels is shown in figure 9.

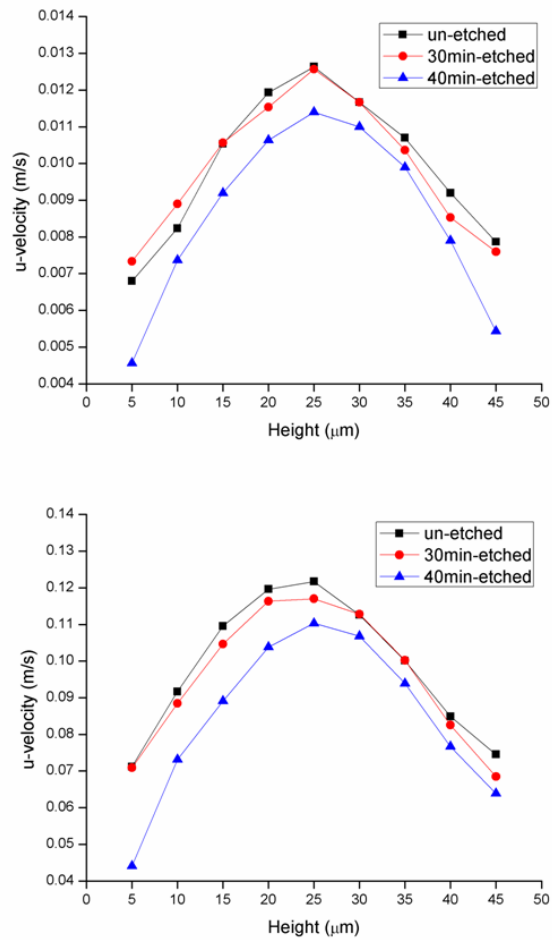


Figure 9. DI water tested on three devices (top: 0.01ml/min; bottom: 0.1ml/min)

In addition, the u-velocity was obtained and compared in a specific device between the 3 working fluids. Figure 10 shows the comparison in the device with the 30 min-etched glass wall.

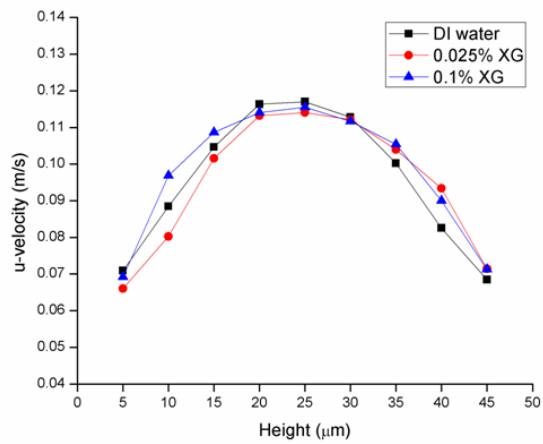
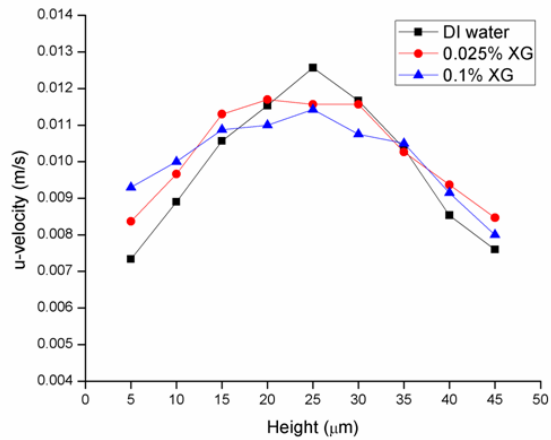


Figure 10. Three fluids tested in the 30 min-etched channel (top: 0.01ml/min; bottom: 0.1ml/min)

Figure 11 shows the comparison in the device with the 40 min-etched glass wall.

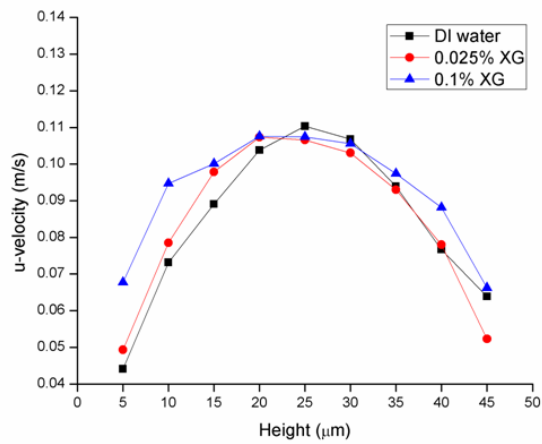
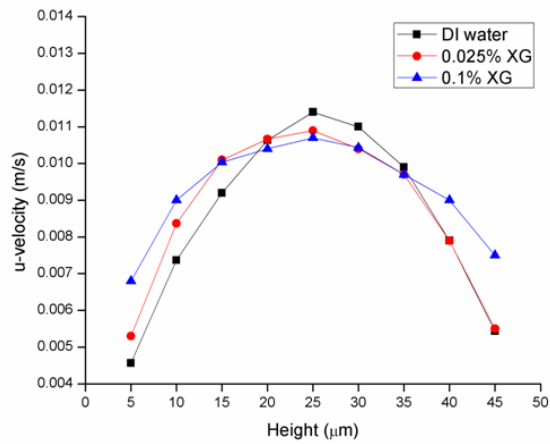


Figure 11. Three fluids tested in the 40-min-etched channel (top: 0.01ml/min; bottom: 0.1ml/min)

Figure 12 shows the comparison of u-velocity of the 3 working fluids in the device with the un-etched glass wall.

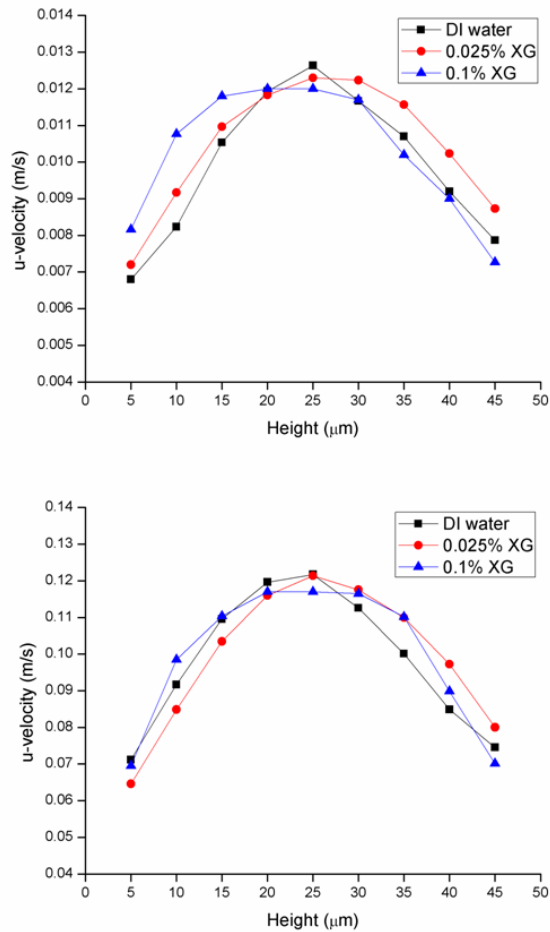


Figure 12. Three fluids tested in the un-etched channel (top: 0.01ml/min; bottom: 0.1ml/min)

Fluctuation in transverse velocity

The effect of roughness on fluctuation in transverse v-velocity was also studied through the autocorrelation calculation. The autocorrelation length of the v-velocity represents how the velocity perturbations caused by roughness cascades as height increases. Figure 13 shows the ACL values of the 3 working fluids as a function of height from the bottom wall of the un-etched microchannel. Slight increase was shown in both flow rates of 0.01 ml/min and 0.1 ml/min, while no significant difference among the 3 fluids was observed.

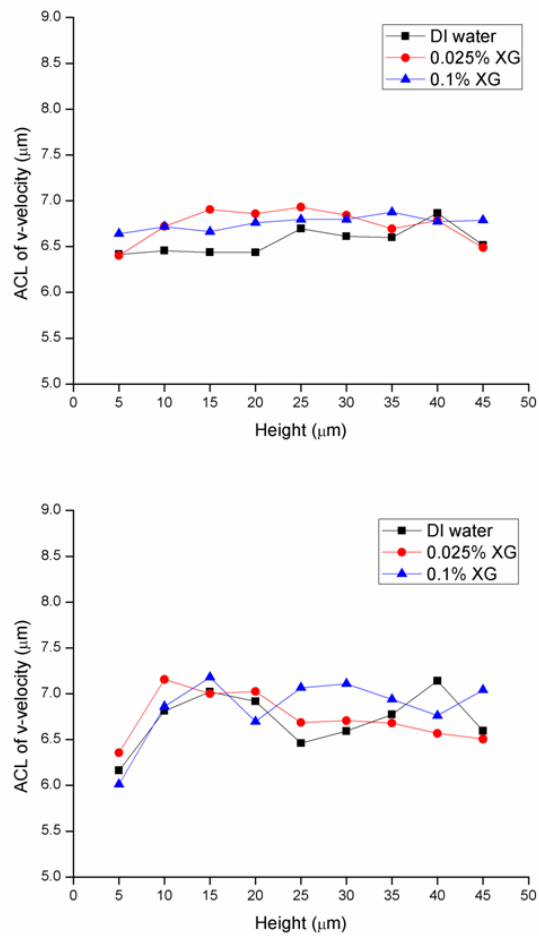


Figure 13. Three fluids tested on un-etched device (top: 0.01 ml/min; down: 0.1 ml/min)

ACL comparison of the 3 fluids in the 30 min-etched channel was shown in figure 14. 0.1% xanthan gum shows the highest ACL values at the middle plane of the channel, indicating that it has larger flow fluctuation caused by the roughness than the other two fluids.

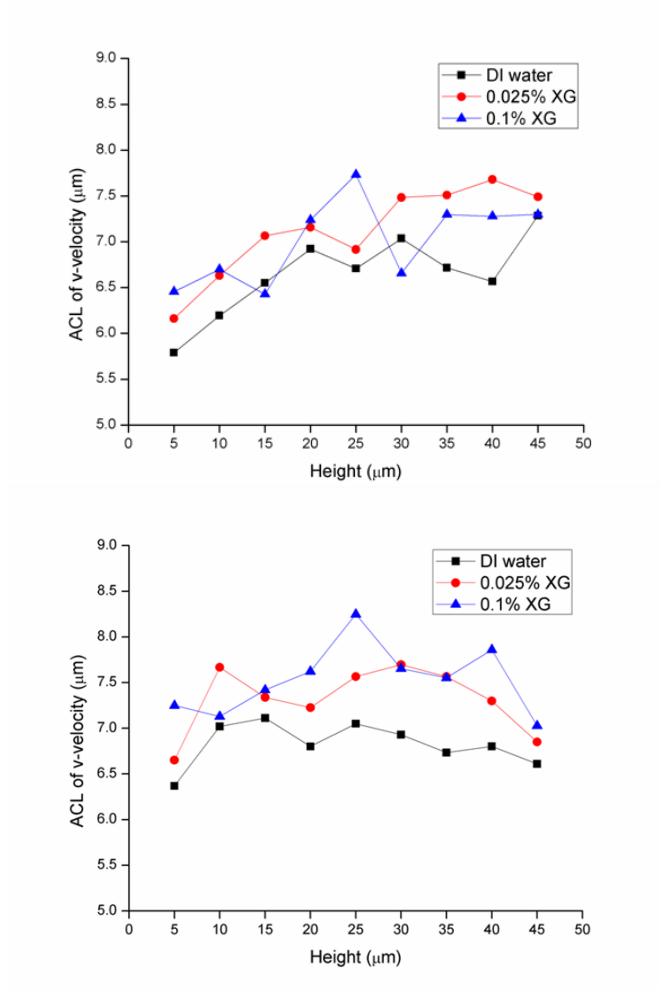


Figure 14. Three fluids tested on 30min-etched device (top: 0.01 ml/min; down: 0.1 ml/min)

The ACL comparison in the 40 min-etched channel is shown in figure 15, which is similar to the trend in the 30 min-etched channel as the highest ACL happens at the middle plane with 0.1% xanthan gum.

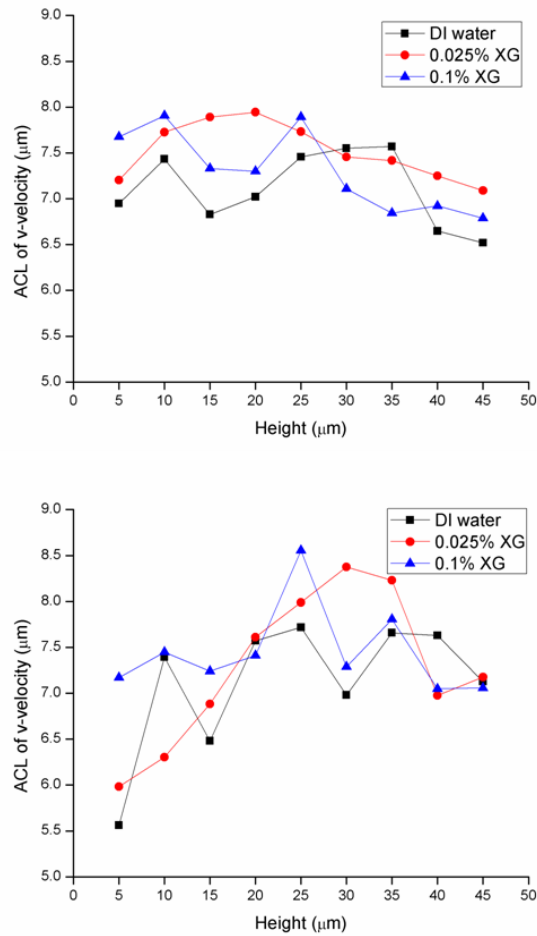


Figure 15. Three fluids tested on 40min-etched device (top: 0.01 ml/min; down: 0.1 ml/min)

Figure 16 gives a comparison of the ACL values between different devices using DI water as working fluid. The roughness influence can be clearly identified as the ACL value generally shows an increase trend as channel roughness increases. At the center layer, with 0.01ml/min flow rate, ACL shows an increase of 0.17% and 11.37% as relative roughness increases to 0.02% and 0.1% from 0.003%. Regarding the 0.1ml/min flow rate, similar flow perturbation enhancement was also observed as relative roughness increases: at the center layer,

as relative roughness increases to 0.02% and further to 0.1%, the working fluid shows a 9.14% and 19.46% increase in ACL compared to the situation with 0.003% relative roughness.

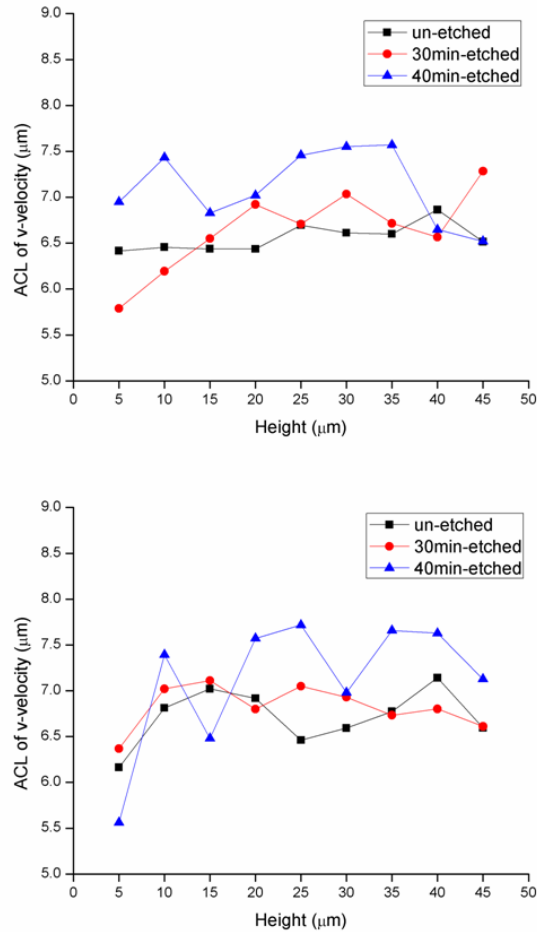


Figure 16. DI water tested on three device (top: 0.01 ml/min; down: 0.1 ml/min)

A comparison of the ACL values between difference devices using 0.025% xanthan gum is shown in figure 17. With 0.01ml/min flow rate, the average ACL of the transverse velocity shows an increase of 5.71% and 11.68% as relative roughness increases from 0.003% to 0.2% and further to 0.1%. At 25 μm height position, ACL increase is -0.21% (slight decrease) and 11.56% as relative roughness increases. Regarding the 0.1ml/min flow rate, similar flow

perturbation enhancement was also observed as relative roughness increases: at the center layer, as relative roughness increases to 0.02% and further to 0.1%, the working fluid shows a 13.16% and 19.49% increase in ACL compared to the situation with 0.003% relative roughness.

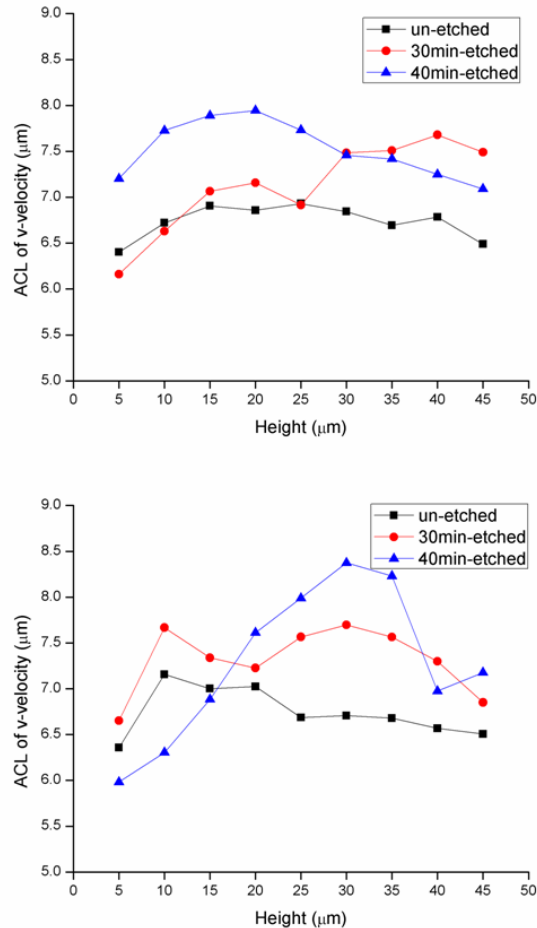


Figure 17. 0.025% xanthan gum tested on three device (top: 0.01 ml/min; down: 0.1 ml/min)

Figure 18 shows the comparison of the ACL values between difference devices using 0.1% xanthan gum. At the center layer, with 0.01ml/min flow rate, ACL increase is 13.8% and 16.15% as relative roughness increases.

Regarding the 0.1ml/min flow rate, at the center layer, as relative roughness increases to 0.02% and further to 0.1%, the working fluid shows a 16.76% and 21.08% increase in ACL compared to the situation with 0.003% relative roughness.

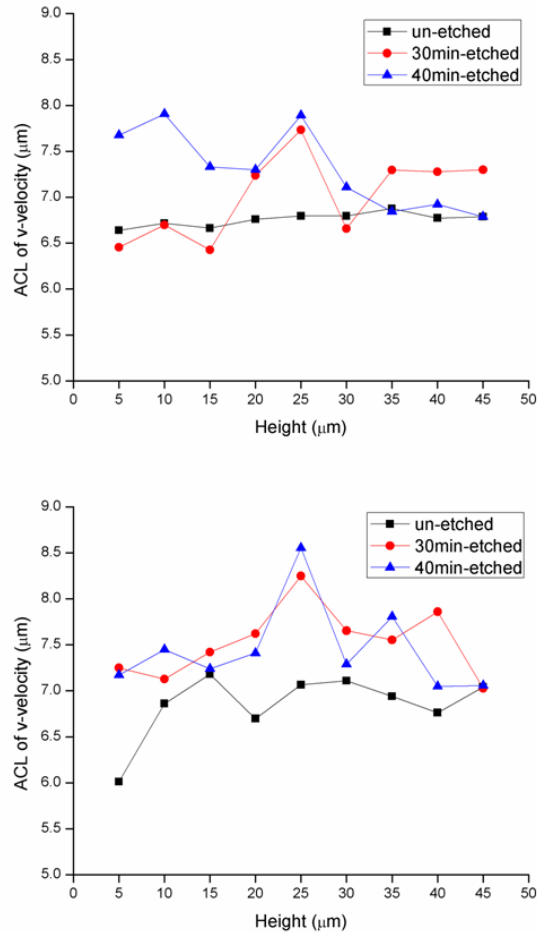


Figure 18. 0.1% xanthan gum tested on three device (top: 0.01 ml/min; down: 0.1 ml/min)

7.6. Conclusion

In this work, the effect of nanoscale random surface roughness on dilute xanthan gum as a blood-analog fluid was investigated. Different levels of nanoscale surface roughness were generated on glass

substrates by chemical wet etching. Three microfluidic devices with dimension of 25 mm (L) \times 400 μm (W) \times 50 μm (H) were further fabricated using the processed glass substrates and PDMS. Surface roughness on the microchannels walls was characterized by optical profilometry. 30 minutes and 40 minutes etching was shown to increase the relative roughness of the bottom channel wall from 0.003% to 0.02% and 0.1%. PDMS walls are considered to have similar relative roughness (0.002%) as the un-etched glass wall.

Dilute xanthan gum solution with different concentrations was used as working fluid. Deionized water was also tested as a comparison in this study. Through the velocity field measurement inside the microfluidic channel using microPIV, we have shown that the effect of the nanoscale random surface roughness can be captured and further characterized.

Two flow rates of 0.01 ml/min and 0.1 ml/min were tested in this study. Velocity field measurements were taken inside the microchannel starting from the bottom glass wall up to the top PDMS cover with an interval of 5 μm .

Among the three working fluids, the dilute xanthan gum solution, both 0.025% and 0.1%, showed the shear-thinning as achieving a fully developed shear flow within a shorter distance from the bottom and upper walls. The result showed that roughness on glass wall, compared to that of the upper PDMS cover, has decreased the u-velocity at the near-wall region up to the middle plane of the microchannels. This was observed among all the three working fluids under the two flow rates, and most significantly in the 40 minutes etched channel. At the center plane of the microchannels, u-velocity decrease was also observed generally in the two roughened channels (etched for 30 and 40 minutes). The effect of surface roughness on the u-velocity, as seen in the velocity distribution, is more obvious as the relative roughness increases.

The autocorrelation analysis revealed the perturbations caused by the surface roughness in the transverse flow. Autocorrelation length (ACL) of the v-velocity was compared between different microchannels with three working fluids. The ACL values showed a slight increase with the height from

the bottom glass wall and are comparable among the three fluids in the un-etched microchannel. As relative roughness increases in the microchannel, higher variation of the ACL values was observed, indicating larger size eddies were produced by the rough surfaces. This impact starts at the bottom of the microfluidic channels, where the glass wall was processed for desired roughness levels, and accumulates up to the center layer of the channels.

Quantitatively, as shown in Table 2, with 0.1ml/min flow rate, autocorrelation analysis of the flow velocity in transverse direction indicates that an order increase in relative roughness leads to a noticeable increase of the autocorrelation length in transverse velocity: at 25 μm height position, the three working fluids are showing 9.14%, 13.16% and 15.76% increase of ACL in transverse velocity as relative roughness increases from 0.003% to 0.02%. As relative roughness increases to 0.1%, the flow perturbation was further enhanced, which was characterized by an increase of 19.46%, 19.49% and 21.08% in ACL values, compared to the situation with 0.003% relative roughness.

Regarding the 0.01ml/min flow rate, similar flow perturbation enhancement was also observed as relative roughness increases: the average ACL of the transverse velocity shows an increase of 1.24%, 5.71% and 3.74% respectively with the three working fluids as relative roughness increases from 0.003% to 0.2%. At 25 μm height position, ACL increases among the three working fluids are 0.17%, -0.21% (decrease) and 13.8%, respectively. As roughness increases to 0.1%, among the three working fluids, average ACL of the transverse velocity increases 8.38%, 11.68% and 8.16% respectively, compared to that of 0.003% relative roughness. Also, at the center layer of the microfluidic channel (25 μm height position), the ACL increases are 11.37%, 11.56% and 16.15%.

Table 2. ACL increase as relative roughness increase from 0.003% to 0.02% and 0.1%

Fluids	0.01 ml/min		0.1 ml/min		0.01 ml/min		0.1 ml/min	
	Center layer (25 μm height)				Overall			
DI water	0.17%	11.37%	9.14%	19.46%	1.24%	8.38%	1.58%	6.03%
0.025% XG	-0.21%	11.56%	13.16%	19.49%	5.71%	11.68%	8.54%	7.98%
0.15 XG	13.80%	16.15%	16.76%	21.08%	3.74%	8.16%	9.88%	8.69%

This study experimentally proves that nanoscale surface roughness affects microfluidic flow in the laminar region and this effect can be realized through the rapid fabrication process and further captured by microPIV technique. By design nanoscale random roughness tailoring into microfluidic channel fabrication, this process provides a fast, low-cost and reliable solution for future studies on microfluidic applications such as droplet control, cell sorting, molecular manipulation and chemical detection, etc., through nanoscale surface tailoring technique. Based on the experimental result, the influence of shear thinning remains to be further explored using numerical simulation. The modeling of the working fluids inside microfluidic channel with nanoscale random surface roughness is the next target of our study.

7.7 Reference

1. Taylor, J.B., A.L. Carrano, and S.G. Kandlikar, *Characterization of the effect of surface roughness and texture on fluid flow - past, present, and future*. International Journal of Thermal Sciences, 2006. **45**(10): p. 962-968.
2. COLEBROOK, C.F., *Turbulent Flow in Pipes, with particular reference to the Transition Region between the Smooth and Rough Pipe Laws*. Journal of the ICE, 1939 **11**(4): p. 133 –156.
3. Moody, L.F., *Friction factors for pipe flow*. ASME Trans., 1944. **66**: p. 671-683.
4. Nikuradse, J., *Laws of Flow in Rough Pipes*. NASA Technical Memorandum, 1950(1292): p. 1-26.
5. Kandlikar, S.G., S. Joshi, and S.R. Tian, *Effect of surface roughness on heat transfer and fluid flow characteristics at low reynolds numbers in small diameter tubes*. Heat Transfer Engineering, 2003. **24**(3): p. 4-16.
6. Kandlikar, S.G., et al., *Characterization of surface roughness effects on pressure drop in single-phase flow in minichannels*. Physics of Fluids, 2005. **17**(10).
7. Ligler, F.S., et al., *Remote sensing using an airborne biosensor*. Environmental Science & Technology, 1998. **32**(16): p. 2461-2466.

8. Heim, S., et al., *Development of an automated microbial sensor system*. Biosensors & Bioelectronics, 1999. **14**(2): p. 187-193.
9. Schmalzing, D., et al., *DNA typing in thirty seconds with a microfabricated device*. Proceedings of the National Academy of Sciences of the United States of America, 1997. **94**(19): p. 10273-10278.
10. Vo-Dinh, T., *Development of a DNA biochip: principle and applications*. Sensors and Actuators B-Chemical, 1998. **51**(1-3): p. 52-59.
11. Walker, P.A., et al., *Isotachophoretic separations on a microchip. Normal Raman spectroscopy detection*. Analytical Chemistry, 1998. **70**(18): p. 3766-3769.
12. Mousoulis, C., et al., *A Skin-Contact-Actuated Micropump for Transdermal Drug Delivery*. IEEE Transactions on Biomedical Engineering, 2011. **58**(5): p. 1492-1498.
13. Ahn, C.H., et al., *Disposable Smart lab on a chip for point-of-care clinical diagnostics*. Proceedings of the IEEE, 2004. **92**(1): p. 154-173.
14. Natrajan, V.K. and K.T. Christensen, *The impact of surface roughness on flow through a rectangular microchannel from the laminar to turbulent regimes*. Microfluidics and Nanofluidics, 2010. **9**(1): p. 95-121.
15. Yang, D.Y. and Y. Liu, *Numerical simulation of electroosmotic flow in microchannels with sinusoidal roughness*. Colloids and Surfaces a-Physicochemical and Engineering Aspects, 2008. **328**(1-3): p. 28-33.
16. Palasantzas, G. and A. Widom, *Roughness effects on the sliding frictional force of submonolayer liquid films on solid substrates*. Physical Review B, 1998. **57**(8): p. 4764-4767.
17. Bahrami, M., M.M. Yovanovich, and J.R. Culham, *Pressure drop of fully developed, laminar flow in rough microtubes*. Journal of Fluids Engineering-Transactions of the Asme, 2006. **128**(3): p. 632-637.
18. Hao, P.F., et al., *Experimental investigation of water flow in smooth and rough silicon microchannels*. Journal of Micromechanics and Microengineering, 2006. **16**(7): p. 1397-1402.
19. Komvopoulos, K., *Surface engineering and microtribology for microelectromechanical systems*. Wear, 1996. **200**(1-2): p. 305-327.
20. Prentner, S., et al., *Effects of Channel Surface Finish on Blood Flow in Microfluidic Devices*. Dtip 2009: Symposium on Design, Test, Integration and Packaging of Mems/Moems, 2009: p. 51-54
- 429.
21. Kang, T., J. Han, and K.S. Lee, *Concentration gradient generator using a convective-diffusive balance*. Lab on a Chip, 2008. **8**(7): p. 1220-1222.
22. Keenan, T.M. and A. Folch, *Biomolecular gradients in cell culture systems*. Lab on a Chip, 2008. **8**(1): p. 34-57.

23. Lin, F., et al., *Generation of dynamic temporal and spatial concentration gradients using microfluidic devices*. Lab on a Chip, 2004. **4**(3): p. 164-167.
24. Thomas, T.R., *Rough surfaces*. 1999: Imperial College Press.
25. Ren, J., B. Ganapathysubramanian, and S. Sundararajan, *Experimental analysis of the surface roughness evolution of etched glass for micro/nanofluidic devices*. Journal of Micromechanics and Microengineering, 2011. **21**(2).
26. Ren, J., Sundararajan, S., *A hybrid surface tailoring process to generate desired random roughness on quartz*. in review, 2013.
27. Jaeger, R., et al., *Nanoscale surface roughness affects low Reynolds number flow: Experiments and modeling*. Applied Physics Letters, 2012. **101**(18).
28. Zhang, X.L. and S.J. Haswell, *Materials matter in microfluidic devices*. Mrs Bulletin, 2006. **31**(2): p. 95-99.
29. Bhushan, B., *Modern tribology handbook*. Vol. 1. 2001, Boca Raton: CRC.
30. Zhang, Y.L. and S. Sundararajan, *The effect of autocorrelation length on the real area of contact and friction behavior of rough surfaces*. Journal of Applied Physics, 2005. **97**(10): p. -.
31. Whitehouse, D.J. and J.F. Archard, *The Properties of Random Surfaces of Significance in their Contact*. Proceedings of the Royal Society of London. Series A, Mathematical and Physical Sciences, 1970. **316**(1524): p. 97-121.
32. Ren, J., Sundararajan, S., *A novel microfabrication method for nanoscale surface roughness impact on microfluidic flow*. In review, 2013.
33. Chien, S., et al., *Shear-Dependent Deformation of Erythrocytes in Rheology of Human Blood*. American Journal of Physiology, 1970. **219**(1): p. 136-&.
34. Schorsch, C., C. Garnier, and J.L. Doublier, *Viscoelastic properties of xanthan/galactomannan mixtures: comparison of guar gum with locust bean gum*. Carbohydrate Polymers, 1997. **34**(3): p. 165-175.
35. Kim, C. and B. Yoo, *Rheological properties of rice starch-xanthan gum mixtures*. Journal of Food Engineering, 2006. **75**(1): p. 120-128.
36. Whitcomb, P.J. and C.W. Macosko, *Rheology of Xanthan Gum*. Journal of Rheology, 1978. **22**(5): p. 493-505.
37. Whitcomb, P.J., B.J. Ek, and C.W. Macosko, *Rheology of Xanthan Gum Solutions*. Journal of Rheology, 1978. **22**(4): p. 425-425.
38. Milas, M., et al., *Flow and Viscoelastic Properties of Xanthan Gum Solutions*. Macromolecules, 1990. **23**(9): p. 2506-2511.

39. Casas, J.A., A.F. Mohedano, and F. Garcia-Ochoa, *Viscosity of guar gum and xanthan/guar gum mixture solutions*. Journal of the Science of Food and Agriculture, 2000. **80**(12): p. 1722-1727.
40. Sikora, M., et al., *Rheological and sensory properties of dessert sauces thickened by starch-xanthan gum combinations*. Journal of Food Engineering, 2007. **79**(4): p. 1144-1151.
41. Bandulasena, H.C.H., W.B. Zimmerman, and J.M. Rees, *An inverse method for rheometry of power-law fluids*. Measurement Science & Technology, 2011. **22**(12).
42. Gijssen, F.J.H., F.N. van de Vosse, and J.D. Janssen, *The influence of the non-Newtonian properties of blood on the flow in large arteries: steady flow in a carotid bifurcation model*. Journal of Biomechanics, 1999. **32**(6): p. 601-608.
43. Wickramasinghe, S.R., C.M. Kahr, and B.B. Han, *Mass transfer in blood Oxygenators using blood analogue fluids*. Biotechnology Progress, 2002. **18**(4): p. 867-873.
44. Liu, Y., M.G. Olsen, and R.O. Fox, *Turbulence in a microscale planar confined impinging-jets reactor*. Lab on a Chip, 2009. **9**(8): p. 1110-1118.
45. Shin, S. and D.Y. Keum, *Measurement of blood viscosity using mass-detecting sensor*. Biosensors & Bioelectronics, 2002. **17**(5): p. 383-388.
46. Bălan Cătălin Mihai, B.C., *μ PIV measurement and numerical computation of the velocity profiles in micro-channels*. UPB Scientific Bulletin, Series D: Mechanical Engineering, 2010. **72**(3).
47. Olsen, M.G. and R.J. Adrian, *Measurement volume defined by peak-finding algorithms in cross-correlation particle image velocimetry*. Measurement Science & Technology, 2001. **12**(2): p. N14-N16.

CHAPTER 8. CONCLUSIONS AND FUTURE WORK

In this work, the effect of micro/nano scale random surface roughness on microfluidic flow was explored. Random surface roughness generation, tailoring and characterization were understood through chemical wet etching on glass substrate. A hybrid process was further developed to generate and control random surface roughness on quartz. Microfluidic devices with desired surface roughness on the channel walls were fabricated for the roughness effect study. This investigation was made possible through high resolution DNS analysis and concurrent microPIV measurement.

8.1 Random roughness generation on glass substrate

In this work, the random roughness generated on glass substrate by buffered HF (6:1 volume ratio of 40% NH_4F in water to 49% HF in water) etching was studied. The surface roughness was characterized by amplitude parameter Ra and spatial parameters ACL. The surface distribution was also investigated. Results indicated that ACL can be increased in the range of 1-4 μm by varying the etch time. Ra was found to increase slowly within 30 minutes etch time from several nanometers to around 20 nanometers. Analysis of the experimental data using Kolmogorov-Smirnov goodness-of-fit hypothesis test (K-S test) shows that the glass surface roughness does not follow a Gaussian distribution, as is typically assumed in literature. Instead, the T location-scale distribution fits the roughness data with 1.11% error. These results provide promising insights into tailoring surface roughness for improving micro-fluidic devices.

8.2 Hybrid random roughness tailoring process on quartz substrate

In this work, a hybrid surface texturing process was developed to generate and control surface roughness on quartz substrate. The process combines reactive ion etching and colloidal masking and provides a practical roughness tailoring method by varying the masking particle size, coverage, and etches depth. A mathematical model was developed to predict the roughness parameter Ra and ACL. The experimental result from AFM measurement validated the prediction. The following conclusions can be drawn:

1. The spatial randomness of the final surface was tested and proved through calculation of the pair correlation function, indicating that the process, as a fast and low-cost technique, can be applied to surface texturing for stochastic roughness.

2. ACL can be effectively tailored by varying particle size and coverage: using 1.2 μm and 2.7 μm particles, ACL can be increased in the range of 2 μm to 6 μm by varying particle coverage from 5% to 30%; while using particle size of 5.5 μm , ACL can be further increased to 8 μm .

3. Amplitude roughness Ra can be controlled through particle coverage and etch depth: at etch depth of 277 nm, Ra can be increased from 65 nm to 105 nm by varying particle coverage from 5% to 50%; at a higher etch depth of 344 nm, Ra can be tailored in a wider range of 50 nm to 1 μm .

8.3 Effect of nanoscale surface roughness on microfluidic flow

8.3.1 Experiments and modeling study on Newtonian fluid

This work investigated the effect of stochastic nanoscale roughness on low Reynolds number Newtonian flow using concurrent modeling and experiments. Microfluidic devices were fabricated with tailored wall roughness. microPIV technique was used to characterize the flow field. The measured surface roughness and velocity field was integrated with Direct Numerical Simulation to resolve the effect of nanoscale roughness on the Newtonian flow (deionized water). Results indicated that nanoscale roughness causes flow perturbations that extend up to the mid-plane and is insensitive to flow-rates. Following conclusions can be drawn from this study:

1. Realistic random surface roughness, even at nanoscale, has a measureable effect on low Reynolds number microfluidic flow. This study is made possible through microPIV measurement combined with computational fluid dynamic DNS simulations.
2. Through the calculation of autocorrelation and energy spectra, the DNS simulation result was validated by the microPIV measurement.

8.3.2 Investigation of nanoscale surface roughness effect on non-Newtonian fluid

Based on the previous study, further investigation was applied to reveal how the nanoscale random roughness influences non-Newtonian blood analog fluid. Three microfluidic devices with different levels of channel wall roughness were fabricated. Microfluidic channel dimension is 25mm (L) $400\ \mu\text{m}$ (W) \times $50\ \mu\text{m}$ (H). Relative roughness was characterized as 0.003%, 0.02% and 0.1%, respectively. PDMS walls are considered to have similar relative roughness (0.002%) as the un-etched glass wall. Dilute Xanthan gum solution with weight concentrations of 0.025%

and 0.1% was tested as working fluid in the microPIV experiment, with flow rates of 0.1ml/min and 0.01ml/min, respectively.

Velocity comparison and autocorrelation analysis were applied to investigate the impact of the nanoscale roughness on flow behaviors:

1. Velocity comparison showed that among the three microfluidic devices, roughness on glass wall has decreased the u-velocity at the near-wall region up to the middle plane of the microchannels. This was observed among all the three working fluids under the two flow rates, and most significantly in the 40 minutes etched channel. At the center plane of the microchannels, u-velocity decrease was also observed generally in the two roughened channels (etched for 30 and 40 minutes). This impact on u-velocity is more obvious as the relative roughness increases.
2. The autocorrelation analysis revealed the perturbations caused by the surface roughness in the transverse flow. Autocorrelation length (ACL) of the v-velocity was compared between different microchannels with three working fluids. The ACL values showed a slight increase with the height from the bottom glass wall and are comparable among the three fluids in the un-etched microchannel. As relative roughness increases, higher variation of the ACL values was observed, indicating larger size eddies were produced by the rough surfaces. This impact starts at the bottom of the microfluidic channels, where the glass wall was processed for desired roughness levels, and accumulates up to the center layer of the channels.
3. Quantitatively, with 0.1ml/min flow rate, autocorrelation analysis of the flow velocity in transverse direction indicates that an order increase in relative roughness leads to a noticeable increase of the autocorrelation length in transverse velocity: at 25 μm height

position, the three working fluids are showing 9.14%, 13.16% and 15.76% increase of ACL in transverse velocity as relative roughness increases from 0.003% to 0.02%. As relative roughness increases to 0.1%, the flow perturbation was further enhanced, which was characterized by an increase of 19.46%, 19.49% and 21.08% in ACL values, compared to the situation with 0.003% relative roughness. This indicates a quantifiable flow perturbation caused by the different levels of nanoscale random surface roughness inside microfluidic devices.

4. Regarding the 0.01ml/min flow rate, similar flow perturbation enhancement was also observed as relative roughness increases: the average ACL of the transverse velocity shows an increase of 1.24%, 5.71% and 3.74% respectively with the three working fluids as relative roughness increases from 0.003% to 0.2%. At 25 μm height position, ACL increases among the three working fluids are 0.17%, -0.21% (decrease) and 13.8%, respectively. As roughness increases to 0.1%, among the three working fluids, average ACL of the transverse velocity increases 8.38%, 11.68% and 8.16% respectively, compared to that of 0.003% relative roughness. Also, at the center layer of the microfluidic channel (25 μm height position), the ACL increases are 11.37%, 11.56% and 16.15%.
5. This study experimentally proves that nanoscale surface roughness affects microfluidic flow in the laminar region and this effect can be realized through the rapid fabrication process and further captured by microPIV technique. By design nanoscale random roughness tailoring into microfluidic channel fabrication, this process provides a fast, low-cost and reliable solution for future studies on microfluidic applications such as

droplet control, cell sorting, molecular manipulation and chemical detection, etc., through nanoscale surface tailoring technique.

8.4 Future work

1. The roughness generation and tailoring process provides promising insights into tailoring surface roughness inside microfluidic devices and harness the roughness effect for improving performances. Beside the glass and quartz substrate used in this research, future work is suggested to extend surface roughness texturing and analysis of other pertinent materials for microfluidic device fabrication, such as silicon, PDMS, SU8, PMMA and other polymer materials.
2. In addition to the surface roughness tailoring techniques, wettability (hydrophilicity and hydrophobicity) modification is suggested by changing surface local chemistry, e.g., applying self-assembled monolayer thin film, wetting and non-wetting coatings, or other similar techniques to complement roughness tailoring.
3. Based on the current study on nanoscale roughness impact on non-Newtonian blood analog fluid, next focus will be combining direct numerical simulation (DNS) with the experimental result to enable experimental-computational analysis of the microfluidic flow behavior inside rough channels.

ACKNOWLEDGEMENTS

I would like to thank my husband, Yufeng Wu, for his support and understanding during my study. Thank my parents Jiakai Ren, Hongmei Yu, and my siblings Hui Ren, Qun Ren, Ci Ren, for all your support and love. Without which, I would never have the opportunity to achieve what I have today.

I would like to express my deepest gratitude to my advisor, Dr. Sriram Sundararajan, for being my guide and mentor throughout my PhD study. Thanks for guiding me to find the right track but not necessarily by giving the answers, but more importantly by posing me to the challenging questions and encouraging me to find the right answers myself. Thanks for always being supportive, patient and helpful in my study.

Also, I would like to take this opportunity to thank my committee member, Dr. Baskar Ganapathysubramanian, for always being open to discussion, helpful and supportive on my research projects during these years.

Thanks to Dr. Michael Olsen, for providing support including the microPIV facility when I work in his lab. Thanks for all the discussion and help during and after my experiments.

Special thanks to Robert Mayer, Max Noack, Dr. Gary Tuttle and Dr. Vikram Dalal in Microelectronics Research Center, for helping me with the facility use and troubleshooting in my project.

APPENDIX A. DETAILED PROCESS METHODOLOGY

I. Process flow of glass surface treatment using chemical wet etching

1. The surface roughness examined in this study was generated on glass slides (25 mm × 75 mm, Erie Scientific Company, Portsmouth, NH).
2. The glass samples were etched by buffered HF (6:1 volume ratio of 40% NH₄F in water to 49% HF in water) to generate different surface roughness. The etch rate was calibrated as 72 nm/min.
3. Samples were immersed in buffered HF and etched for different time period: 5min, 10min, 20min, 25min, 30min, and 35min.
4. Two samples were prepared for each etching condition. After HF etching, the samples were rinsed in DI water for 5 minutes and dried by nitrogen. Two smooth (un-etched) glass slides were also prepared for comparison.
5. All the etched samples were cleaned in acetone and dried by nitrogen to remove organic waste and dust on the surface before taking AFM images. All the AFM scans were acquired in contact mode using a standard Si₃N₄ tip, at a scan resolution of 256×256 points. The scan size was chosen as 75 μm × 75 μm.

II. Process flow of tailoring surface roughness on quartz

1. Before the deposition, quartz slides were cleaned by base piranha etch (3:1 mixture of NH_4OH and H_2O_2), which results negatively charge on the surfaces. A PDDA monolayer was coated on the surface by dipping the quartz substrates into 5% PDDA solution, which formed a polycationic layer on the surface.
2. Polystyrene colloidal solution was sonicated for 15 minutes and the particles were deposited on the surface through dip coating and drop casting methods. During dip coating, the slightly negatively charged particles were absorbed onto the surface randomly. Dip coating method provides good random particle coverage from around 5% to 30%. Drop casting was used to achieve higher coverage up to 70%. While drop casting, the quartz substrates were placed on hotplate with 95°C . Polystyrene solution was applied to the surface with syringe. After coating, the substrates were rinsed in DI water for 5 seconds to remove the loosely attached particles and dried naturally in room temperature. In this study, the particle coverage varies from around 5% to 70%.
3. RIE treatment was executed in a capacitively coupled plasma therm reactive etch system. The coated quartz substrates were etched for 6.5 minutes using SF_6 gas. The flow rate is 28 SCCM. Base pressure is 0.05 mTorr, and process pressure is 31 mTorr. Bias voltage is 500V, and RF power is 420 W. Etch rate of quartz substrate was calibrated as about 49 nm/min. Etch rate of polystyrene with SF_6 gas was reported as about 25 nm/min with pressure of 100 mTorr and power of 50 W.
4. After etching, the remaining particles on the surface were removed by acetone wash for 30 minutes.

III. Process flow for SU-8 mold fabrication

1. Standard clean of 3 inch glass wafer.
2. Bake at 120 °C for 1 hour in oven to dehydrate the wafer.
3. Dispense 3ml SU-8 2075 (microchem) on the wafer.
4. Spin at 1250 rpm for 30 seconds.
5. Soft bake on hot plate, temperature ramped to 65 °C, then keep 10 minutes; then ramp to 95 °C, keep 130 minutes, then cool to room temperature.
6. Expose, UV light, 65 seconds.
7. Post exposure bake (PEB), 55 °C for 2 hours, then cool to room temperature.
8. Develop (SU-8 developer, microchem) for 12 minutes.
9. Rinse with IPA.
10. Hard bake, 150°C for 15 minutes.

IV. Operating procedure of preparing PDMS

In preparation for this stage, obtain unpowdered disposable gloves, a disposable plastic stir stick and a disposable plastic cup.

1. Mix the PDMS: use the digital scale to measure 1:10 ratio of curing agent and PDMS monomers into the disposable plastic cup.
2. Stir the PDMS: use the disposable plastic stir stick to stir the mixture for approximately 3 minutes. The mixture will have many air bubbles inside.
3. Degas the PDMS: to degas the PDMS, place the mixture into a dessicator, which connects to a vacuum pump. The vacuum causes the bubbles in the PDMS mixture to expand and rise to the surface where they pop.
 - a. Make an aluminum foil boat and put into the c to catch any PDMS spills during the degassing process.
 - b. Put the PDMS mixture into the dessicator.
 - c. Close the lid of the dessicator and adjust the vacuum valve on the dessicator to connect the vacuum line.
 - d. Turn on the vacuum pump, observe the bubble raise up and break. Turn off the pump as the bubbles arrive the top of the cup. Wait until the bubbles recede and repeat several times.
 - e. Leave the PDMS in the dessicator for 2 hours.
4. The PDMS is ready to be taken out of the vacuum when there are nearly no bubbles in the liquid.
5. Disconnect the dessicator from the vacuum pump, the foil boat can be kept in for later use.

V. PDMS replica fabrication

1. Place a layer of aluminum foil into a clean glass beaker, then place the SU-8 mold into the beaker. The aluminum foil helps to remove the PDMS easily after it cures.
2. Cast proper amount of the PDMS mixture (approximately 5mm in depth) into the glass beaker to completely immerse the SU-8 mold. Try to cast very slowly to avoid bringing air bubble into the PDMS.
3. Insert stainless steel pins (with the same size of the inlet and outlet) into the PDMS mixture on the positions of the microfluidic channel inlets and outlets. This is to form the inlet and outlet holes after while the PDMS cures.
4. Set the oven temperature to 60 °C and place the glass beaker into carefully. The PDMS will cure in 8 hours. For optimum curing, leave the glass beaker in the oven over night.
5. Detach the aluminum foil from the glass beaker. Use a knife if necessary to remove the foil.
6. Slowly peel the PDMS off from the SU-8 mold. Pull out the stainless steel pins carefully and try not to create any cracks on the PDMS.
7. Use transparent tape to protect the detached PDMS surface from contamination.
8. Use a blade to trim the extra PDMS and leave the part contains the microfluidic channels. The PDMS replica is ready for the bonding process.
9. Store the SU-8 mold into a clean wafer holder for repeated use.

VI. Bonding of the PDMS replica and glass substrate

1. Oxygen plasma was provided by a plasma cleaner system (PDC-32G, Harrick Plasma, Ithaca, NY).
2. Place both the PDMS replica and the glass substrate into the chamber and treat with medium-level oxygen plasma for 55 seconds.
3. Bring the surface-activated PDMS and glass into contact. Apply appropriate pressure and the two parts seals quickly and form a very hard-to-break bond.
4. Insert tubing into the inlet and outlet of microfluidic channel. Apply appropriate amount of silicone sealant to seal the edge of the inlet and outlet. The microfluidic device is ready for sealing test and further study.

APPENDIX B. MATLAB CODES

Matlab code 1

%This program estimates the pdf of AFM roughness data using maximum likelihood (currently only using normal and logistic fit) and constructs the two point correlation of the AFM image. Subsequently an exponential curve fit is performed to extract the correlation length.

```
function [A_vec,ACL] = dataextract1(A)

Clear all;
A = A(:,1:end-1);

A_max = max(max(A))
A_min = min(min(A))

%use the minimum height as the datum..
A = A - A_min;
A_max = max(max(A));
A_min = min(min(A));

%Set number of bins.
%CHECK convergence with varying bin size?
n_bins=50;
delta_A = (A_max-A_min)/n_bins;
%convert matrix into a long vector
A_vec = A(:);

%extract the two poitn correlation
for r=0:size(A,2)
    L_2(r+1) = correlations2pt2d(A,r,0,2);
end
L_2=(L_2-min(L_2))./(max(L_2)-min(L_2));
%-----
%fit an exponential fit to this data
%another good idea is to try the statistic toolbox in Matlab: cftool
%-----
% Set scan size
Length_true = 75000e-9; %in nanometers
Length_pixel = size(A,2); %scan size
X = (0:Length_pixel).*Length_true./Length_pixel;

e=2.71828183;
S=size(L_2);
for i=1:S(2)
    if (L_2(i))<1/e
        break
    end
end
ACL=X(i-1)+(X(i)-X(i-1))*abs(L_2(i-1)-1/e)/abs(L_2(i-1)-L_2(i));
```

Matlab code 2

%Function returns the 2 point correlation at radius 'r', BW is the image,N1 is the number of initial points, N2 is the number of sampling points.

```
function out = correlations2pt2d(BW,r,thet,N1)

ymax = size(BW,1);
xmax = size(BW,2);

val= 0;
for n=1:N1
    for i=1:xmax
        for j=1:ymax
            pt=[i j];
            thet=rand*2*pi;
            pt2 = round([pt(1)+r*cos(thet);pt(2)+r*sin(thet)]);
            iter=1;
            if (pt2(1)>xmax)
                pt2(1)=pt2(1)-xmax;
            end
            if (pt2(2)>ymax)
                pt2(2)=pt2(2)-ymax;
            end
            if (pt2(1)<1)
                pt2(1)=pt2(1)+xmax;
            end
            if (pt2(2)<1)
                pt2(2)=pt2(2)+ymax;
            end
            ZI = BW(pt2(2),pt2(1));
            ZII = BW(pt(2),pt(1));
            val = val+ ZI*ZII;
        end
    end
end
out = val./(xmax*ymax*N1);

function y = genrand(len1,len2)
y(1) = floor(rand*(len1-1))+1;
y(2) = floor(rand*(len2-1))+1;
```

Matlab code 3

%This program is a batch file that automatically detects the files in a folder and runs through them to find out the nu parameter

```

clear all
% Enter the directory name with data here
dir_name = sprintf('45degreeetch');

% find out all the files in this directory
files = dir(dir_name);

% remove the '.' file and the '..' file
files(1) = []; files(1) = [];

%total number of files
n_files = size(files,1);

%loop through these files
for i=1:n_files
    % current file name
    filename = sprintf('%s/%s',dir_name,files(i).name)
    % open this file
    fidin=fopen(filename,'r');
    %Read the raw data into A
    A = textread(filename, '', 'headerlines',597);
    fclose all;
    clear fidin

    A = A(:,1:end-1);

    A_max = max(max(A))
    A_min = min(min(A))

    %use the minimum height as the datum..
    A = A - A_min;
    A_max = max(max(A));
    A_min = min(min(A));
    A_vec = A(:);

    %-----
    %DISTRIBUTION FITTING
    %-----
    %try normal
    [mu,sigma] = normfit(A_vec);

    % Using maximum-likelihood estimators
    % Try student t distribution (custum distribution)
    %phat = mle(A_vec,'pdf',@pdf_test,'cdf',@cdf_test,'start',[mu sigma
3.0],'lowerbound',[mu/2 0.0 2.0]); %[mu, sigma, nu]

```

```

    phat = mle(A_vec, 'pdf', @pdf_test, 'cdf', @cdf_test, 'start', [mu sigma
3.0], 'lowerbound', [mu/2 0.0 1.0], 'optimfun', 'fmincon');
    mu(i) = phat(1);
    sigma(i) = phat(2);
    nu(i) = phat(3);
end

```

Matlab code 4

%This program is a batch file that automatically detects the files in a folder and runs through them to find out the nu parameter, then the code computes the KS test for a random subset of the original data

```

clear all
% Enter the directory name with data here

dir_name = sprintf('test');

% find out all the files in this directory
files = dir(dir_name);

% remove the '.' file and the '..' file
files(1) = []; files(1) = [];

%total number of files
n_files = size(files,1);

%Store in a file
fp = fopen('flat.txt','w')

%loop through these files
for i=1:n_files
    % current file name
    filename = sprintf('%s/%s',dir_name,files(i).name)
    % open this file
    fidin=fopen(filename,'r');
    %Read the raw data into A
    A = textread(filename, '', 'headerlines', 597);
    clear fidin

    %-----
    % COMPUTING THE ACL
    %-----
    % Perform the data - processing to compute teh ACL
    A = A(:,1:end-1);
    A_min = min(min(A));
    %use the minimum height as the datum..

```

```

A = A - A_min;
A_vec = A(:);

%-----
%DISTRIBUTION FITTING
%-----
% compute empirical function
t_ = ~isnan(A_vec);
Data_ = A_vec(t_);
[Y_,X_] = ecdf(Data_);

% Fit this distribution to get parameter values
t_ = ~isnan(A_vec);
Data_ = A_vec(t_);
% To use parameter estimates from the original fit:
p_ = [ 42.99023976329, 11.39231007901, 5.822848304197];
p_ = mle(Data_, 'dist','tlocationscale', 'alpha',0.05) % Fit t location-
scale distribution
y_ = cdf('tlocationscale',X_,p_(1), p_(2), p_(3)); % compute cdf

%FITTED parameter values
mu(i) = p_(1);
sigma(i) = p_(2);
nu(i) = p_(3);

%(Difference between ecdf and computed cdf)
error =abs(Y_-y_);
error_45degree(i) = mean(error);

%Store X_, Y_, y_, error, and hypothesis test number_succesful_t_test
%number_succesful_n_test

% repeat this for 5 different sample size
for k=655:-50:655
    number_succesful_t_test = 0;
    number_succesful_n_test = 0;
    %repeat this for n=500 trials
    for j=1:1000
        %pick a random subset of the original data
        r_cell= unique(ceil(size(A_vec,1)*rand(ceil(size(A_vec,1)/k),1)));
        %pick a random subset
        A_vec_subset = A_vec(r_cell);
        %test the data with log_t distribution
        h_t = kstest(A_vec_subset,[X_ y_],0.05);
        if(h_t==0)
            number_succesful_t_test = number_succesful_t_test +1;
        end
        %test the data with normal distribution
        h_n = kstest(A_vec_subset);
        if(h_n==0)
            number_succesful_n_test = number_succesful_n_test +1;
        end
    end
    success_t(k/655,i) = number_succesful_t_test;
    success_n(k/655,i) = number_succesful_n_test;
end

```

```

end
%store athe data in the file
fprintf(fp, '%s \n', filename);
fprintf(fp, '%10.8f \t %10.8f \t %10.8f \n', mu(i), sigma(i), nu(i));
fprintf(fp, '%d \t %d \t %d \t %d \n', success_t(1,i));
fprintf(fp, '%d \t %d \t %d \t %d \n', success_n(1,i));
end

fclose(fp);

```

Matlab code 5

%This program processes microPIV data including outliers elimination and plane fit, and constructs the two point correlation.

```

clear all
addpath 'E:\Program Files\MATLAB\R2010a\toolbox\matlab\readimx';

%% point1
%smooth
path = 'E:\Study\RESEARCH';

Davis = readimx(path);
[X,Y,Vxt,Vyt,choice] =scaledimx(Davis);

%% Analysis

axis_1_min = 10;
axis_1_max = 50;
axis_2_min = 20;
axis_2_max = 60;

X1 = X(axis_1_min:axis_1_max, axis_2_min:axis_2_max);
Y1 = Y(axis_1_min:axis_1_max, axis_2_min:axis_2_max);
X_vec = X1(:);
Y_vec = Y1(:);
Vx = Vxt(axis_1_min:axis_1_max, axis_2_min:axis_2_max);
Vy = Vyt(axis_1_min:axis_1_max, axis_2_min:axis_2_max);

```

```

%vectorize the field
Vx_vec = Vx(:);
Vy_vec = Vy(:);

% remover spurious data-points
% find where the particles are stuck, when 0.01ml/min, remove
% log(abs(Vy_vec))<=-6); when 0.1ml/min, remove log(abs(Vy_vec))<=-5)
[a b] = (find(log10(abs(Vx_vec))<=-6));

%remove these data points
Vy_new_vec = Vy_vec;
Vy_new_vec((find(log10(abs(Vx_vec))<=-6))) = [];
Vx_new_vec = Vx_vec;
Vx_new_vec((find(log10(abs(Vx_vec))<=-6))) = [];

%% get the mean without counting 0
Vx_mean = mean(Vx_new_vec);
Vy_mean = mean(Vy_new_vec);

%% replace all spurious values with mean
Vx_new = Vx;
Vy_new = Vy;
Vx_new([a b]) = Vx_mean;
Vy_new([a b]) = Vy_mean;

clear Vy_vec;
clear Vx_vec;
clear Vx_new_vec;
clear Vy_new_vec;

%% plane fit
% Convert all inputs to column vectors.
X_vec = X1(:);
Y_vec = Y1(:);
Vx_vec = Vx_new(:);
Vy_vec = Vy_new(:);

% Fit:
ft = fitype( 'poly11' );
opts = fitoptions( ft );
opts.Lower = [-Inf -Inf -Inf];
opts.Upper = [Inf Inf Inf];
opts.Weights = zeros(1,0);
[fitresult_Vx, gof] = fit( [X_vec, Y_vec], Vx_vec, ft, opts );
[fitresult_Vy, gof] = fit( [X_vec, Y_vec], Vy_vec, ft, opts );

%% velocity after remove the plane
Vx_vec = Vx_vec - fitresult_Vx(X_vec,Y_vec) + Vx_mean;
Vy_vec = Vy_vec - fitresult_Vy(X_vec,Y_vec) + Vy_mean;

```

```

%% convert Vx_vec and Vy_vec to matrix
% axis_1_min:axis_1_max, axis_2_min:axis_2_max
for vec_tran = 1:axis_2_max-axis_2_min+1
    Vx_final(:,vec_tran) = Vx_vec(1 + (vec_tran-1)*(axis_1_max-
axis_1_min+1):vec_tran*(axis_1_max-axis_1_min+1));
    Vy_final(:,vec_tran) = Vy_vec(1 + (vec_tran-1)*(axis_1_max-
axis_1_min+1):vec_tran*(axis_1_max-axis_1_min+1));
end

%% calculate ACL of velocity
for i=1:50
[Vy_vec,ACL_vy] = dataextract1(Vy_final);
[Vx_vec,ACL_vx] = dataextract1(Vx_final);
allACL_vy(i) = ACL_vy;
allACL_vx(i) = ACL_vx;
ACL_vy = mean (allACL_vy);
ACL_vx = mean (allACL_vx);
end
    ACL_vy
    ACL_vx

```

Matlab code 6

%This program removes outliers for matrix data

```

function [X,nout,sigma,mu] = RemoveOutliersM(X_in)
%calculate mean and standard deviation
X_in_vec = X_in(:);
mu = mean(X_in_vec);
sigma = std(X_in_vec);

[n,p] = size(X_in);
% Create a matrix of mean values by
% replicating the mu vector for n rows
MeanMat = repmat(mu,n,p);
% Create a matrix of standard deviation values by
% replicating the sigma vector for n rows
SigmaMat = repmat(sigma,n,p);

```

```

% Create a matrix of zeros and ones, where ones indicate
% the location of outliers
outliers = abs(X_in - MeanMat) > 3*SigmaMat;
% Calculate the number of outliers in each column
nout = sum(sum(outliers));
%remove these values from the data
[outlier_pos_x,outlier_pos_y] = find(outliers>0);
for i=1:size(outlier_pos_x)
    %if outlier_pos_x(i)>1 && outlier_pos_x(i)<n && outlier_pos_y(i)>1 &&
outlier_pos_y(i)<p
X_in(outlier_pos_x(i),outlier_pos_y(i))=(X_in(outlier_pos_x(i)+1,outlier_pos_
y(i))+X_in(outlier_pos_x(i),outlier_pos_y(i)+1)+X_in(outlier_pos_x(i)-
1,outlier_pos_y(i))+X_in(outlier_pos_x(i),outlier_pos_y(i)-1))/4;
    %else
    X_in(outlier_pos_x(i),outlier_pos_y(i))=mu;
%end
end
X=X_in;

```